A STUDY OF THE CENTRALLY PRODUCED $\eta\pi^+\pi^-$ AND $\pi^+\pi^-\pi^0$ SYSTEMS AT 450 GeV/c

Christopher J. Dodenhoff

Thesis submitted for the degree of
Doctor of Philosophy

School of Physics and Space Research
Faculty of Science
University of Birmingham

November 1994

Synopsis

The WA91 experiment is designed to study centrally produced exclusive final states formed in the reaction pp $\rightarrow$ $p_f(X^0)p_s$ at 450 GeV/c incident momentum, where the subscripts f and s indicate the fastest and slowest particles respectively in the laboratory frame, and X^0 represents the central system which is believed to be formed by a double exchange process. The ultimate aim of WA91 is to identify non-$q\overline{q}$ states such as glueballs and hybrids. This thesis presents results of an analysis of the $\eta\pi^+\pi^-$ and $\pi^+\pi^-\pi^0$ channels produced from the decay of X^0.

In the $\eta\pi^+\pi^-$ channel clear $\eta'(958)$ and $f_1(1285)$ signals are observed. The $f_1(1285)$ is observed to decay to $\delta/a_0(980)\pi$ and a spin parity analysis shows that it is consistent with being a 1^{++} state. In addition a resonance is observed in the 1.9 GeV region which may be the $a_2(1320)\pi$ decay mode of the X(1900) observed in the $\pi^+\pi^-\pi^+\pi^-$ channel of the same experiment, although a spin parity analysis of this state is inconclusive due to lack of statistics. No evidence is seen for any pseudoscalar states in the 1.4 to 1.6 GeV region, and no evidence is seen for the $E/f_1(1420)$.

The $\pi^+\pi^-\pi^0$ channel shows clear $\eta(547)$ and $\omega(783)$ signals, along with the $a_1(1260)$. In a spin parity analysis the $a_1(1260)$ is clearly seen in the 1^{++} $\rho\pi$ wave with mass 1239 $\pm$ 27 MeV and width 456 $\pm$ 62 MeV, parameters consistent with the Particle Data Group values. Evidence is also seen for some $a_2(1320)$ production, which is seen in the mass spectrum and in the 2^{++}D $\rho\pi$ wave. The $a_1(1260)$ and $a_2(1320)$ are both observed to be isospin 1 states.

To my parents

I would like to thank Professors George Morrison and John Dowell for giving me the opportunity to undertake a PhD in the School of Physics and Space Research all those years ago. I would also like to thank the long suffering taxpayer in the guises of the SERC and D(SS) for supplying me with enough funding to keep the bailiffs at arms (and sometimes fingers) length. Many many thanks must also go to John Kinson and my supervisor Orlando Villalobos Baillie for their help, advice and encouragement (and even threats) without which I would not have survived to complete my thesis. Thanks are also extended towards Laurie Lowe for his computing expertise and for never deleting my Megabytes of spool files no matter how many warnings I ignored.

Special gratitude is expressed towards Andrew Kirk, guru of the WA91 experiment, for never being too busy to answer the most facile of questions and for giving me many well placed kicks in the butt without which I'd never have completed my thesis. I would like to thank Andy, John and Orlando for reading the drafts of my thesis and for tolerating me far longer than any reasonable person would.

I would also like to thank the rest of the Birmingham Omega group for the special atmosphere (usually spiced up by alcohol) generated, especially at CERN. Cheers to Frank Votruba for his ability to argue about anything, to Noel Carney for gin and many interesting evenings/mornings in France and Geneva, and to Roman Lietava, especially for that well timed parting gift of a bottle of vodka.

Thanks are also due to the rest of the WA91 collaboration, in particular Bernard French for help on analysis and the ORC reconstruction program, George Vassiliadis for humour above and beyond the call of a Greek, Raymond and Monique Sene, Maria Girone, and to the Russian/Georgian lads - Irakly, Alexei, Goran and Sergei for that ab fab trip to Dubna and for being all round diamond geezers.

And now to those who over the years I have come to consider as people I have met. First and foremost I would like to thank the members of the Published Club - Mark 'Son of Lenin' Whalley for showing me how political debate is always best augmented by extreme violence, to Richard 'Ginger' Barnes for having the liver of 10 men and proving it on many occasions at home and abroad (and for introducing me to 'that' pub) and to Mike 'Pyromania' Haben for his ability to turn household objects into weapons of war. Many thanks too to Tan 'The Gunners' Ahmed for taking longer to write up than me (and for the tips on jobhunting), and to Ish 'Quizmaster' Badr for being as keen to get a job as I was. Cheers and hurrahs to Steve 'Down Under' Clewer for those angry months at CERN and for being able to swim (hope everything goes well in your new life), Andy 'The Boy' Bayes (when he was here), Stuart 'I'll give up tomorrow' Robertson and Jim 'Overdraft' Clayton for the beer breaks (including the one I've just returned from to type this) and Paul 'Mellow' Davies for altering the way I think. Many hugs and kisses (but not in a girly bumlick sort of way) to Lee 'Curry' West for his interest in graphics and the ability to take an insult (probably due to years of practice), Dave 'Beavis huh huh heh heh heh' Rigby for not being a wussy assmunch and for expanding my vocab with words such as c-banana and f-pig, Keith 'Brucie' Norman (a comic talent wasted on physics), Tim 'Workaholic' Nicholls and Vicki 'Nellie' Hudgson for being the first woman in particle physics for 10 decades. Thanks also to the older generation of Steve Hillier and Dave Rees for being able to finish their PhD's in spite of the chaos erupting constantly in the Orlit, and of course to the inimitable Dave Evans who in spite of being a fascist capitalist pig-dog who kicked me out of my office 2 weeks ago was actually quite bearable. Gratitude is expressed for no particular reason to the new first years - James, Mark, Andrew, Stephen and Kirstee (in spite of the insults). Merci beaucoup to the quiz team - Alan, Roger (for never refusing a beer session), Roger and Chris for winning me cans of beer. Thanks in abundance to Rob Akers, Warren, Ollie, Rich Carney, Mike Natuch, Neil 'Shagger' Talbot, Paul Newman and Mark 'Mickey' Pearce for being. Much cheering for Rachel West for being able to do a proper days work and still go out on the ciders, and to Becky le Marachel for matchmaking in a fashion likely to cause a breach of the peace [37] and for being all in all a truly fabulous human being. Ta very much chuck to me chums back up north - Steve, Harvey and Jonathan 'Cardinal Chunder'.

Special thanks must go to Bob and Les for being the type of landlord and landlady any poor student would wish for, and to their dog Katie for eating all my biscuits. Sporting thanks to Frank Macdonald and the other members of the various physics footie teams for keeping me busy, and to the Village Football Club. And a hearty one cheer to anybody else I met/slagged off/lusted after in my not inconsiderable time here.

Finally my deepest thanks to my Dad and my brothers, Ron and Paul, for their love and support which did everything to get me to this stage, and especially to my Mum who died shortly before I completed my thesis, to whom I will be eternally grateful. If you are reading this thanks for everything you did and I'll never forget you.

Chris Dodenhoff

Birmingham

November 1994.

To probe the visible world we use the assumption that things are simple until they prove to be otherwise.

- E. H. Gombrich, *Art and Illusion*, 1960.

O passi graviora, dabit deus his quoque finem.

- Virgil, *Aeneid I.199.*

Forsan et haec olim meminisse iuvabit.

- Virgil, *Aeneid I.203.*

Quaeque ipse miserrima vidi
Et quorum pars magna fui.

- Virgil, *Aeneid II.5.*

Is not life a hundred times too short for us to bore ourselves?

- Friedrich Nietzsche, *Also sprach Zarathustra.*

You are young and your bitter recollections have time to change themselves to tender remembrances.

- Alexander Dumas, *The Three Musketeers.*

Most of what follows is true.

- Introduction to Butch Cassidy and the Sundance Kid.

Contents

List of Figures

List of Tables

Chapter 1

Introduction to Gluonic States

1.1 The basic constituents of matter

The quest for the fundamental structure of matter perhaps represents mankind's longest scientific endeavour. Through the advances in atomic and nuclear physics of the late 19th and early 20th centuries, and in particle physics over the last 50 years the answer is at long last emerging. At its most basic level we now believe that the whole of known matter can be described in terms of 6 quarks and 6 leptons (point-like spin 1/2 fermions), together with their antiparticles (with the same mass but reversed internal quantum numbers, e.g. charge, baryon and lepton number). This structure of matter was indicated by the proliferation of strongly interacting hadron states discovered since the 1950's. Interactions between these particles are of four fundamental types - Gravity, Electromagnetism, Strong and Weak forces. The forces themselves are mediated by the exchange of bosons (integral spin particles). The situation is summarised in tables 1.1 and 1.2, where spin is given in units of $\hbar$ and charge in units of the electron charge e. This theory is known as the *Standard Model* [1, 2]. It has been extremely successful in explaining particle physics up to present energy scales, but it still suffers from some deficiencies, such as its inability to predict particle masses, or why there are three generations of fermions. Also many parameters have to be fixed by experiment (e.g. Weinberg mixing angle). Several extensions to the Standard Model have been proposed, such as Supersymmetry, to overcome these difficulties, with the ultimate aim being a unified single theory of particle interactions with as few experimentally input parameters as possible. It is the role of experimental particle physics to validate (or disprove) the Standard Model and subsequent extensions by extensive and precise tests.

1.2 Quantum Electrodynamics

The electromagnetic force is perhaps the most well-studied and well-understood of the four forces, due to its familiar and overwhelming presence in everyday life. It is responsible for keeping the electrons orbiting the atomic nucleus and for the molecular forces responsible for most everyday phenomena, and as such governs the chemical and biological processes of life. The combining of electricity and magnetism into electromagnetism as formulated by Maxwell in the mid 19th century was perhaps the first example of a unification theory. This century has seen the theory expanded to include relativity and quantum field theory [3] to give Quantum Electrodynamics - QED. This theory describes the electromagnetic interaction of fermions, represented in terms of complex fields, by the exchange of field quanta, in this case photons. The emission and absorption of these field quanta by a pair of fermions results in a change in their momentum, which corresponds to a force between them. This theory for the response of quarks and charged leptons to an electromagnetic field can be derived from applying perturbation theory to the Dirac equation

$$(i\gamma^\mu \partial_\mu - m)\psi = 0 \tag{1.1}$$

which describes free spin 1/2 quarks and leptons, with the electromagnetic field interaction as described by Maxwell's equations put in by hand, or by applying local gauge invariance[1] to the free particle Lagrangian

$$\mathcal{L} = i\overline{\psi}\gamma^\mu \partial_\mu \psi - m\overline{\psi}\psi \tag{1.2}$$

[1]The complex fields describing fermions possess an unobservable quantum mechanical phase, which can vary from space-time point to point. Theories which are invariant under arbitrary changes to the phase of the fields are said to possess local gauge invariance.

Type	Charge	Spin	Generations		
quarks	$+\frac{2}{3}$	$\frac{1}{2}$	u	c	t
	$-\frac{1}{3}$	$\frac{1}{2}$	d	s	b
leptons	-1	$\frac{1}{2}$	e	μ	τ
	0	$\frac{1}{2}$	ν_e	ν_μ	ν_τ

Table 1.1: Quark and lepton generations.

Force	Carrier	J^P
Strong	Gluon	1^-
Weak	$W^\pm$	1
	Z^0	1
Electromagnetic	Photon	1^-
Gravity	Graviton	2^+

Table 1.2: The fundamental interactions.

where the electromagnetic field, the existence of the massless photon as the intermediate vector boson of the interaction and conservation of electric charge come out as a natural consequence [4].

The beauty of QED is that the complexities of the field theory behind it can be effectively hidden by the use of Feynman diagrams. Such a diagram is shown in Fig 1.1 for the reaction $e^+e^- \rightarrow \mu^+\mu^-$. Not only are these diagrams very useful

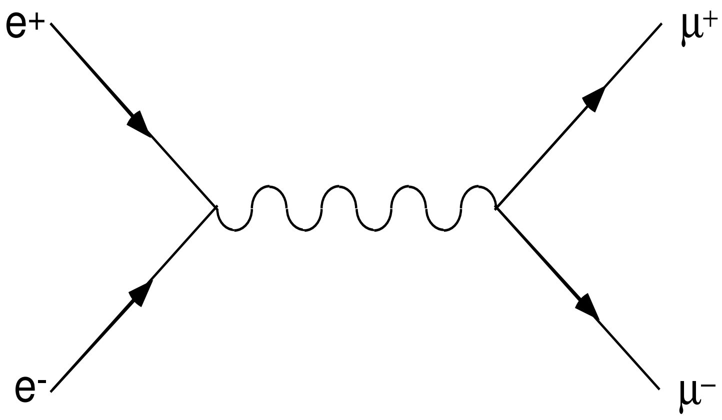

Figure 1.1: Feynman diagram for $e^+e^- \rightarrow \mu^+\mu^-$

pictorial representations of the interaction mechanism, but they can also be used for calculation of reaction amplitudes by the application of the Feynman rules. These rules involve assigning factors to the external lines to represent the particles, a propagator factor to the internal line to represent the dynamics of the mediating boson (photons in the case of QED), and vertex factors to represent the coupling of the particles to the mediator - in effect representing the strength of the interaction. The invariant amplitude $\mathcal{M}$ is obtained by summing the contributions from all the distinct diagrams for the process under consideration.

1.2.1 Charge Screening and Renormalizability

In terms of QED an electron is not just a pointlike object of charge e. It can emit photons which can convert into e^+e^- pairs which can annihilate back into photons.

Thus QED predicts the electron will be surrounded by a cloud of virtual e^+e^- pairs, which becomes polarised such that the positrons are closer to the source electron. This is shown in Figs 1.2a and b. Thus on approaching the electron one penetrates deeper into this polarised cloud, and the effective charge measured increases. This is shown in Fig 1.2c. QED thus predicts the strength of the electromagnetic interaction increases on probing deeper into the electron, an effect known as charge screening. The magnitude of this effect can be calculated in QED by considering all possible contributions to the electron charge cloud, and leads to an important feature of QED. One such contribution is shown in Fig 1.3. The calculation of the amplitude due to this diagram causes a problem. Although 4-momentum is conserved at each vertex, the momentum p circulating around the e^+e^- loop is unrestricted, being able to take values between zero and infinity. Thus the contribution from this diagram is divergent, running off to infinity. In fact all such higher order diagrams, involving loops, are divergent. The problem, however, lies in definition. The electron charge associated with the first order interaction (for example at the electron vertex in Fig 1.1) is not the charge measured in experiment. This is the bare charge e_0. The measured charge is the bare charge clothed by the higher order loop corrections. Thus it is possible to reparameterise or renormalize the amplitude $\mathcal{M}$ to be in terms of the measured charge e, measured at some arbitrary 4-momentum transfer μ^2. The infinities of Fig 1.3 are absorbed into e, and the higher order corrections, when formulated in terms of e are all finite. This property of QED is called *renormalization [5],* and it is a vital property of any gauge field theory, as it means that at the expense of introducing a finite number of arbitrary constants which must be measured experimentally (in QED these are h, m, e) the predicted amplitudes for physical processes remain finite at all energies and to all orders of the coupling constant $\alpha = e^2/4\pi\hbar c$. In fact coupling constant is a misleading term, as due to the higher order corrections (the charge screening effect) α varies with the energy it is measured at. Calculations show

$$\alpha(Q^2) = \frac{\alpha(\mu^2)}{1 - \frac{\alpha(\mu^2)}{3\pi}\log(\frac{Q^2}{\mu^2})} \tag{1.3}$$

Figure 1.2: a) An electron surrounded by virtual photons and e^+e^- pairs. b) The polarisation of the charge cloud surrounding the electron. c) How the measured electron charge varies with distance from the 'bare' charge.

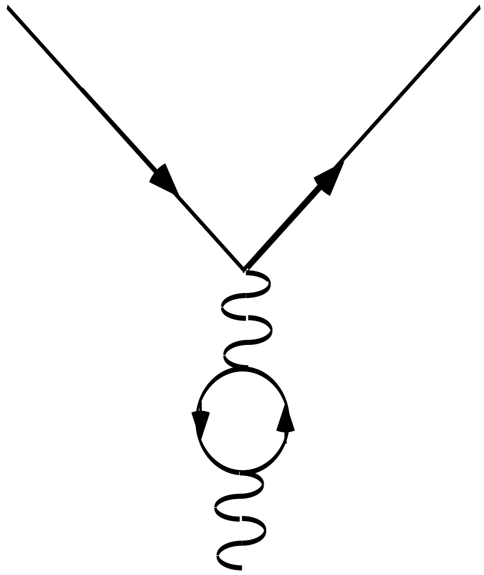

Figure 1.3: Feynman diagram for the $O(\alpha^2)$ contribution to the electron charge.

where Q^2 is the 4-momentum of the photon probing the electron charge, and μ^2 is the (arbitrary) value of Q^2 at which the charge was measured for renormalization. The variation of α with Q^2 is very small, increasing from $\approx 1/137$ at atomic energies to $\approx 1/128$ at $Q^2 = 100$ GeV. QED has been extensively tested, for example in the Lamb shift of atomic spectra, and in the anomalous magnetic moment of the electron and muon, and has given results accurate to 1 part in a million [6].

1.3 Quantum Chromodynamics

The immense success of QED as a calculational scheme prompted theorists to try and copy it to explain the strong interactions between quarks. However the strong interaction has subtle differences from the electromagnetic one, which have far reaching consequences. Whereas QED has 2 types of charge, + and −, which generate the electromagnetic field, the strong interaction requires 6 strong 'charges', called colour. Quarks can carry one of 3 colours (red, blue or green), and the antiquarks the appropriate anticolours. The existence of this colour degree of freedom was originally postulated to explain the existence of the spin 3/2 Ω^- and Δ^{++} baryons, which, being composed of 3 identical quarks in the same spin up configuration, would violate the Pauli Exclusion Principle unless each quark carries a different colour. However there is also experimental evidence for colour, for example in the ratio $\sigma(e^+e^- \rightarrow \text{hadrons})/\sigma(e^+e^- \rightarrow \mu^+\mu^-)$, or in the decay rate of $\pi^0 \rightarrow 2\gamma$.

Interquark interactions are invariant under colour interchange (or more exactly under rotations in colour space), and so can be described by the SU(3) symmetry group. Applying local gauge invariance to the free quark Lagrangian in analogy to QED, but using the SU(3) colour group in place of the U(1) group of QED, leads to the following features of Quantum Chromodynamics (QCD), the field theory of the strong interaction :-

- 8 colour fields are required, instead of the single electromagnetic field of QED. More fields are required as there are 3 quark fields whose phase changes need to be compensated for to maintain the invariance of the Lagrangian.

- These carriers of the colour force, called gluons, are spin 1 massless bosons, just like the photon.

- Unlike the photon, which is electrically uncharged, the gluons carry colour charge just like the quarks. This implies that gluons can interact amongst themselves. Thus is due to the fact that the generators of the SU(3) colour group are matrices, which do not all commute with each other. The SU(3) group is said to be Non-Abelian, and leads to gluon-gluon coupling terms appearing in the QCD Lagrangian. The generators of the U(1) group of QED are real numbers, which of course commute, and so QED is said to be an Abelian theory, and no photon-photon coupling appears.

- QCD, like QED is renormalizable - the divergences of higher order loop diagrams can be absorbed by redefining the colour charge to be a physically measurable parameter.

A typical quark-quark interaction mediated by a gluon is shown in Fig 1.4. A red quark (R) switches colour with the blue quark (B) at the bottom of the diagram. To achieve this colour exchange, which causes the strong interaction between the quarks, the gluon must carry the colour charge $R\overline{B}$. The colour composition of the

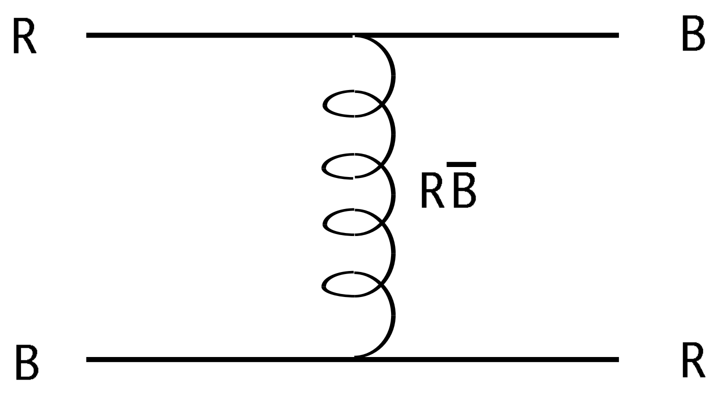

Figure 1.4: A quark-quark interaction mediated by a gluon.

8 gluons is :-

$$R\overline{B}, R\overline{G}, B\overline{G}, B\overline{R}, G\overline{R}, G\overline{B}, \frac{R\overline{R}-B\overline{B}}{\sqrt{2}}, \frac{R\overline{R}+B\overline{B}-2G\overline{G}}{\sqrt{6}}.$$

With 3 colours and 3 anticolours, 3^2 gluon combinations would be expected, but the singlet state

$$\frac{R\overline{R}+B\overline{B}+G\overline{G}}{\sqrt{3}}$$

does not carry any net colour and so cannot play the part of a gluon carrying colour between quarks.

1.3.1 Colour screening in QCD

As in QED, a quark will continually emit gluons, which can turn into quark-antiquark pairs, as shown in Fig 1.5a, which as in QED produce a shielding effect on the colour charge of the quark. However, due to the extra self coupling of gluons in QCD, gluons can also form gluon-gluon pairs, as shown in Fig 1.5b. It turns out that certain polarisation states of this pair produce an anti-shielding effect. This effect is so large that it reverses the behaviour found in QED, i.e. the effective colour charge decreases on approaching the quark, as shown in Fig 1.5c. The QCD calculation for the running coupling constant $\alpha_s(Q^2)$ gives

$$\alpha_s(Q^2) = \frac{12\pi}{(33 - 2n_f)\log(Q^2/\Lambda^2)} \tag{1.4}$$

where Λ is a mass scale introduced due to renormalization, and must be determined experimentally, and n_f is the number of quark flavours.

1.3.2 Confinement and Hadron States

Equation 1.4 shows that for $n_f \leq 16$, $\alpha_s(Q^2)$ decreases as Q^2 increases. This implies two things :-

- For high energy interactions with large Q^2, the quarks interact with colour fields of reduced strength. As $Q^2 \to \infty$ then $\alpha_s(Q^2) \to 0$, and the quarks become essentially free, non-interacting particles. This is known as asymptotic freedom, and allows QCD calculations to be performed in this region by perturbation theory.

- As quarks separate, the colour interaction becomes stronger ($\alpha_s(Q^2)$ increases). This allows multi-gluon exchange to become probable, and due to the mutual interaction of the gluons, the colour field lines of force become squeezed into a tube, as shown in Fig 1.6a. In QED the electromagnetic field lines of force spread out through space as there is no photon self-coupling to contain them, as shown in Fig 1.6b. Thus QCD predicts that as quarks separate the potential increases as $V(r) \sim \lambda r$. This form of potential has been seen experimentally, for example in the energy levels of heavy quarkonium ($\mathrm{c\overline{c}}$ and $\mathrm{b\overline{b}}$) systems. It implies that an infinite amount of energy is needed to free a quark, and so under normal conditions quarks are bound into hadron particle states. This is known as confinement.

QCD also predicts what sort of states can exist. The colour degree of freedom has never been observed experimentally, due to the confinement of the individual quarks and gluons. Thus all particle states are postulated to be colourless, or more precisely

Figure 1.5: A quark surrounded by a cloud of virtual gluons producing a) quark-antiquark pairs and b) gluon-gluon pairs. c) How the measured quark colour charge varies with distance from the bare quark.

Figure 1.6: a) The colour field lines of force between two quarks. b) The electromagnetic lines of force between two charges.

the colour wavefunction of the state is unchanged by rotations in colour space. This accounts for the 2 types of quark bound state so far discovered :-

$$\text{Baryons} = \mathrm{qqq}$$

$$\text{Mesons} = \mathrm{q}\overline{\mathrm{q}}$$

where the baryons have equal amounts of each colour (or anticolour for the antibaryons), and the mesons have equal amounts of colour and anticolour.

1.4 Meson Multiplets

The SU(3) symmetry group is also a very useful way of classifying meson states. The fundamental representation is a triplet, consisting of the up, down and strange quarks. The nine possible combinations of $\mathrm{q}\overline{\mathrm{q}}$ group themselves into an octet and a singlet according to SU(3):

$$\mathbf{3} \otimes \overline{\mathbf{3}} = \mathbf{8} \oplus \mathbf{1}$$

where under pure SU(3) group operations the octet states transform amongst themselves and do not mix with the singlet state. A typical meson nonet and the

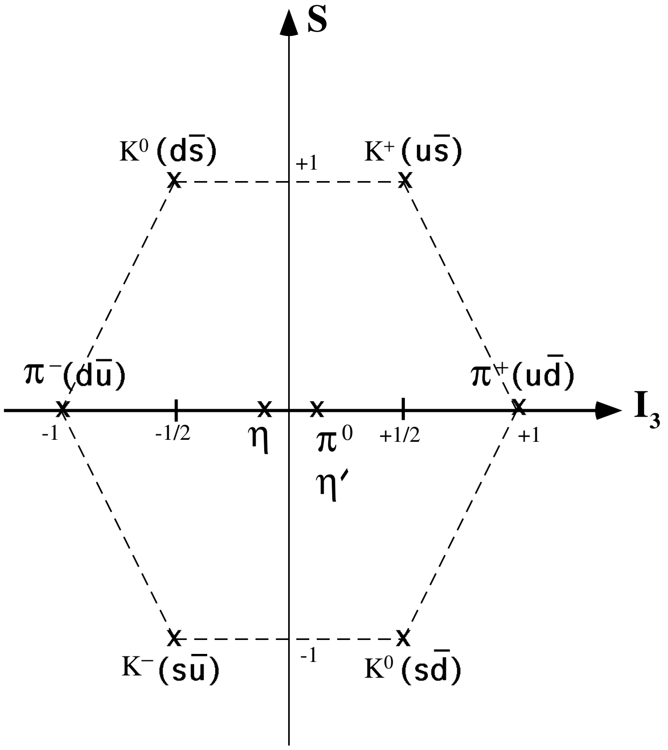

Figure 1.7: The quark content of a typical SU(3) meson nonet.

quark content of its members is shown in Fig 1.7. Whereas SU(3) of colour is believed to be an exact symmetry, SU(3) of flavour is much more approximate. For example in the lightest nonet, the 0^- pseudoscalars, the kaon is more than 3 times as massive as the pion, which is explained in the quark model by the much larger bare mass of the strange quark compared to the up and down quarks. The SU(3) symmetry is also broken by the mixing of pure SU(3) states with identical quantum numbers to produce the physical states. For example, in the 1^- nonet, the $\mathrm{I} = 0$ neutral octet and singlet states mix in such a way that the physical states are almost purely made from strange and non-strange quarks :-

$$\phi \approx \mathrm{s\bar{s}}, \omega \approx \sqrt{\frac{1}{2}}(\mathrm{u\bar{u}} + \mathrm{d\bar{d}})$$

which is borne out by the decay modes and small width of the ϕ .

Flavour SU(3) is now mainly of historical value. The underlying quark model contains most of the predictive power. As quarks have spin $\frac{1}{2}$ the total intrinsic spin S of a meson can be either 0 or 1. The total spin J of the meson is then the vector sum of its intrinsic spin and the relative orbital angular momentum L between the quark and antiquark. The parity of the meson is then given by :-

$$\mathrm{P} = -(-1)^{\mathrm{L}}$$

Orbital Ang Mom	Spin	J^{PC}	$I = 1$	$I = \frac{1}{2}$	$I = 0$	Typical Mass (MeV)
$L = 0$	$S = 0$	0^{-+}	π	K	η, η'	500
	$S = 1$	1^{--}	ρ	K^*	ω, ϕ	800
$L = 1$	$S = 0$	1^{+-}	$b_1(1235)$	$K_1(1400)$	$h_1(1170), ?$	1250
		2^{++}	$a_2(1320)$	$K_2^*(1430)$	$f_2(1270), f_2'(1525)$	1400
	$S = 1$	1^{++}	$a_1(1260)$	$K_1(1270)$	$f_1(1285), f_1(1510)$	1300
		0^{++}	$a_0(980)$	$K_0^*(1430)$	$f_0(1400), f_0(975)$	1150

Table 1.3: Meson multiplets and their quantum numbers.

and the charge conjugation parity of the neutral nonet members (and thus of the whole nonet) by :-

$$C = (-1)^{L+S}$$

Table 1.3 shows some examples of meson nonets and their quantum numbers. As well as orbital excitations there can also be radial excitations (just as in atoms) - i.e. nonets with the same quantum numbers but at higher mass.

1.5 Non $-$ $q\overline{q}$ mesons

In section 1.3.2 it was stated that there are two types of bound quark states, mesons and baryons. However, since gluons can self interact then QCD predicts there should also exist bound states which contain gluons. For meson type states (with integral spin), these can be composed totally of gluons (e.g. gg), in which case they are known as *glueballs* , or they can be a mixture of quarks, antiquarks and gluons (e.g. $q\overline{q}g$), known as *hybrids*. Thus an important test of QCD is to find and identify such gluonic non $-$ $q\overline{q}$ mesons.

1.5.1 Characteristics of gluonic states

It would be extremely useful in the search for gluonic matter if we could predict the properties (e.g. mass, spin, decay modes) of such states. Unfortunately, due to the large strong coupling inside hadrons, mathematical solutions to QCD are as yet impossible. There is no way at present to derive confinement from first principles. Models and approximations inspired by QCD have to be used. Thus no detailed predictions on glueball properties are possible. However by developing and refining such models to explain the properties of normal hadronic matter, predictions of the properties of gluonic matter will improve. Thus an essential part of the search for gluonic states is to improve our knowledge of conventional hadronic spectroscopy. A review of various models and their predictions is given in reference [7]. The agreement between the various models is only fair, but they all predict the lightest glueballs to be in the mass range 1.0 to 2.0 GeV/c^2, with the lowest lying glueballs expected to have $J^{PC} = 0^{++}$, 0^{-+} and 2^{++}, and the lowest lying hybrids to have $J^{PC} = 0^{-+}$, 1^{-+}, 1^{--} and 2^{-+}. Predictions on glueball widths vary so much as to be no useful guide, with some models giving widths so large as to make them unobservable. Glueballs are singlets in colour and flavour, are electrically neutral and carry no isospin, so they would be expected to decay into isoscalar final states in a flavour symmetric way, although it has been argued that they may couple preferentially to kaons. Also as photons do not couple directly to gluons, radiative decays are expected to be suppressed compared to a quark meson at a similar mass.

1.5.2 The search for gluonic states

Thus it seems that gluonic mesons do not exhibit strikingly different properties to normal mesons. Searches for them must rely on the following guidelines [8]

1. Look for 'oddball' states, i.e. states having J^{PC} quantum numbers not allowed for normal meson states, e.g. 1^{-+}, as such a state must be exotic.

2. Look for extra states, i.e. ones having J^{PC} quantum numbers of an already completed meson nonet, but with sufficiently low mass so as to make it unlikely

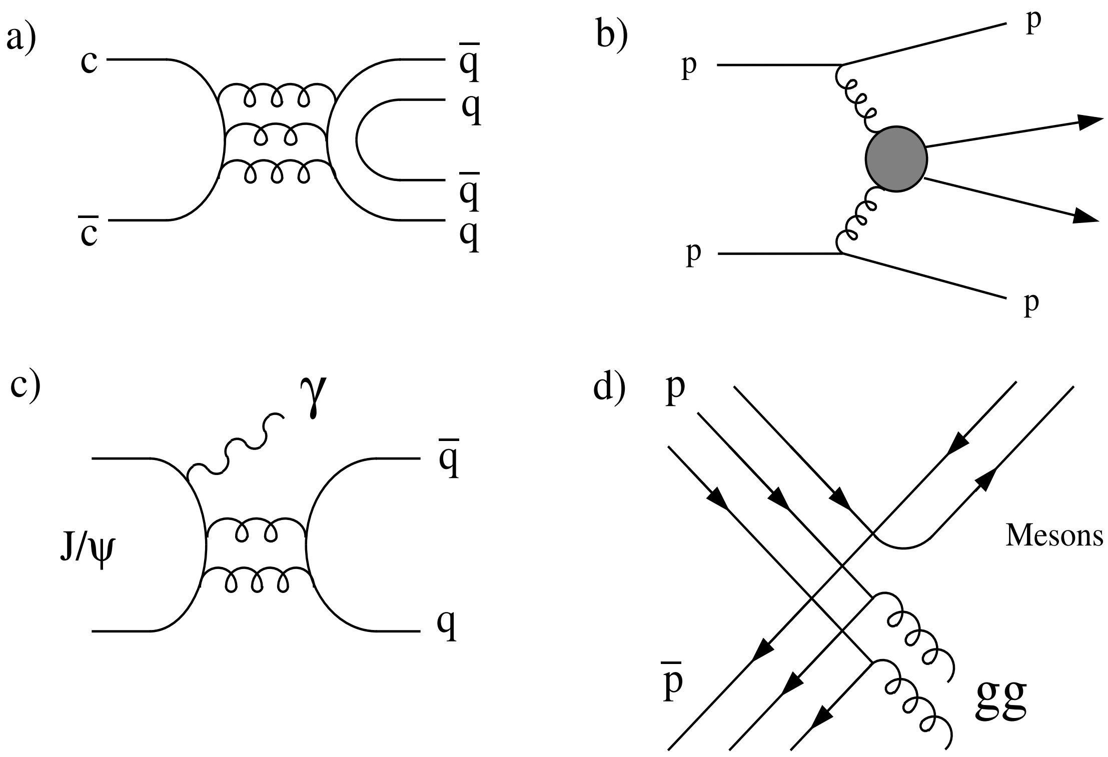

Figure 1.8: Examples of gluon rich processes where gluonic states might be found.

to be a member of the next radially excited nonet. For example, the lowest lying 1^{++} nonet is complete as shown in table 1.3, but there is an extra state, the $f_1(1420)$, which is too low in mass to be in the first radially excited nonet. This implies that the $f_1(1420)$ may have an exotic nature. The problem with this method is that only the first few nonets are fully established. The higher mass nonets where it is expected that the lowest mass gluonic states should occur are already crowded with standard $q\overline{q}$ states and their radial excitations so that the groupings into multiplets are very uncertain. Thus any new gluonic resonances would be difficult to prove due to our poor understanding of the normal states. This is another reason why conventional meson spectroscopy is complementary to gluonic spectroscopy.

3. Look for states produced in gluon rich processes, as compared to other production mechanisms. Examples of such processes are given in Fig 1.8.

   - The hadronic (Fig 1.8a) or radiative (Fig 1.8c) J/Ψ decay.

- Central production via Double Pomeron Exchange (DPE). as shown in Fig 1.8b. The Pomeron is believed to be a multi-gluon state, thus this reaction is effectively gluon-gluon scattering. This is the reaction mechanism studied by the WA91 experiment at CERN, and will be discussed in the following chapter.
- Proton - antiproton annihilation (Fig 1.8d) where the annihilation region is a source of gluons where gluonic states could be produced.

Comparison of states produced in these reactions with those produced in reactions such as $\gamma\gamma$ collisions and π or K induced peripheral reactions where gluonic states should be suppressed should give indications as to which are the potential gluonic states.

Thus it seems unlikely that the discovery of a single exotic state would prove the existence of gluonic states. Only by building up a series of gluonic candidates, and examining in detail their production and decay channels, will gluonic states be conclusively proved. This indeed was the same for the quark model - there is no meson or baryon state that conclusively proves the quark model to be correct. Only through the discovery of many states, and the measurement of their properties, was the quark model finally accepted.

Chapter 2

The WA91 Experiment

2.1 Introduction

The WA91 experiment [9] is designed to study exclusive final states, with good particle identification, formed in the reaction

$$pp \rightarrow p_f(X^0)p_s$$

at 450 GeV/c incident proton momentum, where the subscripts f and s denote the fastest and slowest particles in the laboratory, and X^0 denotes the centrally produced system which decays into neutral and charged final states. The experiment follows on from the original WA76 experiment carried out in 1982 using a π^+/p beam of 85 GeV/c, and the further run in 1986, using a 300 GeV/c proton beam. A summary of the results of these experiments is given in [9]. Fig 2.1 shows an example of the required reaction in the centre of mass and laboratory frames. The reaction is believed to proceed *via* a Double Pomeron Exchange process (DPE), where the Pomeron is thought to be a multi- gluonic object. Thus triggering on this reaction involves finding the fast and slow protons. This type of exchange is predicted to be dominant over other mechanisms at high centre of mass energies and when the Feynman x (x_F) of the outgoing protons is near to one. DPE is also believed to be enhanced when the four momentum |t| transferred at the exchange vertices is small. Offline cuts on x_F and |t| can be used to increase the DPE events over background.

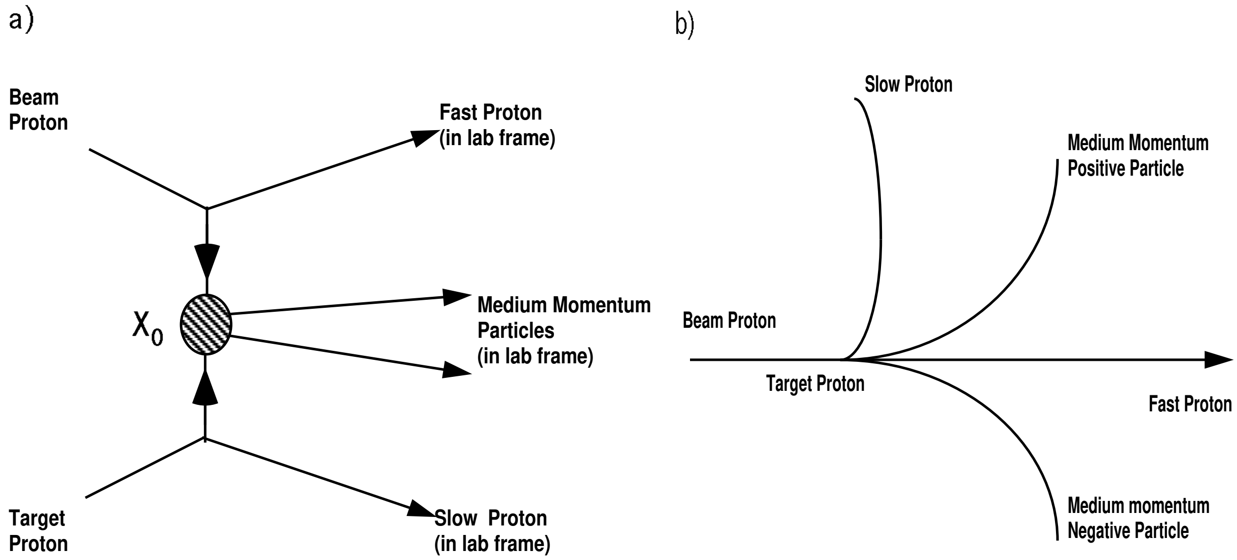

Figure 2.1: Central production as viewed from a) the centre of mass and b) the laboratory frame.

2.2 Motivation

The original WA76 experiment in 1982 was concerned principally with looking at strange channels, such as K^+K^- and K^0K^0 where other experiments had seen possible gluonic structures, and also channels containing pions such as $\pi^+\pi^-$. However experiments such as Crystal Barrel, Mark III and GAMS have examined channels containing neutrals, such as $\eta\eta$ and found potential exotic states, and so a study and comparison of such channels in central production was considered interesting. It is also an advantage to be able to study many channels in the same experiment so that decay branching ratios for various mesons can be worked out. Thus in 1986 the experiment was repeated with a 300 GeV/c proton beam (the WA76$'$ experiment), and the Geneva Photon Detector (GPD) electromagnetic calorimeter to detect neutrals. However since the principal goal of this experiment was to increase statistics on charged channels, the calorimeter was placed a long way from the target, consequently having low acceptance, and statistics collected on neutral channels was low. To overcome this problem, the WA91 experiment was proposed [9]. This was designed to get high statistics on both neutral and charged channels by the following means :-

- Using a 450 GeV/c momentum proton beam. DPE reactions are predicted to be enhanced at higher energies.

- Increasing the acceptance of the experiment. This was achieved by adding detectors to measure events with a slow proton on both sides of the target (previously only slow protons on one side were detected) and by increasing the fast proton acceptance by a factor 2.5 using improved microstrips.

- By splitting the data taking into 2 parts. The first part was optimised for the detection of neutral particles, with the calorimeter placed near the target to increase acceptance. This set-up was used for a 30 day data taking run in July 1991, and a 43 day data taking run in November 1992. The second part is to be optimised for charged track detection, with Cerenkov counters placed near the target for good particle identification, and the calorimeter placed after these. The first data taking run using this set-up was performed in May 1994.

The experimental layout described below is from the 1992 run, as it is on these data that the analysis presented in this thesis was performed. The layout for this part of the experiment is shown in Fig 2.2.

2.3 The Experimental Set-up

WA91 uses the Ω spectrometer which is a multi-user detector designed for measuring interactions with many final state particles. It consists of a pair of superconducting Helmholtz coils capable of producing a field of up to 1.8 T, although in this experiment the field used is 1.35 T. The apparatus consists of several parts.

1. The incident beam direction is measured accurately using 10 (5y and 5z planes) 20 μm pitch micro-strip detectors. These detectors consist of very thin strips of silicon held at a biasing voltage of around 50V, so that the silicon becomes depleted of charge carriers. Charged tracks passing through the silicon ionise it, and the resultant charge is amplified and recorded. Since each strip is read out separately, very accurate spatial resolution is possible. Three groups of

Figure 2.2: Layout of the Ω spectrometer for WA91.

Name	Planes	Pitch	Channels	Dimensions	X position (mm)
BEAM1	4 (ZYZY)	20μm	512	10.24x10.24	-3998/-3988/-3942/-3931
BEAM2	2 (ZY)	20μm	512	10.24x10.24	-3326/-3315
BEAM3	4 (ZYYZ)	20μm	512	10.24x10.24	-2729/-2718/-2686/-2676
VERTEX	4 (ZYYZ)	25μm	2048	51.2x51.2	-969/-944/-919/-894
5m A1	4 (ZYZY)	25μm	2048	51.2x51.2	5330/5335/5380/5405
10m A2	4 (ZYZY)	25μm	2048	51.2x51.2	10462/10487/10512/10537
12m A2	2 (YY)	50μm	2048	51.2x51.2	12501/12553

Table 2.1: Positions of the microstrips used in the 1992 run.

microstrips, fixed at various points along a rigid optical bench, are used to detect the beam particle, the positions of which are given in Table 2.1.

2. The target is a 60 cm long cylinder of liquid hydrogen in a mylar and aluminium container, representing 15% of an interaction length. This target has the advantage that the interactions are very clean (i.e. pp), unlike solid targets such as beryllium, where nuclear effects are introduced.

3. A set of 4 (2y and 2z planes) 25μm pitch micro-strip detectors just after the target to give a very accurate point in the field for measuring the fast proton momentum, and also to improve accuracy for finding V^0's.

4. To measure the slow proton trajectory, Multi-Wire Proportional Chambers (MWPC) called C chambers are placed on either side of the target. This doubles the acceptance over WA76 which had chambers on only one side of the target. Each set of C chambers consists of 8 modules, with each module consisting of 2 planes of wires (Y, U or V where the U and V planes are inclined at $\pm$ 10.14^o to the vertical Y plane).

5. To measure the medium momentum tracks coming from the central system the Ω A and B MWPC chambers are used. The B chambers have the same layout as the C chambers, whilst the A chambers consist of 7 modules each consisting of 3 planes of wires (Y,U,V). All the chambers (A,B,C) have 2 mm

wire spacing and a gas filling of iso-butane and alcohol. There are also 2 high precision drift chambers (DC1 and DC2) further downstream, consisting of 4 planes (Y,U,Y,V), with each plane having a 2.5 cm spacing between the sense and field wires. In addition there is a 1mm spacing MWPC placed just after the vertex microstrips, with 4 planes of wires (YZUV), in order to give extra track hits for reconstructing the fast proton and charged tracks from the centrally produced system.

6. The fast proton is measured using 3 sets of microstrip detectors. The first 2 sets have 4 planes (ZYZY) and a 25μm pitch and are placed at approximately 5m and 10m from the centre of Ω, as shown in Table 2.1. The final set consists of 2 planes (YY) with 50μm pitch placed approximately 12m from the centre of Ω. In addition are 2 sets of 1mm wire spacing MWPC's, each with 4 planes of wires (ZYUV and ZYZY) at 16.5m and 17m from the Ω centre.

7. The electromagnetic calorimeter OLGA (Omega Lead Glass Array) placed 6 metres downstream (Fig 2.3). This consists of 3 modules :-

   - An array of 18x19 lead glass blocks (type SF5) with surface 14x14 cm^2 and depth 47 cm, corresponding to 18.5 radiation lengths. Each block is wrapped in mylar to stop light leaks. The central block was removed to allow free passage of the beam or fast proton (in the first WA91 run the central 4 blocks were removed and replaced with a 4x4 array of smaller lead glass blocks (7x7x47 cm ^{3}) to improve positional resolution. However their performance during the run was poor, and so they were removed from the second run).

   - The samplers, which are large lead glass slabs (type F2W) of surface area 14x145 cm^2 and depth 10 cm, corresponding to 3 radiation lengths. These are arranged in a column of 19 samplers down the left and right halves of OLGA. A photon incident on the samplers will start an electromagnetic shower within it, the barycentre of which is calculated by the scintillator fingers (see next item) and allows an accurate measurement of incident

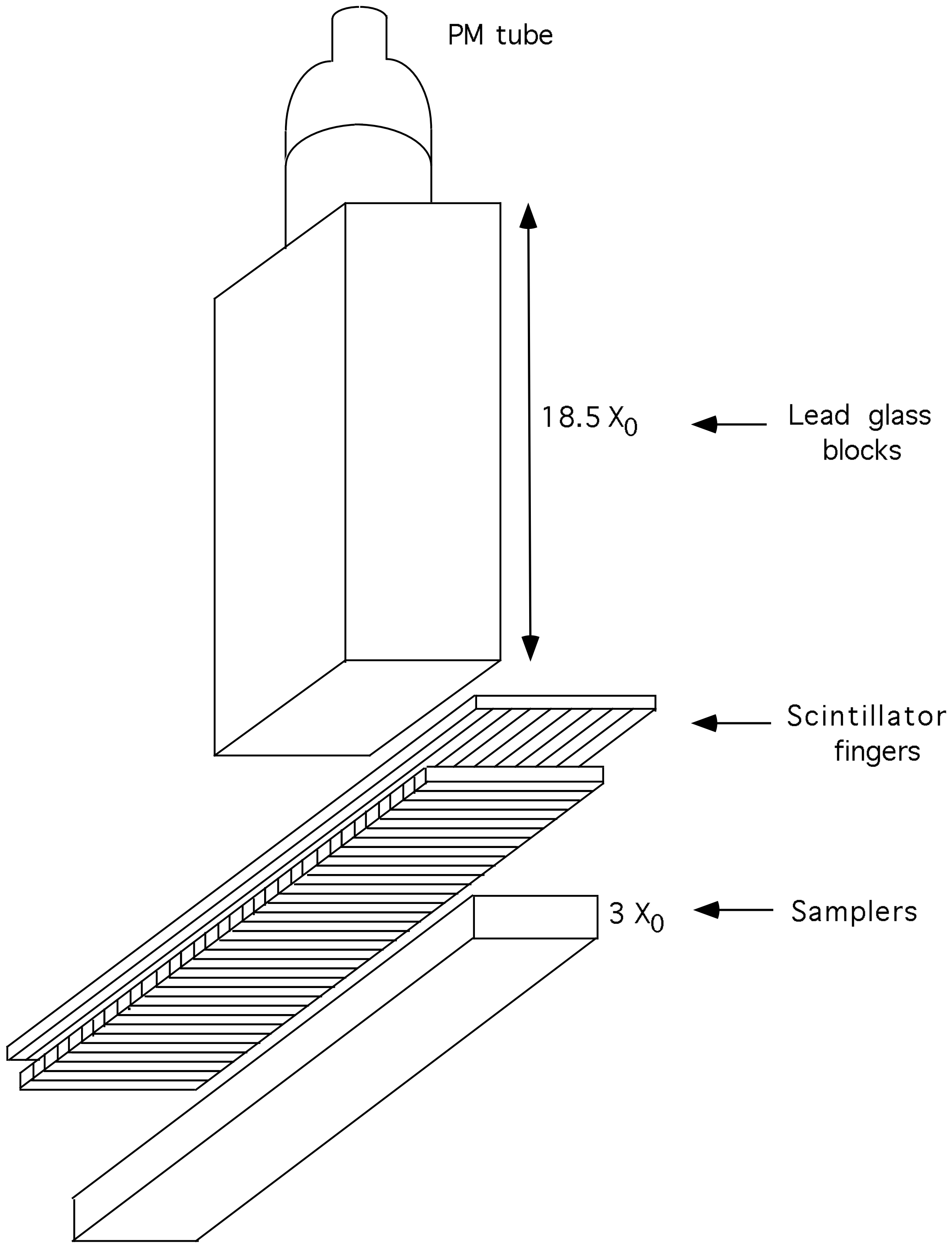

Figure 2.3: Schematic diagram of OLGA.

photon position. The amount of energy deposited in the sampler also gives a rough idea of the energy of the photon, which is more accurately measured in the lead glass array.

- The positional detector made up of scintillator fingers in 4 half planes - 2 half planes of horizontal fingers, with each half plane made up of 180 fingers (length 147cm, width 1.53 cm, depth 1 cm) and 2 half planes of vertical fingers, with each half plane made up of 180 fingers (length 152 cm, width 1.53 cm, depth 1 cm). The signals in the horizontal and vertical fingers, induced by the shower started in the samplers, can be used to increase the measurement precision of the incident particle position beyond the finger width. NA14 claim the final position resolution to be $\pm$ 4 mm [10].

The testing of the various modules of OLGA will be the subject of chapter 4.

2.4 The Trigger

In order to select reactions of the type shown in Fig 2.1 in preference to competing reactions, it is necessary to use a trigger which only writes events to tape that satisfy certain requirements, namely having a fast and slow proton, and 2 or more medium momentum tracks. To achieve this the trigger is split into several sections.

2.4.1 The Beam Trigger

Fig 2.4 shows the apparatus used to trigger on and record a beam proton. There are two trigger scintillators, S2 and S4, which are square slabs of side 2.5cm and 0.8cm respectively and thickness 5mm, and two veto scintillators, V2 and V4, which are square slabs of side 17cm, but with central holes of diameter 15mm and 8mm respectively. A beam trigger is defined as $S2.\overline{V2}.S4.\overline{V4}$. Extra logic also ensures there is no other beam particle within 50ns of this trigger, thus ensuring that no interaction interferes with the one being considered.

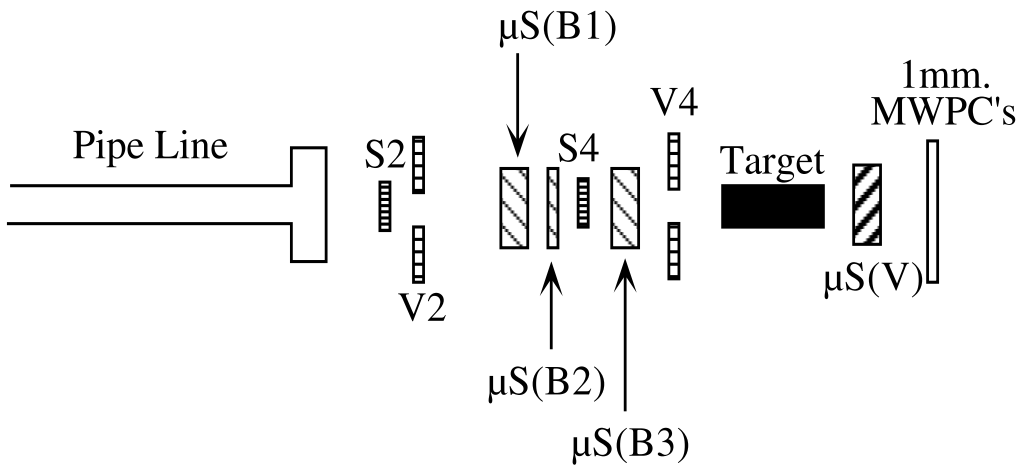

Figure 2.4: The beam trigger apparatus.

2.4.2 The Slow Proton Trigger

Fig 2.5 shows the apparatus used to trigger on and record the slow proton. It consists of two parts. The target box (see Fig 2.2b) is an open ended box surrounding the target and made up of 10 slabs, TB1-TB10, with TB1 (TB(L)) on the left side of the target and TB2 (TB(R)) on the right side (in the Omega system the left side is in the direction of increasing y). Each slab is 60cm long, with slabs 3-10 being 1cm thick and TB(L) and TB(R) being 0.5cm thick. The second part involves the slow proton counters SPCL and SPCR, which each consist of 14 scintillator slabs (active length 56cm, thickness 2cm) positioned so as to accept slow particles tracked in the C chambers. A slow particle trigger on the left side is defined by a coincidence between hits on TB(L) and either 1 or 2 slabs of SPCL. To reduce target diffraction (see Fig 2.6) which produces several slow particles, no hits are allowed on any other slab of the target box. The right slow particle trigger is the same but replacing TB(L) with TB(R) and SPCL with SPCR. The signal produced in the slow proton counters can be used to distinguish between protons and pions. This is done by taking the signals from each of the 14 slabs of the SPC (left or right), normalising them to take account of the different photomultiplier gains, and then adding them together. The resulting spectrum for the 1991 run is shown in Fig 2.7. A clear band corresponding

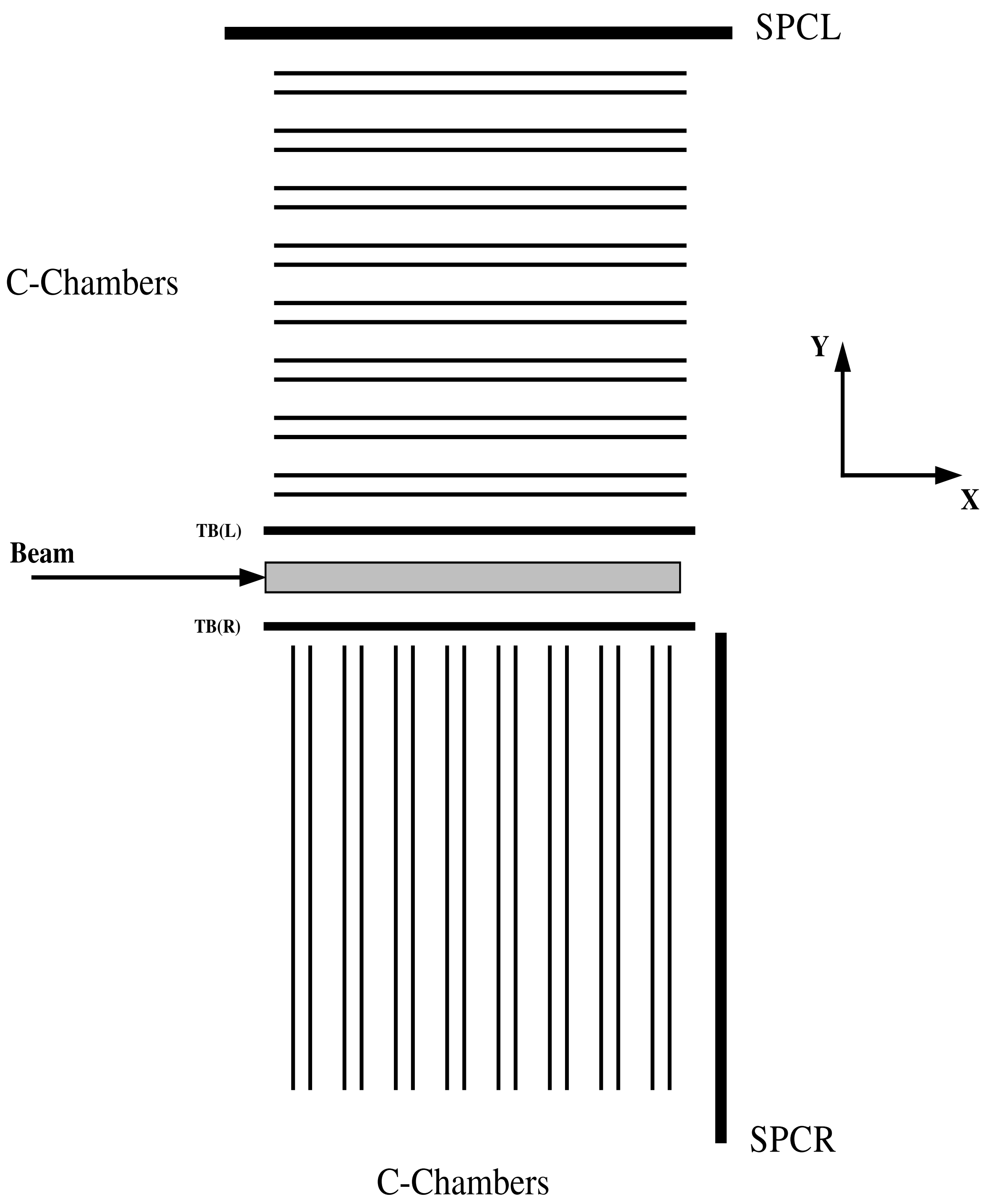

Figure 2.5: The slow proton trigger layout.

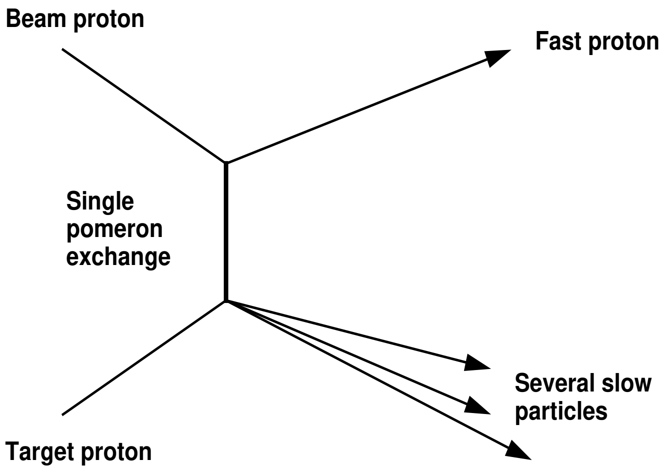

Figure 2.6: Target Diffraction.

to slow protons can be seen. The initial rise in energy deposited (ADC counts) at low momentum corresponds to protons being stopped in the SPC scintillator, the maximum corresponding to protons which are just stopped within the scintillator. The subsequent fall corresponds to protons passing through the scintillator, where the energy deposited is determined by the Bethe-Block formula [11]. In this non-relativistic region for protons the rate of energy loss with distance falls as $1/\beta^2$. The less dense band at the bottom of the plot corresponds to slow pions, since at any given momentum pions deposit less energy in the scintillator than protons. Thus protons can be distinguished from pions, and by setting a discriminator for each slab so as to exclude the lower region then slow pions can be excluded from the trigger.

2.4.3 The Fast Proton Trigger

A fast proton trigger is defined by a coincidence between 2 upstream scintillators, A1 (just in front of the 5m microstrips) and A2 (just after the 10m microstrips) as can be seen in Fig 2.2. These scintillators are square slabs of side 2.5cm and 5.0cm respectively. Immediately behind A2 is a similar scintillator except for being split into a left (A2L) and right (A2R) half so that the fast particle direction can be established.

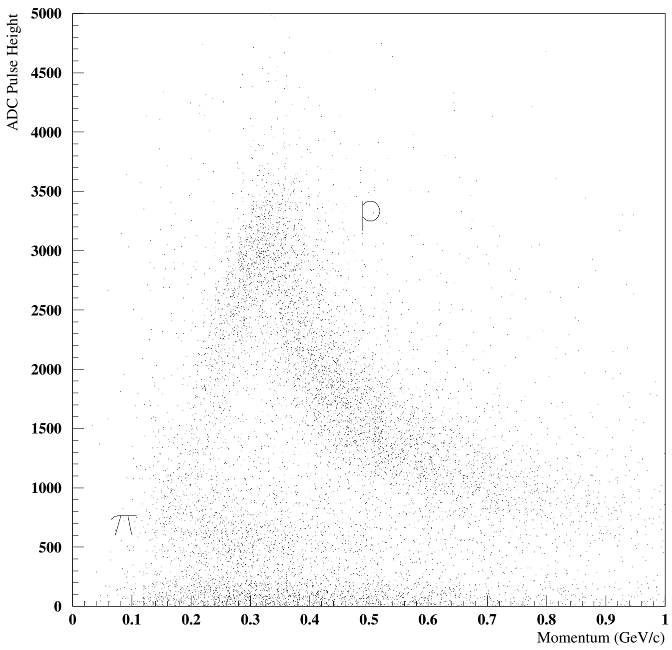

Figure 2.7: ADC pulse height vs slow particle momentum for SPCL.

2.4.4 The Neutral Trigger

OLGA is used to trigger on neutral particles. The photons from their decay lead to energy being deposited in several blocks of the lead glass array. For triggering purposes the lead glass blocks are split into 30 trigger cells each consisting of between 4 and 10 blocks. A neutral trigger is then defined as at least one trigger cell having more than 2 GeV deposited in it.

2.4.5 The Multiplicity Trigger

The trigger sections described above make up the LEVEL 1 trigger of WA91. This trigger is fast and can make a decision on taking an event within 236 ns of a beam proton hitting S2. It is fast because it relies only on information from scintillators and lead glass. It can and has been used to take events for analysis. However the efficiency of the trigger for taking good events can be improved by making checks on hit multiplicities in the MWPC's. This is the LEVEL2 trigger, and consists of two parts :-

- The C chamber multiplicity trigger - This is used to ensure that there is one and only one track going through the C chambers on the left or right side. This is done by requiring two modules to have 1 or 2 wires firing per plane.

- The FASTRO trigger - This is used to ensure a reasonable multiplicity in the A chambers. This is achieved by requiring 2 or more hits in chamber A3 outside of the beam region.

With the LEVEL 2 trigger incorporated, the decision time to take an event rises to 180μs, but this is still small compared to the data acquisition time ($\sim 800\mu$s) and the quality of events taken is improved.

The overall logic diagram for the WA91 trigger is shown in appendix A.

2.5 Event Types

Combining the trigger elements described above allows selection of DPE-like events while rejecting elastic ones (the main competing reaction), using the following criteria :-

- Only take event if there is a clean beam trigger.

- Allow events with a slow left and fast left proton (LL), or slow right and fast right proton (RR), as such events cannot be elastic as they would not balance momentum.

- If the event has slow left with fast right (LR), or slow right with fast left (RL) then check OLGA to see if it triggered on a neutral particle. If not, check FASTRO to see if there is reasonable forward multiplicity. If not then reject the event as it is likely to be an elastic.

For all triggers, the slow proton trigger also had the C chamber multiplicity check. In addition every 1 in 16 triggers taken was purely a beam trigger (BEAM). This was done in order to monitor the microstrip alignments throughout the run.

With this set-up, around 500 triggers were taken per burst (with an incident beam flux of about 5 million protons per burst), which is the amount predicted in the WA91 proposal [9]. The total number of triggers taken during the 43 days of data taking was 84 million, distributed amongst the different trigger types as recorded in Table 2.2.

Trigger	Amount (%)
LL	64.0
RR	6.6
LR + OLGA	8.8
RL + OLGA	4.0
LR + FASTRO	10.0
BEAM	6.6

Table 2.2: Proportion of each trigger type taken during 1992 run.

Chapter 3

Electromagnetic Calorimeters

3.1 Introduction

In the WA91 experiment, several important channels needing to be studied contain neutral particles, such as π^0, η, η'. The detection of such particles requires an electromagnetic calorimeter (which, as these particles decay deep inside the target, actually detects the photons due to their decay). Calorimeters also have several other advantages :-

- They are sensitive to charged particles as well.
- The dimensions needed to contain showers scales as ln(E), while a magnetic deflection device scales as $E^{\frac{1}{2}}$.
- They can be segmented, allowing precise measurement of incoming particle position, and also allowing the detector to be easily extended to cover larger solid angles if necessary.
- They do not need a magnetic field for energy measurements.
- They have fast response times of around 100ns which makes them useful for high rate measurements and for triggering purposes, either triggering on total energy deposition or patterns of energy deposition.

3.2 Electromagnetic Interactions

Particles traversing matter generally interact and lose a fraction of their energy. For electrons and photons the electromagnetic interaction dominates this energy loss. For electrons there are two main mechanisms responsible for energy loss [12, 13] :-

- Below about 100 MeV ionisation of the particles in the medium is the principal means of energy loss.
- Above 100 MeV the principal mechanism is bremsstrahlung. This is the process whereby electrons radiate photons as a result of the Coulomb interaction with the nuclear electric field. The emitted photons typically carry off a large fraction of the electron's initial energy. A primary electron with several GeV of energy may radiate thousands of photons on its way through the detector.

On the other hand, for photons [12, 13] :-

- Below 100 MeV the main mechanisms are Compton scattering, where the photon is scattered off an atom, or the photoelectric effect where a photon is absorbed by an atom and thus liberates an electron.
- Above 100 MeV the main mechanism is pair production. This involves the conversion of a photon into an electron-positron pair.

Positrons behave identically to electrons in their electromagnetic behaviour except that when one comes to rest it annihilates with an electron of the medium, creating two γ's of 511 keV energy.

Thus a high energy electron or photon can develop into an electromagnetic shower, with electrons radiating photons by bremsstrahlung which in turn create electron-positron pairs and so on. Similarly for a high energy incident photon. The shower may consist of thousands of particles - electrons, positrons and photons. The shower continues until the energy of the particles in it falls below about 100 MeV, when the dissipative processes of ionisation, excitation, Compton scattering and photoelectric effect take over. These processes do not increase the number of shower particles.

The energy-loss mechanisms depend primarily on the electron density of the medium in which the shower develops, which is roughly proportional to the (average) Z of the medium. The energy at which Compton scattering dominates pair production, and ionisation dominates bremsstrahlung are very material dependent. This leads to a definition of a "critical" energy, E_c, for the medium. Below this energy no shower particle multiplication occurs, as the dissipative processes have taken over. Thus complex dependence on the medium only occurs below the critical energy.

3.3 Shower Development

The mathematical description of a completely general shower is extremely complex. To simplify one considers only the average behaviour of the shower. Also, since at high energies the angle of emission of the electrons and photons is small, the shower will develop primarily in the forward direction. One can then treat the longitudinal and transverse development separately.

Since at high energies, where the shower development occurs, only the electron density of the medium determines the energy loss, the distance that the shower has traversed is usually described in a material independent way, by measuring it in radiation lengths, given approximately by [14]

$$X_{rad} = 180A/Z^2 \ g/cm^2$$

Shower calculations usually make a number of approximations [12]. A simple model which gives the correct qualitative description of the longitudinal development of a shower has been given by Heitler [15]. The following assumptions are made :-

1. Each electron with energy $E > E_c$ travels 1 radiation length before radiating a bremsstrahlung photon with half its energy.

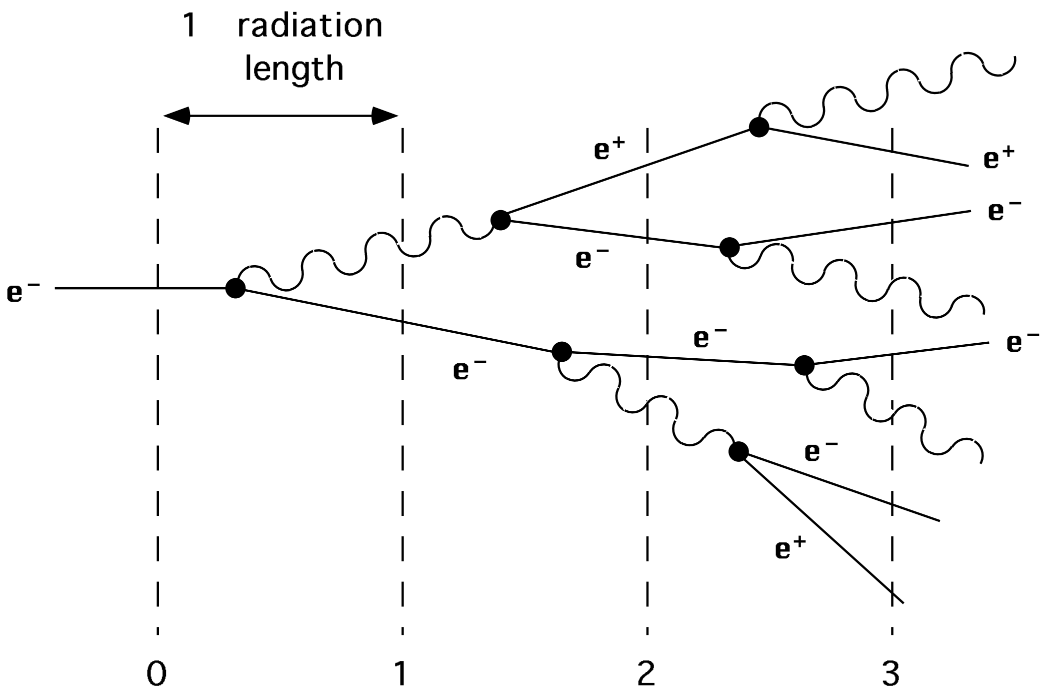

Figure 3.1: Simple model of the development of an electromagnetic shower. The numbers at the bottom are distances in radiation lengths.

2. Each photon with $E > E_c$ travels 1 radiation length before undergoing pair production, the electron and positron receiving half the photon's energy.

3. Electrons with $E < E_c$ stop radiating and lose their remaining energy by ionisation and excitation.

4. Neglect ionisation losses for $E > E_c$.

Fig 3.1 shows how a shower develops in this model. The shower begins with an incident electron of energy $E_0 >> E_c$. In the first radiation length it radiates a photon of energy $E_0/2$. In the second radiation length this photon produces an electron-positron pair of energy $E_0/4$, while the electron again radiates a photon. Thus after 2 radiation lengths there are 2 electrons, 1 positron and 1 photon, each of energy $E_0/4$.

This simple model predicts several important features of the shower :-

1. The total number of particles after t radiation lengths is

$$N(t) = 2^t = e^{tln2} \tag{3.1}$$

The number of shower particles thus increases exponentially with t.

2. The average energy of a shower particle at depth t is

$$E(t) = E_0/2^t \tag{3.2}$$

3. The shower has the maximum number of particles when $E(t) = E_c$, at the depth

$$t_{max} = \frac{ln(E_0/E_c)}{ln2} \tag{3.3}$$

At this the point the shower multiplication abruptly stops. This equation shows that the size of the detector needed to contain a shower scales as ln(E).

4. The number of particles at the maximum is

$$N_{max} = e^{t_{max} ln2} = E_0/E_c \tag{3.4}$$

5. The number of particles in the shower with energy greater than some value E' is $(E' << E_0)$

$$\begin{aligned} N(E > E') &= \int_0^{t(E')} N(t)\, dt \\ &\simeq \frac{1}{ln2}\frac{E_0}{E'} \end{aligned} \tag{3.5}$$

Thus the energy spectrum dN/dE' falls like $1/E'^2$.

6. The sum of all the track lengths of all charged particles in the shower is

$$\begin{aligned} L &= \frac{2}{3}\int_0^{t_{max}} N(t)\, dt \\ &\simeq \frac{E_0}{E_c} \end{aligned} \tag{3.6}$$

The factor 2/3 comes from the fact that the shower contains approximately equal numbers of e^-, e^+ and γ. Thus the total charged track length is directly proportional to the incident energy.

Beyond t_{max} no further multiplication occurs, and as more and more electrons are stopped, the total number of shower particles slowly decreases.

Since the underlying physics behind shower development is well understood, very accurate calculations for it can be performed by Monte Carlo simulation. These

Figure 3.2: Longitudinal shower profiles in lead at different incident electron energies. (D. Müller, Phys.Rev. D5:2677, 1972).

techniques can take into account energy dependences of the various loss mechanisms,dependence on the medium at lower energies, lateral spread due to multiple scattering, statistical fluctuations, and other complications. Such a program, EGS4 (Electron Gamma Shower) [16], is commonly used for this purpose. A study of OLGA using this program is under way. Fig 3.2 shows the results of a Monte Carlo calculation of the longitudinal shower development in lead. This figure shows the general features contained in equations 3.1 to 3.6, *viz* an initial exponential rise to a maximum followed by a slow tail off; a logarithmic dependence of t_{max} on E_0; and how N_{max} is proportional to E_0.

The transverse development of the shower is due to electrons moving away from the shower axis due to multiple scattering, and by bremsstrahlung photons being emitted at an angle to the axis. The transverse development is also measured in an nearly material independent way by measuring it in units of the Molière radius, given approximately by [14]

$$\rho_M = 7A/Z \ g/cm^2$$

where roughly 95% of the shower is contained laterally in a cylinder of radius $2\rho_M$.

3.4 Energy measurement

The OLGA calorimeter uses lead glass to convert incident electrons and photons into electromagnetic showers. The energy of the shower (and thus of the incident particle) is then measured using the Cerenkov effect [12]. This occurs when the velocity of a charged particle traversing a dielectric medium exceeds the velocity of light in that medium. Photons are emitted at a fixed angle to the particle, given by

$$cos\theta = 1/\beta n$$

where β is the velocity of the particle and n is the refractive index of the medium.

Calculations by Frank and Tamm [12, 17] give, in the wavelength interval 350-500 nm which corresponds to the response range of most photomultiplier tubes, an energy emitted per unit length by Cerenkov radiation of

$$dE/dx = 1180 \ sin^2\theta \ \ \mathrm{eV/cm}$$

and a photon yield of

$$dN/dx = 390 \ sin^2\theta \ \ \mathrm{photons/cm}$$

assuming 100% collection efficiency. From equation 3.6 the total charged track length is proportional to the incident energy. From the above equations the number of photons emitted per unit charged track length is constant (θ is nearly constant for all shower particles). Thus the number of Cerenkov photons emitted is proportional to the incident energy.

For an electron with $\beta \sim 1$ in lead glass, $\theta = 53.3^o$ so that 760 eV/cm is given off as Cerenkov radiation. This is small compared to the $\sim$ 2 MeV/cm ionization energy loss and approximately 100 times weaker than the light output in plastic scintillator. On average, 250 photons are emitted every centimetre of path length. It is therefore important to collect as many of these photons as possible.

Chapter 4

Calorimeter Testing and Calibration

4.1 Introduction

The calorimeter used in the 1986 WA76 run (the Geneva Photon Detector) would have been the ideal calorimeter to use in WA91, since it had been calibrated, the reconstruction program was written and working, and considerable experience had been accumulated in its use. However the liquid scintillator had degraded and the calorimeter was no longer usable. The best calorimeter available for use in 1991 was the OLGA lead glass calorimeter. This calorimeter had been used already in experiments such as WA4 at the OMEGA spectrometer [18] and NA14 [10]. However due to the length of time since its last use, the need for calibration data and the need to examine overall performance it was decided to use one of the CERN test beams to provide this information. This also gave the opportunity to test the data acquisition electronics and software before the first WA91 experimental run. A 30 day test run was performed in May 1991, the set-up and results of which are described in this chapter.

Beam momentum (GeV/c)	Δp/p
50	1%
25	1%
15	1%
10	1%
5	2%
3	10%
2	20%
1	30%

Table 4.1: Momentum bite of electron beam.

4.2 The test beam

The test beam used was the CERN X5 beam. This is a tertiary particle beam produced by the CERN-SPS and is capable of providing hadrons, electrons or muons of energies between 5 and 100 GeV. The beam is a part of the West Area test beam complex that is derived from the H3 secondary beam. The beam energy is tuned using dipole bending magnets and collimators. The last stage of the beam line consists of two correction dipole magnets for steering the beam and two quadrupole magnets for focussing. The momentum bite Δp/p at different electron energies is given in Table 4.1.

4.3 The apparatus

The layout of the apparatus is shown in Fig 4.1. This consisted of :-

- The A counter, consisting of 1 horizontal and 1 vertical scintillator slab (AH,AV) with an overlapping area of 5x5 cm^2.
- The B counter, consisting of 1 horizontal and 1 vertical scintillator slab (BH,BV) with an overlapping area of 2x2 cm^2.

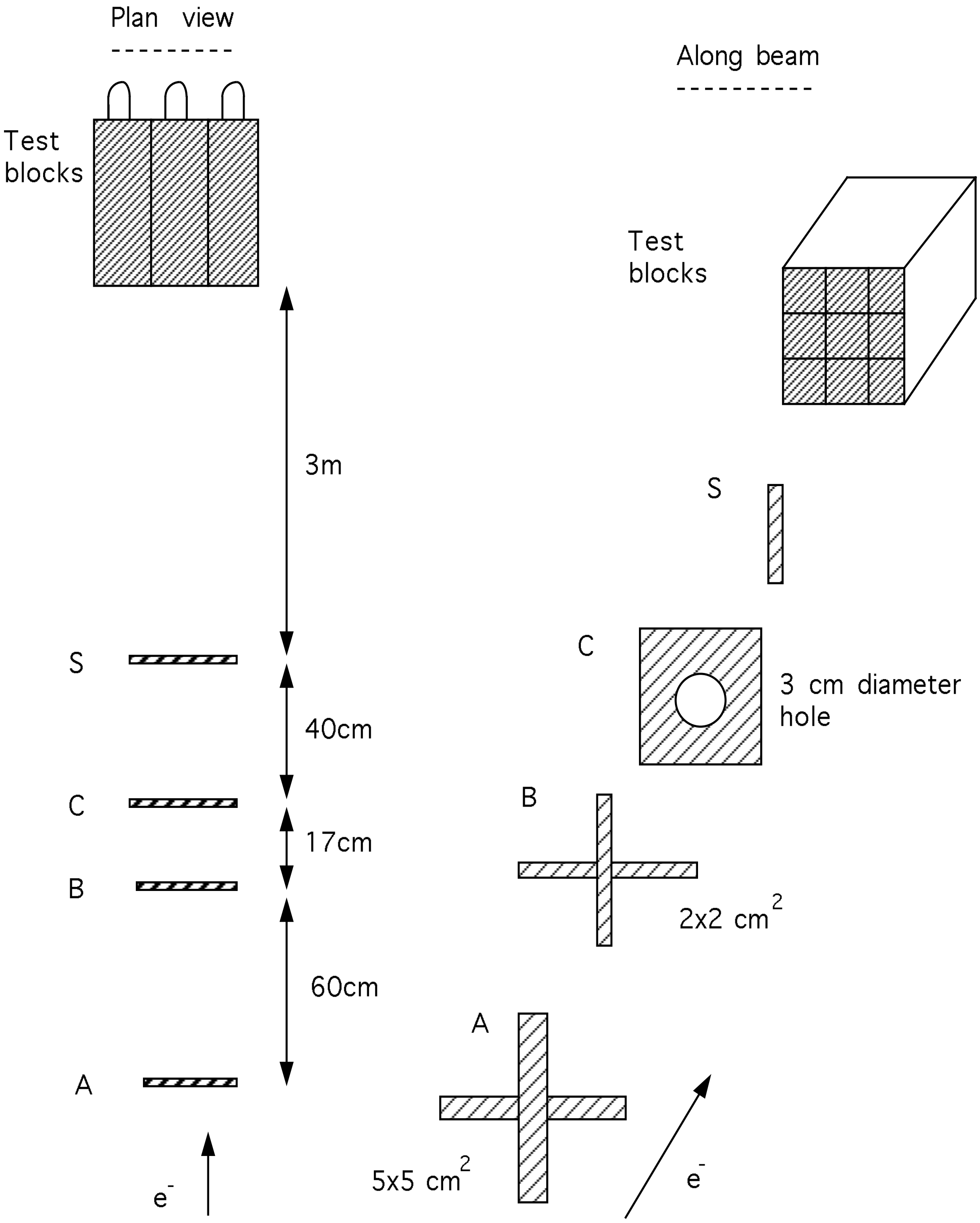

Figure 4.1: Layout of the test beam apparatus.

- The C counter, which is a large square scintillator slab with a 3 cm diameter hole to act as a veto.
- The S counter, which is a thin scintillator finger of dimensions 0.25x0.25 cm^2.
- The OLGA components being tested, about 3 m downstream of the C counter.

The trigger used to define a good beam particle was (AH.AV).(BH.BV).$\overline{\mathrm{C}}$.S . This ensured that the beam size at OLGA is around 2.5 mm. The beam counters were aligned by scanning the beam over them using the 2 bending dipole magnets. The beam rate using this trigger varied from about 100 events per burst at 50 GeV to about 3 events per burst at 1 GeV, this variation being due to the incident beam flux lowering as the beam energy was reduced.

4.4 Electronics

Fig 4.2 is a schematic diagram of the layout of the data acquisition electronics. The signals from the photomultipliers of the detector modules are passed to a FASTBUS ADC unit (LeCroy 1885) by 20 m long coaxial cables. The ADC has a resolution of 12 bits, plus the ability to switch automatically from low to high range mode, with a conversion factor of eight between modes. The high/low range offset for each ADC channel can be found using a calibration and trigger module (LeCroy 1810 CAT).

The ADCs are readout via FASTBUS by a Segment Manager/Interface module (LeCroy 1821 SM/I) which is capable of hardware pedestal subtraction. This means empty ADC channels are suppressed and thus the data associated with each event are reduced. The data from the SM/I are then read into a VME memory card (specially constructed by Heidelberg University) via an ECL convertor. This has a 132 Kbyte memory. Finally the data are read into a Fast Intelligent Controller (FIC 8232) called OMEGA4 which has a 1 Mbyte memory. OMEGA4 controls the readout of the SM/I via an I/O card, also specially constructed at Heidelberg University.

The sequence of actions involved in reading out an event is shown in Fig 4.3.

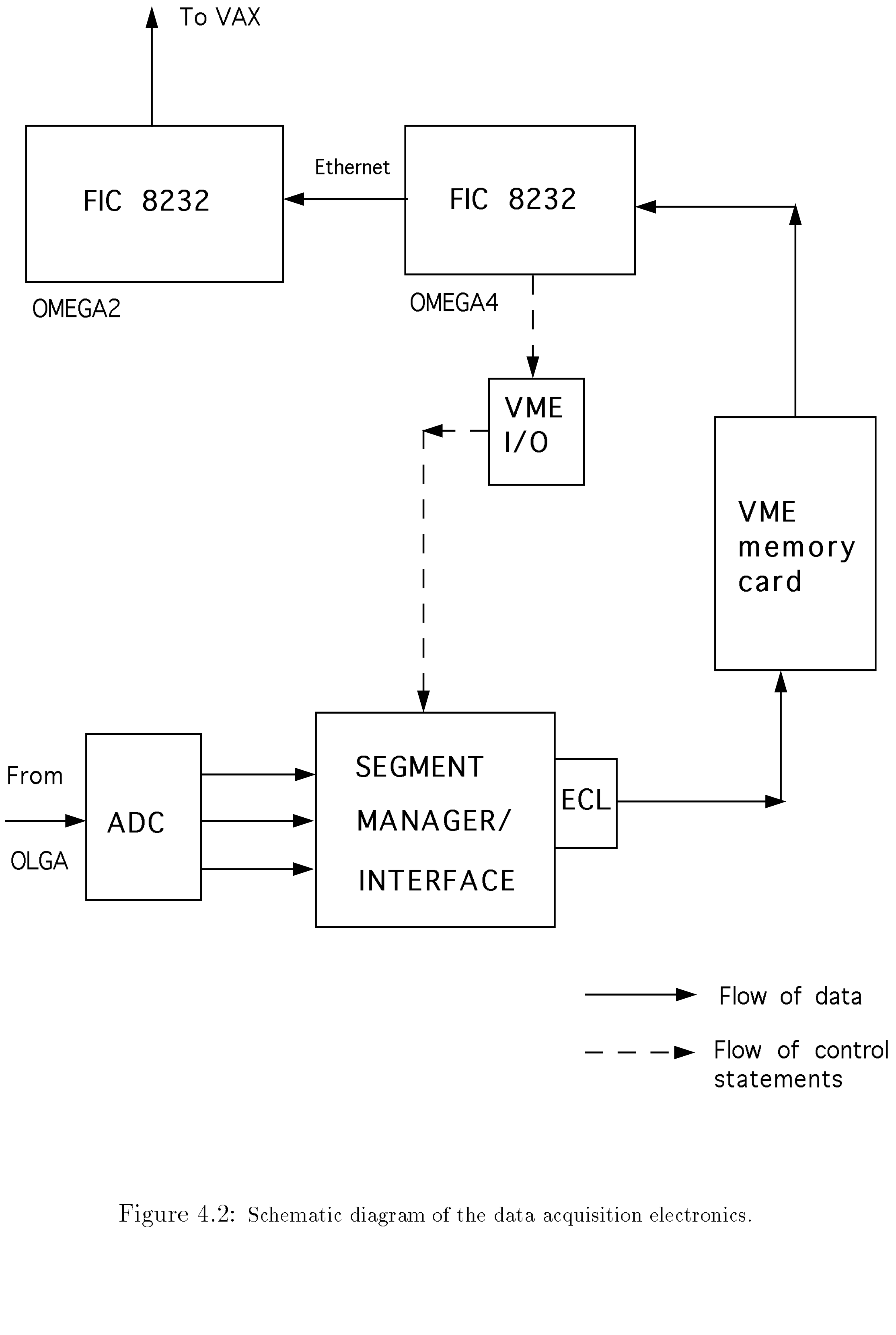

Figure 4.2: Schematic diagram of the data acquisition electronics.

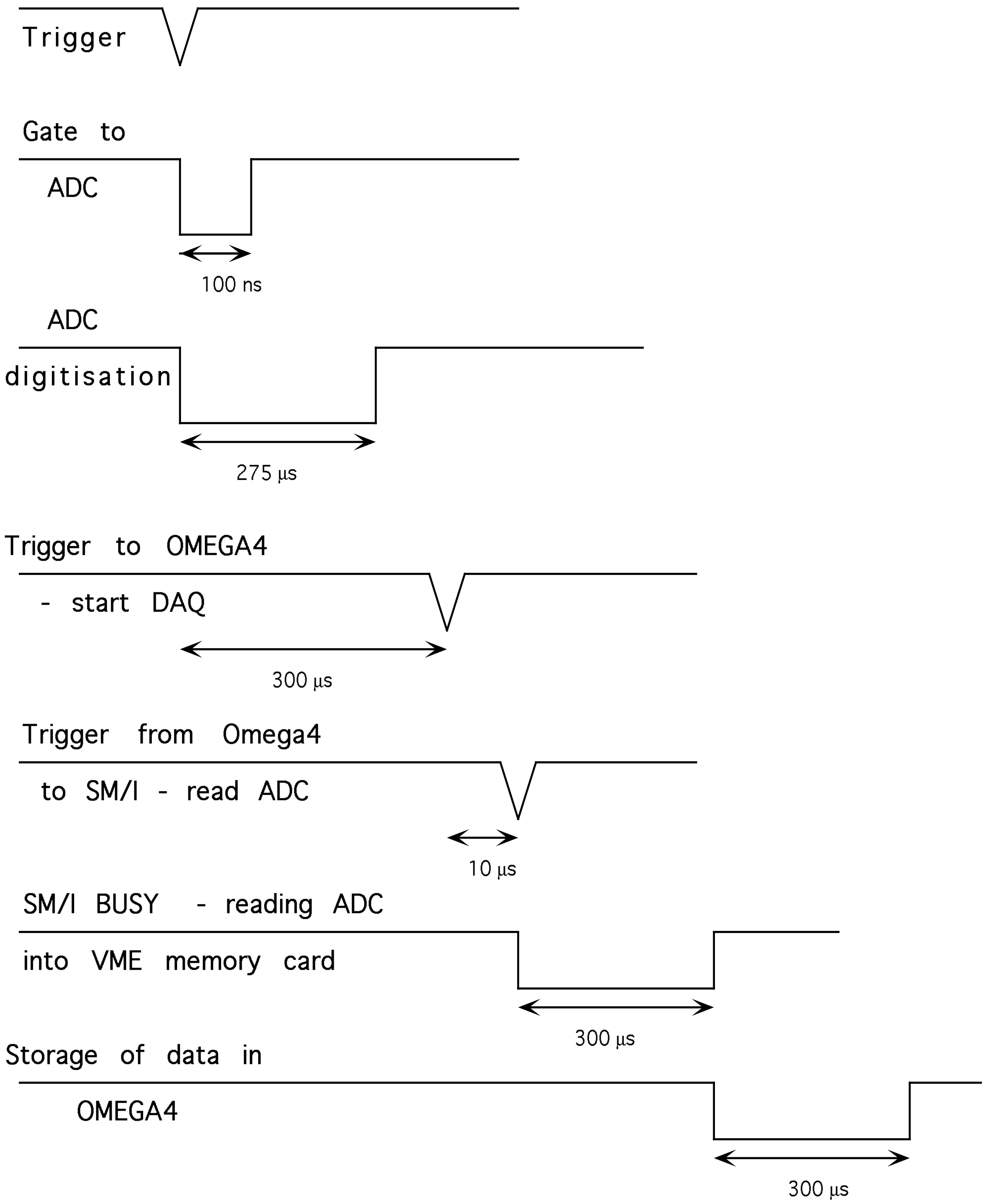

Figure 4.3: The sequence of actions involved in reading an event.

1. A trigger signal indicating a good beam particle is used to send a gate signal of 100ns width to the ADC. The conversion time of the ADC to digitise the input signals is 275μs.

2. 300μs after the initial trigger a signal is sent to OMEGA4 to instruct it to begin the data readout operation.

3. 10μs later OMEGA4 sends a signal via the VME I/O card to the SM/I to instruct it to read out the ADC. It takes 300μs for the data to be read out into the VME memory card.

4. Finally the data are read into OMEGA4. This takes a further 300μs. While this is happening, a clear is sent to the ADC's to clear them for the next event.

5. As the total read out time per event is 900μs a dead time of 1ms started by the initial beam trigger is imposed to avoid a further trigger coming in during readout.

Thus the data for each run are finally stored in the memory buffer of the FIC, OMEGA4. Each event consists of two 16 bit words. For a typical run of 500 events, 20 kbytes of memory are used. At the end of the run the data are transferred over Ethernet to another FIC called OMEGA2. This FIC is connected to the computer network over TELNET, and so the data for the run are finally transferred to the VAX in the form of a normal file. Unfortunately Ethernet is too slow for the data to be transferred directly from the ADC to OMEGA2, which is the reason for using OMEGA4 to store the data during the run.

4.5 Test run procedure

Before any test measurements could be made on the OLGA modules, it was necessary to locate the position of the beam and set up a coordinate system. The OLGA modules were mounted on a support platform which could be moved vertically using an hydraulic system and horizontally along rails using an electric motor. A fixed coordinate system was set up behind this platform using two rules of 1 metre length, and a horizontal and vertical pointer attached to the platform to allow coordinate measurement.

A system of 3x3 lead glass blocks was set up on the platform. These were moved using the platform so that the middle block was in the beam (i.e. only this block gave a signal on an oscilloscope). Then by scanning this block horizontally and vertically over the beam using the platform, and observing the ADC value for this block at each point, the positions of the block edges using the coordinate system were found. Thus as the dimensions of the block were known, the coordinate of the centre of the block was determined. The coordinates of the other blocks, and the sampler and fingers tested later, could then be measured relative to this point. The results of the test can be split up into those concerning the three major components of OLGA - the lead glass block array, the samplers and the scintillator fingers.

4.6 The Lead glass blocks

As described in chapter 2 these come in two types, an array of large blocks of size 14x14 cm^2, and a set of smaller 7x7 cm^2 blocks for the centre of the calorimeter. Twenty-five of the large blocks and all fifteen small blocks were tested. The first 9 large blocks were tested in a 3x3 array. The second set of 16 large blocks was tested in a 4x4 array. When the 15 small blocks had to be tested, these were set up in a 4x4 array and placed inside the larger block array by removing the middle two columns of large blocks.

4.6.1 Linearity of response

To test the voltage and energy dependence of the signals coming from the lead glass blocks, electrons of various energies were fired into the centre of each block (showers originating in the centre of a block are totally contained within it, as will be shown in section 4.6.2). Typical signal against PM voltage and signal against energy curves for the large blocks are shown in Fig 4.4. Similar curves are obtained for the small

Figure 4.4: a) typical gain curve and b) typical energy calibration curve of a large lead glass block.

blocks. As expected from section 3.4, the PM signal is directly proportional to the incident energy. This fact is used to calibrate the blocks, as it implies only the pulse heights for two energies need to be known in order to calibrate that block. Twenty-five of the blocks were calibrated using the electron beam. For the other blocks it was necessary to use a muon beam. This was provided by a muon halo around the π^- beam during the WA92 run, an experiment which also uses OLGA. Muons also lose energy by electromagnetic means, but compared to electrons the cross-sections for processes such as bremsstrahlung and pair production are smaller by a factor of $(m_\mu/m_e)^2 \approx 40000$, leading to a critical energy of around 200 GeV. Thus muons lose energy mainly through ionisation. NA14 found that the spectra for muons incident on a block have 2 peaks, one at 0.65 GeV and one at 1.1 GeV. The first peak corresponds to muons passing through the entire length of the block. The second peak corresponds to muons which also cross the light guide between the block and the PM tube, thus emitting Cerenkov light. This light is collected very efficiently as it is emitted so close to the PM, and seems to give a signal which would correspond to an extra 0.45 GeV being deposited in the block. Thus the muon halo gives two energy points per block, which allows their calibration. However it was found that this second point is not totally reliable, as it can vary between 1.0 and 1.3 GeV, and so for initial calibration the origin and the 0.65 GeV point were used. The calibration was then improved by methods described later.

The blocks calibrated during the test had their voltages set so that they all gave the same signal at each energy. The gain curve of Fig 4.4 was then used to set the other blocks in the same way in the 1992 WA91 run. This was done by comparing the muon signal in the test run calibrated blocks and the muon halo calibrated blocks, calculating by what percentage the second signal needs to be increased or decreased to coincide with the first, and then using the gain curve to calculate by how much the voltage on the PM tube needed to be altered to achieve this percentage signal change. This made online monitoring and offline analysis easier as the blocks had a common set of parameters.

4.6.2 Energy losses in the blocks

In order to examine the shower development in the blocks at various energies and to examine the amount of energy lost due to shower leakage between blocks, the beam was scanned horizontally and vertically between the centre of two blocks. Fig 4.5 shows how the average energy in a block varies as a function of distance for a vertical scan between the centre of two blocks at incident beam energies of 10 and 25 GeV. Similar curves are seen for a horizontal scan. These curves show that the shower is contained inside one block if it is initiated more than about 2.5 to 3 cm from the edge of the block; showers initiated closer than this to the edge of the block begin to spread between the two blocks. If for each event the energy in the two blocks is summed then Fig 4.6 is produced. This shows that about 3% of energy is lost for showers starting at or very near the gap between two blocks.

Figure 4.5: How the average shower energy in a block varies with distance for a) 25 GeV and b) 10 GeV incident electrons.

4.6.3 Energy resolution

Fig 4.7 shows a typical energy spectrum produced in a block by an incident electron. To obtain the energy resolution a Gaussian is superimposed onto the pulse height distribution, as shown by the solid curve, and the energy resolution is then given by the σ of this distribution divided by the mean pulse height. The energy dependence of the energy resolution can be expressed by the function

$$\sigma_E/E \ = \ a \ + \ b/\sqrt{E}$$

where the first term comes from factors such as incomplete shower containment, non-linearities in the energy response of the lead glass, fluctuations in PM tube response and so on, while the second term comes from the statistical nature of the showering process. Fig 4.8 shows the energy resolution as a function of beam energy for the large and small blocks. The dotted line is a fit to the above formula. Of the blocks tested the average values for the parameters were

$$a = 2.0\% \ \ , b = 6.0\% \qquad \text{for the large blocks}$$

Figure 4.6: Sum of shower energy as a function of distance for a) 25 GeV and b) 10 GeV incident electrons.

$$a = 1.0\% \ \ , b = 8.8\% \qquad \text{for the small blocks}$$

with a typical χ^2/NDF of 2.63/3. The variations of these parameters over the blocks measured came to 2% at the most.

4.6.4 Position resolution

The sharing of energy amongst blocks by the shower provides a method of determining the impact point of the particle to an accuracy better than the block size. There are several possible methods to do this; the simplest one is to use the energy measured in each block to calculate the barycentre of the shower, which is given by the sum over all blocks of the energy in the block multiplied by the position of its centre, divided by the sum of the block energies. Using the beam scans of section 4.6.2, a plot of shower barycentre against real beam position can be drawn. This is shown in Fig 4.9 The errors on each point give the width σ of the barycentre distribution. This curve can be used to calculate the real impact position of the particle from the barycentre of the shower. The error on the shower barycentre translates

Figure 4.7: Typical ADC pulse height spectrum for an incident electron. The solid curve is a Gaussian superimposed on the spectrum.

Figure 4.8: Energy resolution of a) large and b) small lead glass blocks. The dotted line is a fit described in the text.

Figure 4.9: Plot of shower barycentre against beam impact position for a) 25 GeV and b) 10 GeV incident electrons.

Energy	block edge	block centre
25 GeV	8.9 mm	41.0 mm
10 GeV	10.5 mm	48.5 mm

Table 4.2: Position resolution of the large blocks.

into the uncertainty in knowing the real impact position, i.e the position resolution. Table 4.2 gives the measured position resolution at the block centre and block edge for 10 and 25 GeV. These have been corrected for the finite beam width.

4.7 The Sampler

As described in chapter 2 the sampler is a convertor to start off the electromagnetic shower to improve the position resolution of the fingers. To ensure that the energy resolution of the detector does not suffer it is important to have good energy calibration, and also to allow for the attenuation of the Cerenkov light due to showers originating at different points along the sampler.

4.7.1 Energy deposited in sampler

To examine how much energy is deposited in the sampler by an incident electron, a sampler was placed in front of the array of lead glass blocks. To remove the possibility of any PM gain drift one of the blocks was recalibrated with beam energies from 1 GeV to 25 GeV (Fig 4.10a). The beam was then directed into the centre of this block with the sampler in front and the signals from both recorded as a function of beam energy. To remove events where the shower spreads into more than one block a cut was placed on the surrounding blocks at the usual level of block noise. If any of these surrounding blocks gave a signal above this threshold that event was ignored. Using the block calibration curve the average energy deposited in the block could be deduced. Since the beam energy is known the remainder of the energy could be assigned to the sampler. Fig 4.10b shows the average energy deposited in the sampler against incident energy, while Fig 4.10c shows this as the average percentage of incident energy deposited in the sampler. These results fit with the general shower description as can be seen by examining Fig 3.2. From this figure we see that for a constant radiation depth, as we have in the sampler, the energy deposited increases with E_0, but the amount of the increase tails off as the energy increases, leading to the form of curve in Fig 4.10b. Since as the energy goes down the sampler thickness approaches t_{max} the percentage energy deposited in the sampler increases with decreasing energy, as shown in Fig 4.10c. The shower process is statistical in nature, so there are large fluctuations around the average in the energy deposited in the sampler. Of incident electrons, 90% give a point inside the hatched area of Fig 4.10d. For example a 5 GeV e^- can deposit up to 40% of its energy in the sampler, falling to 15% for a 20 GeV e^-.

The 1 and 2 GeV beams were very "unclean", in the sense that there were a lot of very low energy electrons mixed in them. This was seen as a low energy peak in the sampler spectrum, corresponding to where these electrons were completely stopped in the sampler. To remove these, it was required that the signal in the block was above noise threshold and/or the sampler signal was above the low energy peak. This meant that electrons stopped in the sampler and not getting through to the

Figure 4.10: a) calibration curve of lead glass block. b) average energy deposited in sampler. c) average percentage of incident energy deposited in sampler. d) limits of incident energy deposited in sampler - 90% of e^- give a point in the shaded area.

Figure 4.11: Calibration curve for a sampler.

block behind would be ignored, but low energy sampler signals due to little shower development in the sampler would be accepted.

Using the ADC pulse height seen in the sampler together with the energy deposited in it as worked out above, it is possible to draw a calibration curve for the sampler. This is shown in Fig 4.11 The pulse height has been corrected for attenuation using the parameters found in the next section, and corresponds to the pulse height that would be seen if the electrons were incident at 0 cm. As for the blocks it is linear and goes through the origin. Unfortunately due to lack of time only one sampler was calibrated in this way. To calibrate the other samplers it is again necessary to use the muon halo technique described in section 4.6.1. However there will only be one muon energy point for the samplers, as no muons go through the light guide. From Fig 4.11 the muon signal (black circle) corresponds to 0.11 GeV deposited. This is consistent with the fact that the sampler is 3 radiation lengths in thickness, whereas for the blocks a muon deposits 0.65 GeV in 18.5 radiation lengths.

4.7.2 Attenuation in the sampler

To examine the attenuation of the Cerenkov signal along the length of the sampler, 10 and 25 GeV electron beams were directed at various points along it. The results are shown in Fig 4.12. The attenuation curve can be parameterised by

$$E(x) \;=\; E_0\, exp\, [a_1 x \;-\; a_2 x^2\,]$$

where $E(x)$ is the energy really deposited in the sampler, E_0 is the energy seen after attenuation, and x is the distance from the point of impact of the particle to the PM.

Fits to the data using the above equation are shown by the dotted curves in Fig 4.12. The values obtained for the constants are

$$\begin{aligned} a_1 &= 0.0090 cm^{-1} \\ a_2 &= 3.7 \times 10^{-5} cm^{-2} \end{aligned}$$

with a χ^2/NDF of 4.13/4. These values agree well with those obtained by NA14 [10]. This amount of attenuation gives with x=100 cm, for example

$$E_{real}/E_{seen} \;=\; 1.70\ .$$

4.8 The fingers

The fingers are designed to increase the positional resolution of the calorimeter to allow accurate measurement and separation of the 2 photons in π^0 and other neutral particle decays. It is thus necessary to know what is the expected pattern of signals in the fingers from showers initiated in the sampler. It was also necessary to test fingers of different types that were available to see which gave the best performance.

4.8.1 Attenuation in the fingers

The impact position is calculated from the barycentre of the horizontal and vertical finger signals. Attenuation of these signals thus leads to errors in this calculated

Figure 4.12: Attenuation curve for sampler at a) 25 GeV and b) 10 GeV. The dotted curves are fits described in the text.

position. The scintillator fingers on OLGA had already been tested with a radioactive source and divided into two classes. 'Good' fingers were defined as those with a ratio of (close end signal)/(far end signal) of less than 2.5. Of the remaining fingers, some were too bad to use (poor signal or too large attenuation) and so would have to be replaced, while the rest were modified by cutting off the ends, polishing and rewrapping. Two sorts of scintillator were under consideration for replacing the broken fingers, Nuclear Enterprises (NE) and Bicron, and fingers of both types were available for testing.

The fingers to be tested were laid horizontally, and a 25 GeV beam scanned in a vertical line over them in 0.5 cm steps. Plotting finger signal against beam position showed a peak, corresponding to the vertical centre of that finger. The beam was then centred vertically on a finger and scanned horizontally along it. This was done for 3 or 4 fingers of each type. Typical attenuation curves for each type are shown in Fig 4.13. The finger attenuation can be parameterised by a simple $e^{-\alpha x}$ dependence on the distance x from the PM tube. The value of α for each finger type is given in Table 4.3. Thus the modified fingers have improved greatly over the good ones, while both Bicron and NE are suitable for replacing the broken fingers.

Figure 4.13: Finger attenuation curves for a) good, b) modified, c) NE and d) bicron scintillator fingers. The dotted curves are fits described in the text.

Finger type	α	$\text{Signal}_{0cm}/\text{Signal}_{100cm}$
Good	0.0091	2.48
Modified	0.0030	1.35
NE	0.0032	1.38
Bicron	0.0024	1.27

Table 4.3: Attenuation parameters of the various finger types.

4.8.2 Finger responses

It is interesting to know how the fingers behave for showers of different energies, in terms of number of fingers going off, the number of times a cluster of fingers has one missing and so on. These tests were performed on the good fingers of the previous section. Initially it is necessary to normalise the finger signals. This was done using the beam scans described in the last section. Taking the data with the beam in a fixed horizontal position so attenuation could be ignored, only events with one finger firing were considered, where a finger was said to have fired if it gave a signal above a suitable noise cut. As the beam was centred on 3 different fingers, and the beam width meant that electrons hit the 2 adjacent ones about 22% of the time, this gave enough data to plot ADC spectra for 8 fingers. Using the mean ADC pulse heights, these 8 fingers could then be normalised relative to each other. In the WA91 run the fingers are normalised using muons.

A sampler was then placed in front of the fingers. This system was in front of the array of lead glass blocks. Electron beams of various energies were then directed into the sampler and fingers at 3 positions - near the finger PM tube, middle of finger, and far end of finger. To see the finger profiles clearly, events were only considered if the shower profile was centred on finger 4, i.e. if this finger had the maximum ADC pulse height. Also, to ensure the events were real, it was required that there should be a large amount of energy in the sampler and/or the lead glass blocks behind. This is especially important for the low energy beams as it will remove the spurious very low energy electrons coming in with the beam which are completely absorbed by the sampler. Fig 4.14 shows the percentage of fingers going off in an event as

Energy (GeV)	1 finger missing (%)	2 fingers missing (%)
25	17.5	2.6
10	18.6	2.5
5	15.1	9.4
3	8.3	6.9
2	12.5	4.6
1	21.4	4.8

Table 4.4: Number of missing fingers in a cluster as a function of energy.

a function of energy, for electrons incident in the middle of the system. Thus the most likely number of fingers in a cluster at 25 GeV is six, while this falls to one at 1 GeV. The average number of fingers going off is plotted in Fig 4.15. The reason for the average number at any energy decreasing with distance from the PM is that due to attenuation, the small signals at either end of a finger cluster may fall below the noise cut.

Scanning through the events allows them to be separated into four categories. Good events (Fig 4.16a) are those with an expected normal distribution in the finger pulse heights in a cluster. Bad events (Fig 4.16b) are those with spikes occurring on an otherwise normal finger profile. Finally there are events which have a normal profile, but one (Fig 4.16c) or two (Fig 4.16d) of the fingers in the cluster give no signal, the reason for which is not known. Considering all positions and energies, about 70% of events are good, 10% are bad, 15% have 1 missing finger and 5% have 2 missing fingers. The breakdown with energy (all positions) is given in Table 4.4. The table shows that if there is any dependence on energy, it is a very weak one.

4.9 Calibration of OLGA

In order to obtain the best energy and position resolution it is necessary to calibrate the blocks, samplers and fingers as accurately as possible. The initial calibration was performed using muons coming from the muon halo surrounding the π^- beam

Figure 4.14: Percentage of fingers going off as a function of energy.

Figure 4.15: Average number of fingers going off against energy at a) near end, b) middle and c) far end of finger.

Figure 4.16: Examples of a) good, b) bad, c) one finger missing and d) two finger missing events.

in the WA92 experiment. As stated in section 4.6.1 muons passing through the lead glass blocks give rise to two signals, one of 0.65 GeV corresponding to the minimum ionising energy loss for the muons in the block, and one of ~ 1.1 GeV corresponding to muons also passing through the light guide to the photomultiplier. A typical ADC spectrum for muons passing through a lead glass block is shown in Fig 4.17a, where the two peaks can clearly be seen. Since the energy corresponding to the second peak fluctuated around 1.1 GeV (as found from the test beam calibrated blocks) it was decided to use the 0.65 GeV point and the origin to fix the initial calibrations for each block. For blocks where the muon halo is not incident, charged tracks coming from WA92 π^-p interactions and traced to OLGA were used.

The same technique was used to initially calibrate the samplers, where as stated in section 4.7.1 only the minimum ionising peak at 0.11 GeV is seen. Fig 4.17b shows a typical ADC spectrum for muons passing through a sampler, where each muon signal has been corrected for attenuation in the sampler using the parameters found in section 4.7.2.

Muons passing through the fingers were also used to normalise the finger signals relative to each other.

The calibration of the blocks and sampler is then improved using π^0's. Events coming from the $\pi^+\pi^-\gamma\gamma$ channel are selected, where each γ deposits its energy in a single block only. The following steps are then followed :-

1. The sampler calibrations are assumed to be correct. Then a block is chosen and the $\gamma\gamma$ mass spectrum is plotted using all the surrounding blocks. The calibration constant of the chosen block is then altered until the π^0 peak is centred at the correct mass. This is repeated for all the blocks.

2. The block calibrations are now assumed to be correct. A sampler is chosen and the $\gamma\gamma$ mass spectrum plotted using all the surrounding blocks/samplers. The calibration constant of the chosen sampler is then altered until the π^0 peak is centred at the correct mass. This is repeated for all the samplers.

Steps 1 and 2 are then repeated until the calibration constant of each block does not

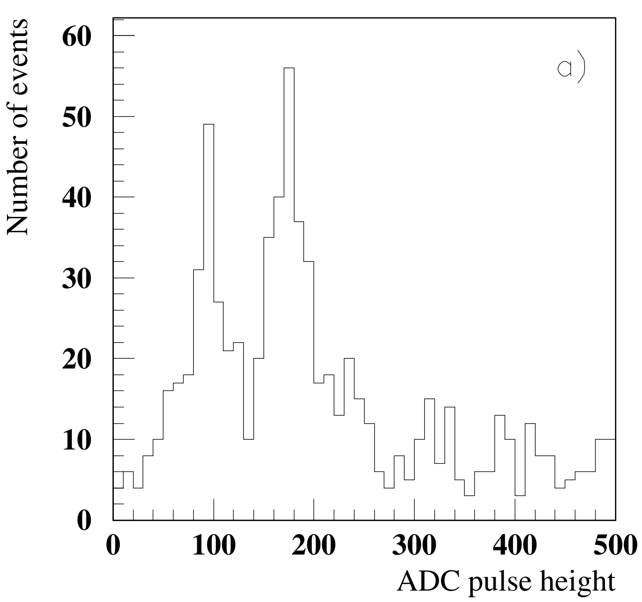

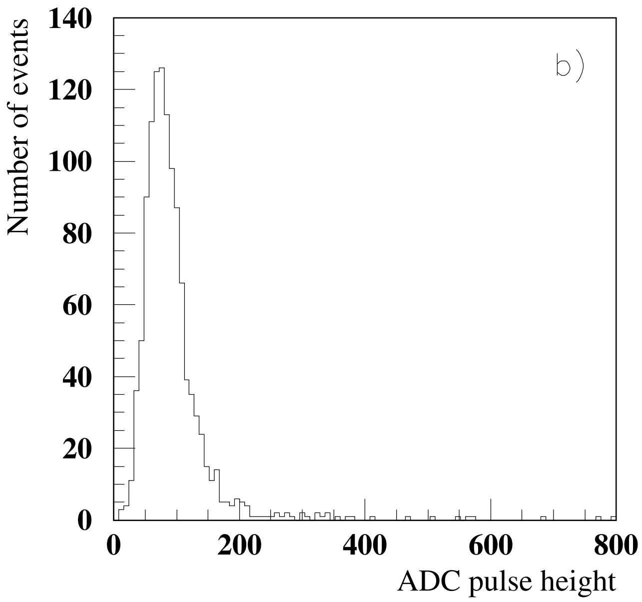

Figure 4.17: Typical ADC spectra for incident muons for a) a lead glass block and b) a sampler.

change by more than 0.5% between iterations. The blocks are chosen to indicate stability rather than the samplers because it is found that the block calibrations are more important to the overall π^0 mass spectrum than the sampler calibrations.

The $\gamma\gamma$ mass spectrum from the $\pi^+\pi^-\gamma\gamma$ channel (no momentum balance cuts applied) using the whole calorimeter was fitted for the muon calibration alone and gave the following parameters for the π^0 and η

$$
\begin{aligned}
m_{\pi^0} &= 123.6 \ \pm \ 0.7 \ MeV \\
\sigma_{\pi^0} &= 18 \ \pm \ 1 \ MeV \\
m_{\eta} &= 519 \ \pm \ 4 \ MeV \\
\sigma_{\eta} &= 44 \ \pm \ 4 \ MeV
\end{aligned}
$$

while after the recalibration using π^0's

$$
\begin{aligned}
m_{\pi^0} &= 135.5 \ \pm \ 0.5 \ MeV \\
\sigma_{\pi^0} &= 17.1 \ \pm \ 0.6 \ MeV \\
m_{\eta} &= 561 \ \pm \ 4 \ MeV \\
\sigma_{\eta} &= 41 \ \pm \ 4 \ MeV
\end{aligned}
$$

indicating a significant improvement in the overall calorimeter calibration.

Chapter 5

Background Reduction in Channels involving Photons

5.1 Introduction

As explained in appendix C, the electromagnetic calorimeter reconstructs photon impacts using the signals recorded in the blocks, samplers and fingers. However not all of these signals are due to real photon impacts. For example noise in the PM tubes, or light leaks in the lead glass can lead to fake photons being recorded. Also charged tracks incident on the calorimeter give rise to electromagnetic showers which can be mistaken for photons. All such processes will lead to backgrounds being introduced into the data, making it harder to identify possible resonances in the various channels. It is thus essential to identify the sources of background, and to reduce them while retaining as much of the real signal as possible. This chapter describes the three main sources of background found in WA91, and how they were reduced. Although this chapter concentrates on the $\pi^+\pi^-\gamma\gamma$ channel the principles can be applied to all channels involving photons.

Distance from centre of OLGA (cm)	Itype	y_{diff} (cm)	z_{diff} (cm)
R > 20	10 - 20	14	12
	40 - 50	26	26
R ≤ 20	10 - 20	20	20
	40 - 50	27	27

Table 5.1: Limits on the difference in y and z between a charged track and OLGA cluster for an association to be made.

5.2 Removal of charged track impacts

A serious source of background is from clusters caused by impacts of the charged tracks on OLGA, which can turn 2γ events into events with 3,4,5 etc. γ's. These impacts have to be removed. This is done by tracing each track from its last measured position to OLGA, using its reconstructed energy and momentum. For tracks whose last measured position is outside the magnetic field a straight line extrapolation is used, while for those with a last measured point inside the field, the track is extrapolated to the edge of the field (whose strength and direction has been measured at regular intervals) using a fourth order Runge-Kutta method, and then the straight line extrapolation is used. For each traced track, the difference in y and z between its impact and each cluster in OLGA is computed. The cluster is marked as associated with a charged track if y_{diff} and z_{diff} are within the limits shown in table 5.1. The explanation of the photon type Itype as used in this thesis is given in appendix C. Wider association cuts are used if the OLGA cluster is part of a subcluster, as the coordinates of such clusters are more open to error. It was also found that due to the missing block in OLGA, and due to the 'shadow' of the microstrips that wider cuts are needed for the central region of the calorimeter. Typical distributions of y_{diff} and z_{diff} are shown in Fig 5.1. Clusters that are thus associated with charged tracks are then rejected.

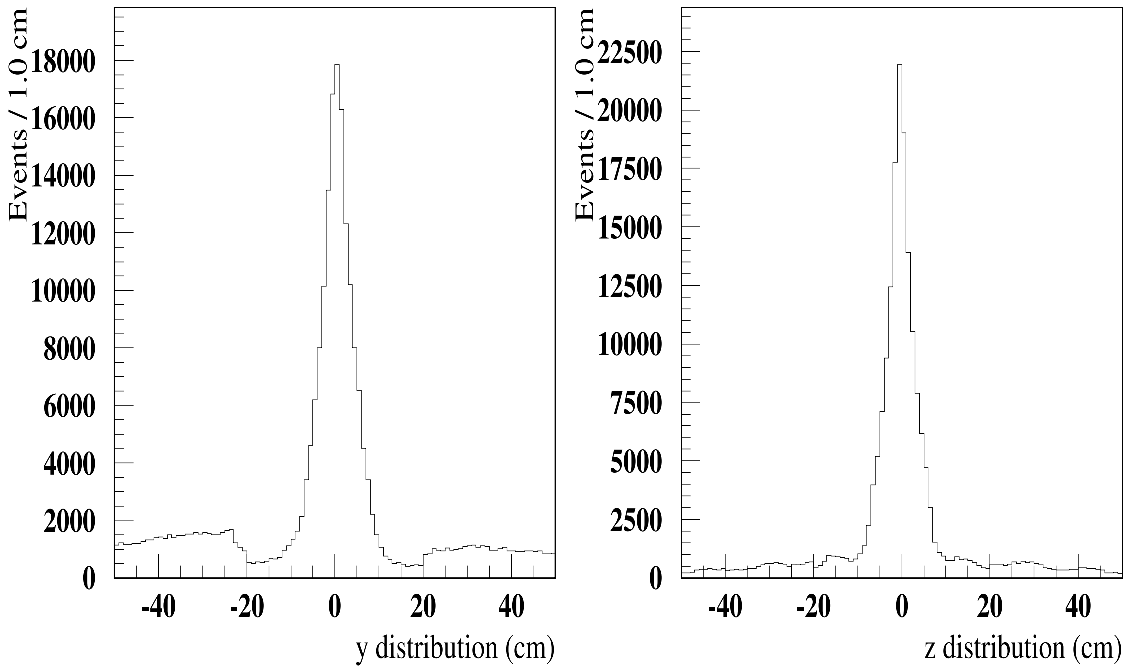

Figure 5.1: Distributions in y and z for (charged track hit) -(OLGA cluster position).

5.3 Removal of other channels

If, in the reaction, $pp \rightarrow p_f(\pi^+\pi^-2\gamma)p_s$ the missing transverse momentum p_t of the $\pi^+\pi^-$ system is plotted (i.e. ignoring the γ's) then a clear peak is seen at $p_t = 0$, as shown in Fig 5.2. The explanation for this is that mixed into the real $\pi^+\pi^-2\gamma$ events are $\pi^+\pi^-$ events with 2 fake γ's. This happens because of the gate width on the blocks of OLGA. In order for the ADC's to read the voltage signal from the PM tubes, a logic gate signal must be sent in coincidence with the PM signal. A gate width of 250ns was needed to read out the voltage signal from the lead glass blocks as these signals were quite wide. The beam rate was 2MHz and so the interaction rate with a 15% target was about 300kHz. Thus with a 250ns gate on the OLGA blocks the chance of another interaction occurring whilst reading the signals from the blocks is about 1 in 10. This has the effect of turning a $\pi^+\pi^-$ event into a $\pi^+\pi^-n\gamma$ event, where $n \geq 1$. Now since the gate on the fingers was only 70ns, the chances of pile-up occurring in the fingers is much less, so it would be expected that these fake γ's would have no finger information, i.e. be ORC type 18 or 20. This is indeed the case as can be seen in Fig 5.3, which is a plot of γ type against γ energy for photons in the $\pi^+\pi^-$ missing p_t peak. If the γ energy is plotted against missing p_t (see Fig 5.4) for the $\pi^+\pi^-$ system, then the peak at low p_t (out of time

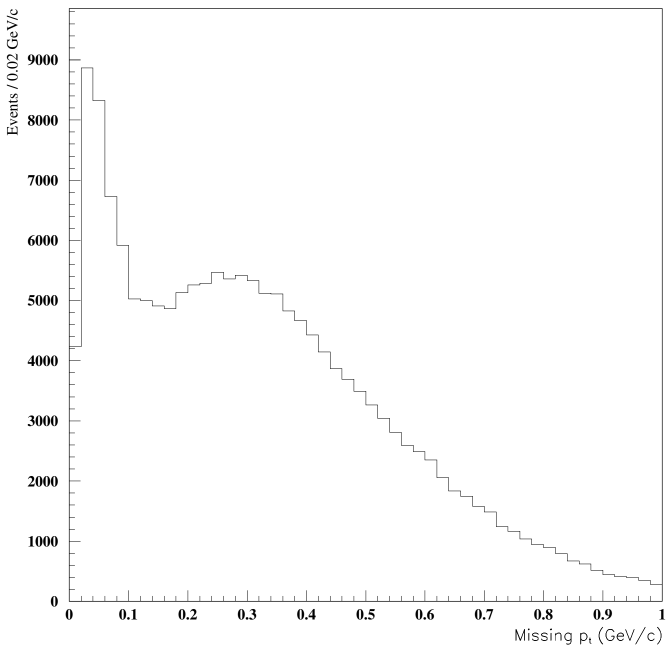

Figure 5.2: Missing transverse momentum of the $\pi^+\pi^-$ system from the $\pi^+\pi^-2\gamma$ channel.

γ's) corresponds to low energy γ's, with E < 1.5 GeV. Unfortunately most of the real $\pi^+\pi^-\gamma\gamma$ signal at high p_t also corresponds to low energy γ's. Thus it is difficult to remove the out of time events with merely an energy cut. The easiest way to remove these events with fake photons is to cut on the missing momentum of the $\pi^+\pi^-$ system, the optimum cuts being

$$\begin{aligned} |\text{missing } p_x| &< 10.0 \text{ GeV/c} \\ |\text{missing } p_y| &< 0.10 \text{ GeV/c} \\ |\text{missing } p_z| &< 0.06 \text{ GeV/c} \end{aligned}$$

Fig 5.5a shows the mass spectrum for these rejected events if the γ's are ignored. This is of the same shape as the normal $\pi^+\pi^-$ mass spectrum, indicating the interpretation of their origin is correct. Alternatively if we treat these rejected events as real $\pi^+\pi^-\gamma\gamma$ events and plot the $\gamma\gamma$ mass spectrum (Fig 5.5b) we see there is very little π^0 or η signal, and indeed the $\pi^+\pi^-\pi^0$ and $\eta\pi^+\pi^-$ mass spectra (Fig 5.5c,d) for these events show very little structure.

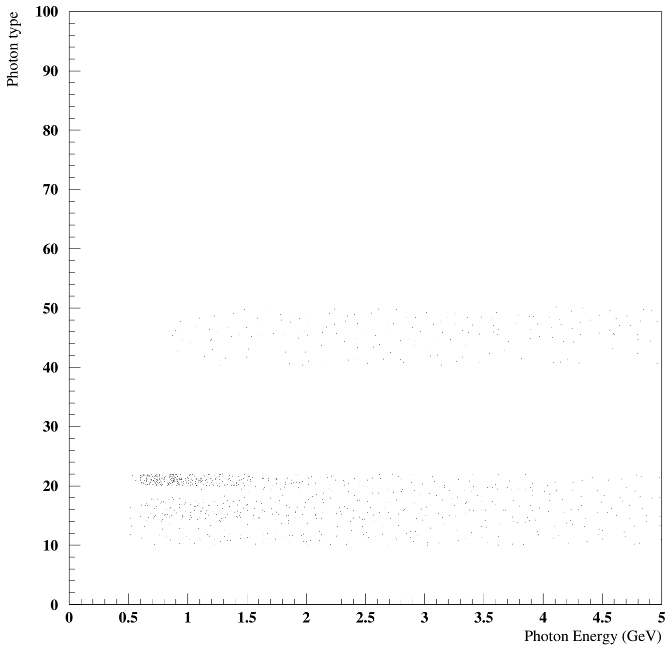

Figure 5.3: ORC γ type vs γ energy for the fake photons.

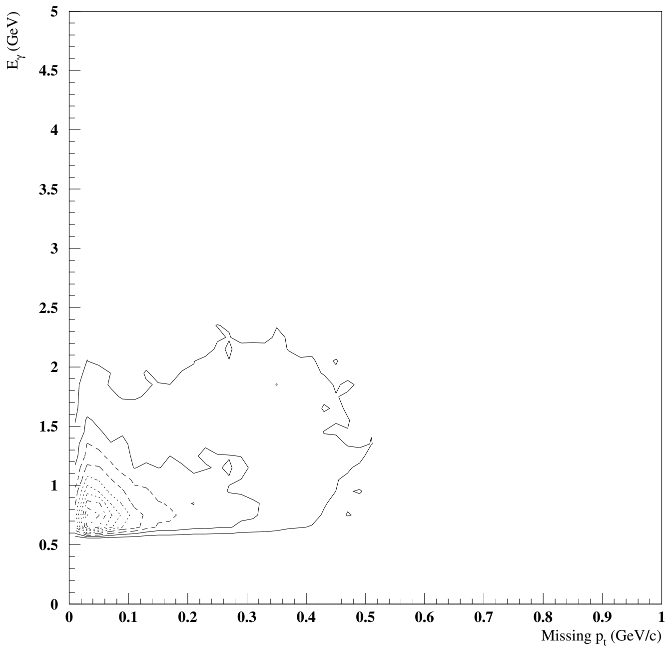

Figure 5.4: γ energy against missing p_t for the $\pi^+\pi^-$ system from $\pi^+\pi^-\gamma\gamma$.

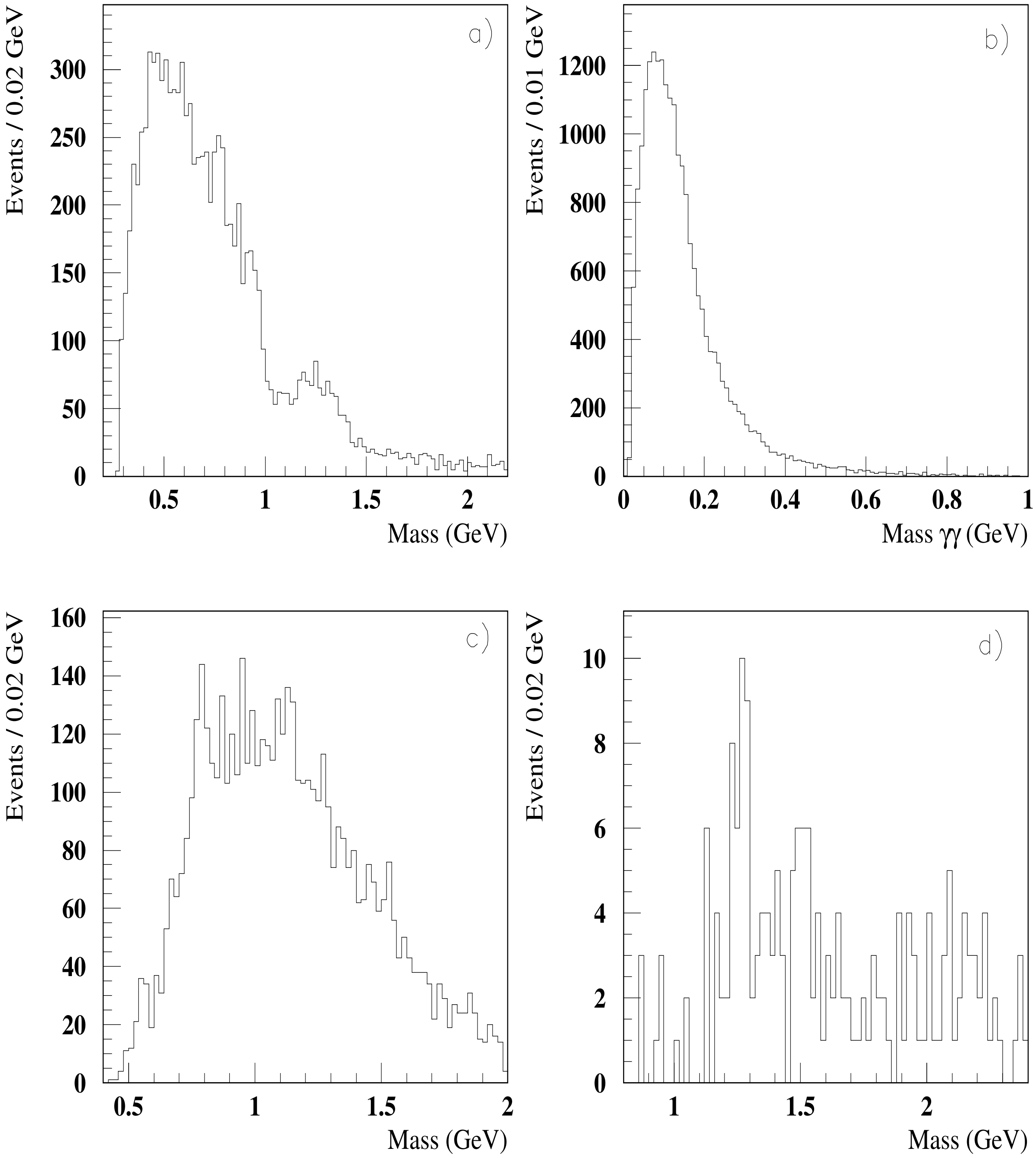

Figure 5.5: a) $\pi^+\pi^-$ mass spectrum for rejected events. b) $\gamma\gamma$ mass spectrum for rejected events. c) $\pi^+\pi^-\pi^0$ and d) $\eta\pi^+\pi^-$ mass spectra for rejected events.

5.4 Removal of γ's due to noise

The final cleaning of the photon signals from OLGA is achieved by removing signals due to noise (e.g. from light leaks in the PM tube light guides). This is achieved by examining the $\gamma\gamma$ mass spectrum and trying to reduce the background. This can be done in two ways :-

1. Energy cuts - Fig 5.6 shows the minimum energy of the $\gamma\gamma$ pair (E_{min}) against the mass of the $\gamma\gamma$ pair ($m_{\gamma\gamma}$) for the $\pi^+\pi^-\gamma\gamma$ system (with the above cuts applied). This is shown for events with at least one ORC type 10 (fingers in both y and z), type 14 (fingers in either y or z) and type 20 (no finger information) photon. Clear bands at the π^0 mass can be seen in all the plots. The amount of background around the π^0 mass varies with photon type, for example the π^0 signal is clear in the type 10 photons for all energies, whereas in the type 20 the signal only comes out of the background for E_{min} greater than about 1 GeV. By using these plots and the resulting $\gamma\gamma$ mass spectra the optimum energy cut to remove background for each photon type can be chosen. This is shown in Fig 5.7 where the $\gamma\gamma$ mass spectrum for events with a type 20 photon is shown with no energy cut, and with a cut of 1.4 GeV. A similar procedure can be used with the η signal (see Fig 5.6d). Higher energy cuts are required for photon types with less finger information since it is more likely for such photons to be due to noise than it is for a photon which also has y and z finger hits associated with it.

2. Radial cuts - If the distance from the centre of OLGA (R_{centre}) is plotted against the $\gamma\gamma$ mass (Fig 5.8) then again a band can be seen at the π^0 mass. The background can be reduced if a cut is made on R_{centre}, the background being due to the missing block in the centre of OLGA and the presence of the 5m microstrips. Once again a similar procedure can be used for the η signal.

The actual cuts on E_{min} and R_{centre} used are given in chapters 6 and 7.

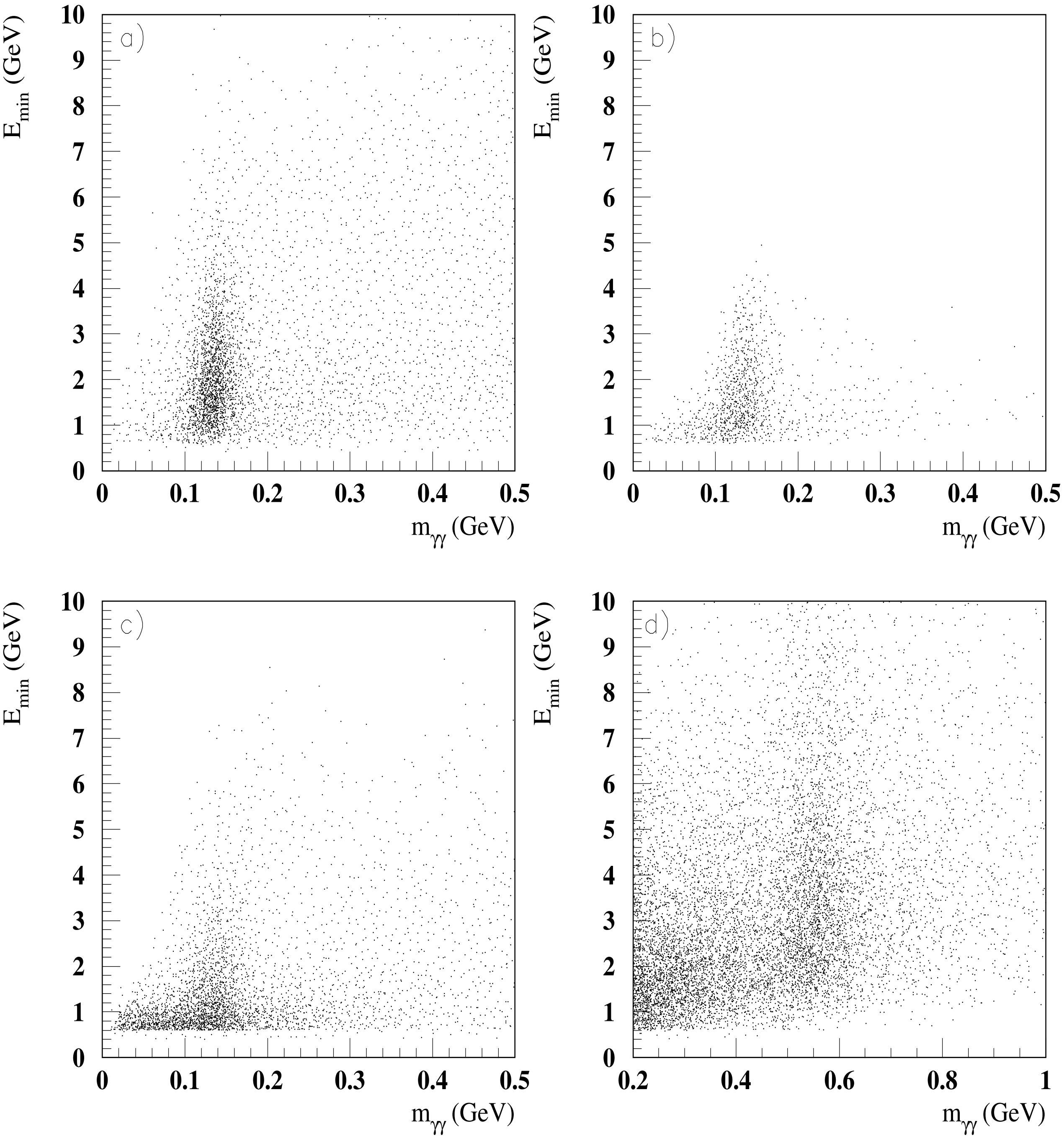

Figure 5.6: E_{min} vs $m_{\gamma\gamma}$ for the $\pi^+\pi^-\gamma\gamma$ system for events with a) type 10, b) type 14, c) type 20 and d) type 10 (in η mass range) photon.

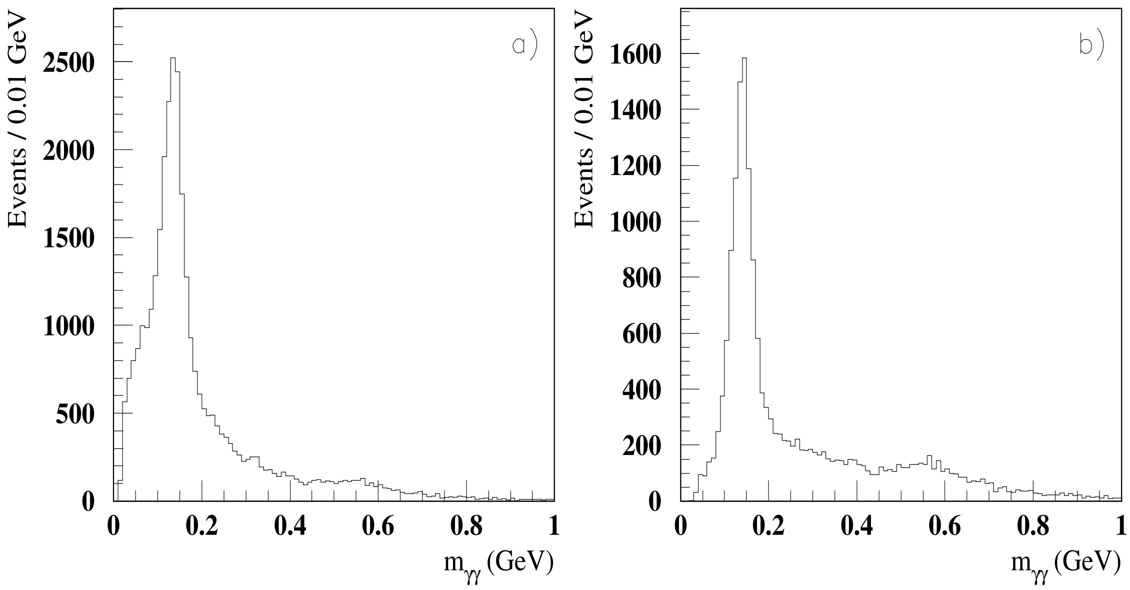

Figure 5.7: $\gamma\gamma$ mass spectra for events with a type 20 photon with a) no energy cut and b) a 1.4 GeV energy cut.

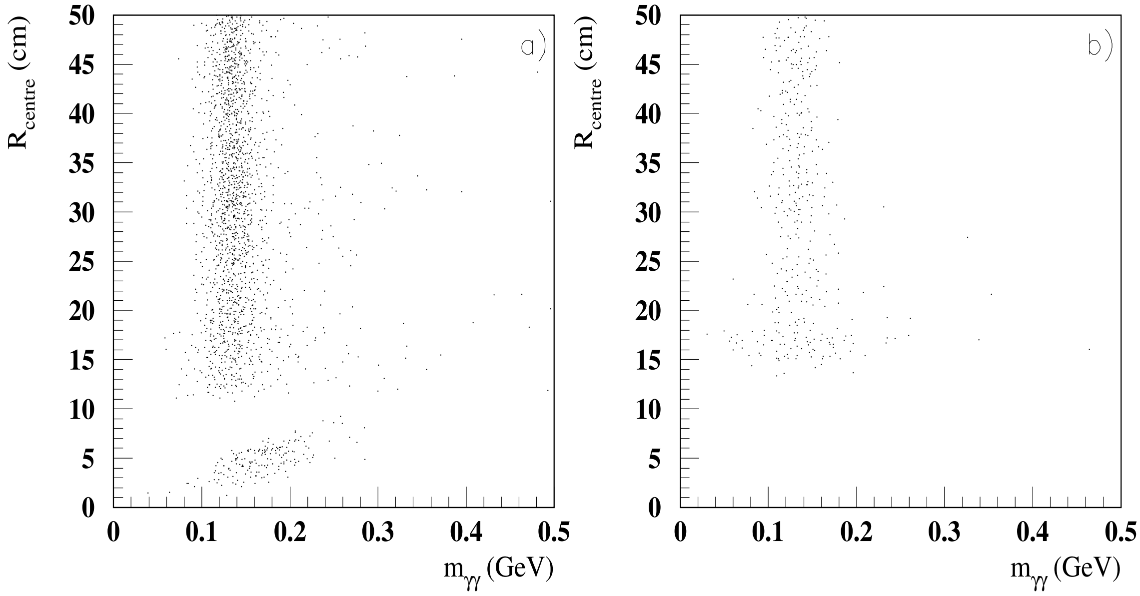

Figure 5.8: R_{centre} vs $m_{\gamma\gamma}$ for events with a) type 10 and b) type 14 photons.

Chapter 6

The $\eta\pi^+\pi^-$ channel in WA91

6.1 Introduction

The search for mesonic resonances in the mass range 1.0 to 2.0 GeV has been extensively conducted over the past years in channels such as $K\overline{K}\pi$, $\eta\pi\pi$, 4π and $\rho\gamma$. Several resonances have been seen in this region in various production processes, but the situation is unclear with many of these states awaiting confirmation of their existence and parameters.

The $\eta\pi\pi$ channel is an interesting one to study to help clarify the situation, especially in the 1.4 GeV region, where confusing observations of $J^{PC} = 0^{-+}$ and 1^{++} states have been made for the past 27 years, in reactions such as $p\overline{p}$ annihilation [19], radiative J/ψ decay [20, 21], $\pi^- p$ interactions [22] and central production [24]. These states have similar masses and widths, different reaction mechanisms but all decay to $K\overline{K}\pi$. Recent experiments and reanalysis of old data have now come to the conclusion there are in fact three states in this region, one at 1400 MeV decaying to $\delta/a_0(980)\pi$ [25, 26] with $J^{PC} = 0^{-+}$, one at 1420 MeV decaying to $K^*\overline{K}$ [24, 27] with $J^{PC} = 1^{++}$ and one at 1490 MeV decaying to $K^*\overline{K}$ [26] with $J^{PC} = 0^{-+}$.

The 1400 MeV state is most likely a radial excitation of the ground state pseudoscalar multiplet. The $\delta/a_0(980)\pi$ decay mode implies it should be seen in the $\eta\pi\pi$ channel which has been confirmed [25, 28], but probably not in central production where pseudoscalar state production seems to be suppressed relative to other states, and indeed it was not seen in the 300 GeV/c WA76 data [29].

The dominant $K^*\overline{K}$ decay mode of the 1^{++} state, called the $E/f_1(1420)$, indicates a strong $s\overline{s}$ component to its wavefunction. However it is not formed in K^- incident experiments where $s\overline{s}$ objects should be preferentially produced. Instead a different 1^{++} state is observed, the $f_1(1510)$ [30], which is now thought to be a better candidate to complete the ground state 1^{++} nonet. This leaves the $E/f_1(1420)$ as an extra possibly exotic state, which could be a hybrid [31], a four quark state [32] or a $K^*\overline{K}$ molecule [33]. The 1490 MeV state could also be a $K^*\overline{K}$ molecule in P-wave. Searching for a $\eta\pi\pi$ decay mode of these mesons will help in deciding on their structure.

A state has been observed in the 4π channel of the 300 GeV/c WA76 and 450 GeV/c WA91 data in the 1900 MeV region, called the X(1900)[34, 35]. A spin analysis of this state has revealed it is a 2^{++} state which is either a single resonance decaying equally to $a_2(1320)\pi$ and $f_2(1270)\pi\pi$ or two separate resonances. A study of the $\eta\pi\pi$ channel, where only the $a_2(1320)\pi$ mode would be present, should help confirm the nature of this state.

Thus the $\eta\pi\pi$ decay channel can give vital evidence on the nature of several states which are as yet not fully understood. The following chapter describes the analysis of the $\eta\pi\pi$ channel formed in the experiment WA91 at 450 GeV/c.

6.2 Selection of the channel $\eta\pi^+\pi^-$

6.2.1 Selection of $\eta \to \gamma\gamma$

The reaction

$$pp \to p_f(\pi^+\pi^-\eta_{\to\gamma\gamma})p_s \tag{6.1}$$

where the symbols f and s refer to the fast and slow proton respectively in the laboratory frame, has been selected from the sample of events having four outgoing tracks and two reconstructed γ's in the electromagnetic calorimeter OLGA. Initially an energy cut of 1 GeV was imposed on the γ's, and showers associated with charged tracks were removed as described in the last chapter. Also events with out of time photons were rejected as described in the last chapter. The maximum number of lead glass blocks allowed to be in a photon shower was four. Momentum balanced events were then selected by imposing the following cuts on the components of missing momentum,

$$\begin{aligned} |\text{missing p}_x| &< 20.0 \text{ GeV/c} \\ |\text{missing p}_y| &< 0.20 \text{ GeV/c} \\ |\text{missing p}_z| &< 0.16 \text{ GeV/c} \end{aligned}$$

The $\gamma\gamma$ signal in the η region following these cuts is shown in Fig 6.1a. To enhance the η signal over the background the following extra cuts were made on the photon energies depending on ORC type (see appendix C) :-

Itype	Energy cut (GeV)
11	4.0
12	4.0
13	2.0
15	2.0
16	4.0
17	2.0
18	2.0
20	1.0

and the following cuts on the minimum photon distance from the centre of OLGA :-

Itype	Minimum distance from OLGA centre (cm)
17	19.0
18	20.0
20	19.0

The reason for these cuts was explained in section 5.4. Also events where one or both of the photons came from a subclustered shower were rejected. The η signal produced after these cuts is shown in Fig 6.1b, and the signal that is rejected is shown in Fig 6.1c. These cuts therefore reject a lot of background at the expense of losing very little of the η.

Reaction 6.1 was then selected by requiring $0.45 < m(\gamma\gamma) < 0.65$ GeV. The momenta and energy of the two γ's were then recalculated to give the η mass. There were three possible ways of doing this. Method one assumes that the impact position is correct for each γ and that all the error comes from the energy measurement, and so recalculates the total energy of the pair in order to give the η mass. Method two changes both the energy and momenta of each γ according to the ORC code of each γ, i.e. according to whether the γ's position is given by the fingers or the blocks. It first calculates the change in separation between the two γ's needed to give the η mass. It then calculates how much it can change the two γ positions, e.g. if there is finger information in both projections then no change would be made, while if there is finger information only in the y projection then only the z position would be changed. Finally it calculates how much the energy of each γ would have to be changed to give the η mass. Using these limits it then calculates the most likely changes in position and energy of the two γ's and recalculates the momentum of the pair. Method three uses a full kinematic fit (based on the MINUIT minimisation package [36]). This recalculates the energy and momentum of each γ taking into account the expected positional and energy resolution of their measured parameters. Fig 6.2a,b,c and d show the $\eta\pi\pi$ mass spectrum for no recalculation and recalculation by methods one, two and three respectively. Methods two and three give the best resolution. It was decided to use the full kinematic fit (method three) as this gives a χ^2 for each event related to how probable are the recalculated parameters. The importance of this will be discussed later in this chapter.

To remove diffractive contributions to the spectrum the rapidity of the η, π^+ and π^- were plotted, as shown in Fig 6.3, where rapidity is defined by

$$y = \frac{1}{2} \ln \left(\frac{E + p_L}{E - p_L} \right)$$

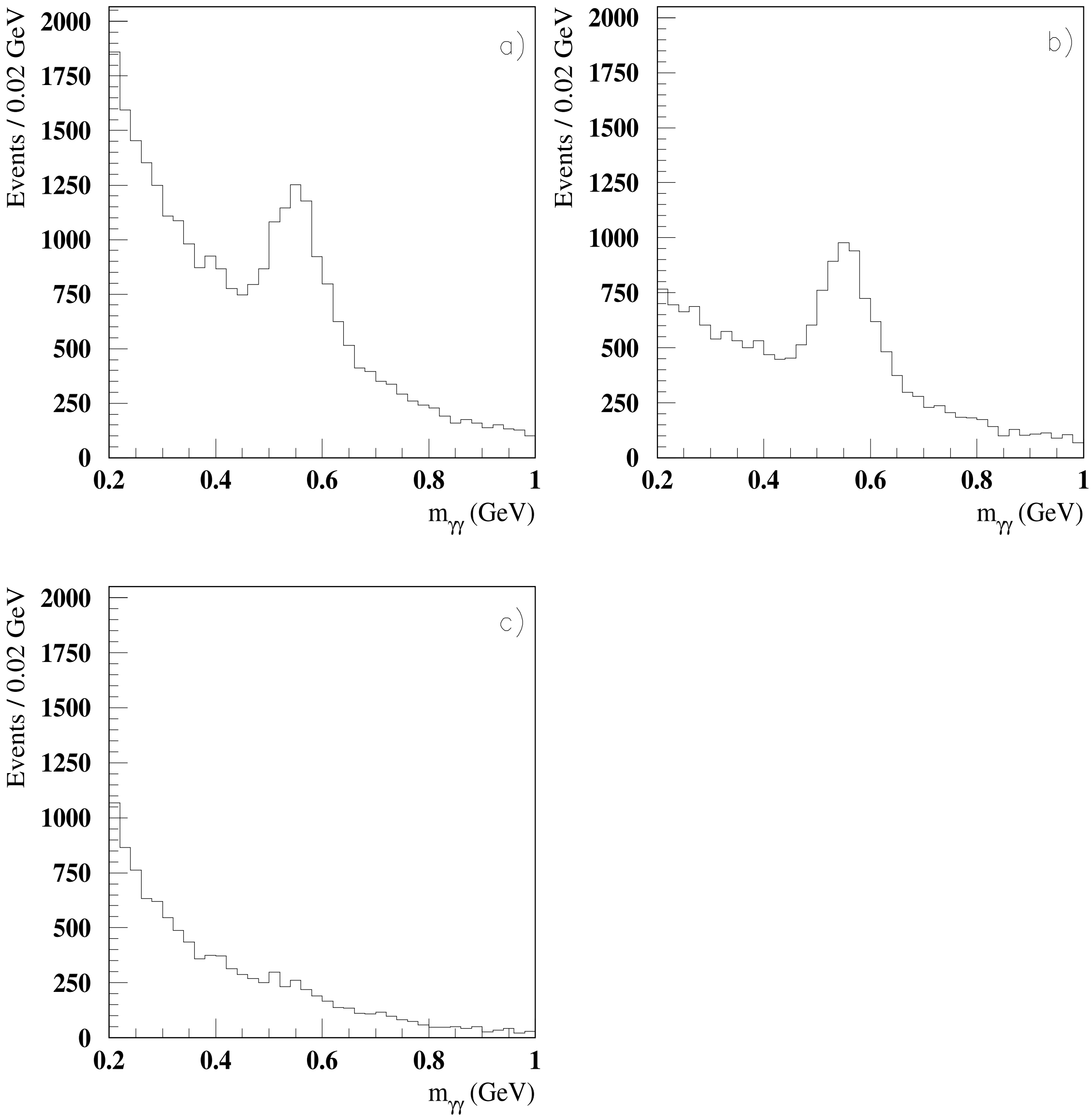

Figure 6.1: $\gamma\gamma$ spectrum after the a) initial cuts and b) secondary cuts. c) The $\gamma\gamma$ signal rejected by the secondary cuts.

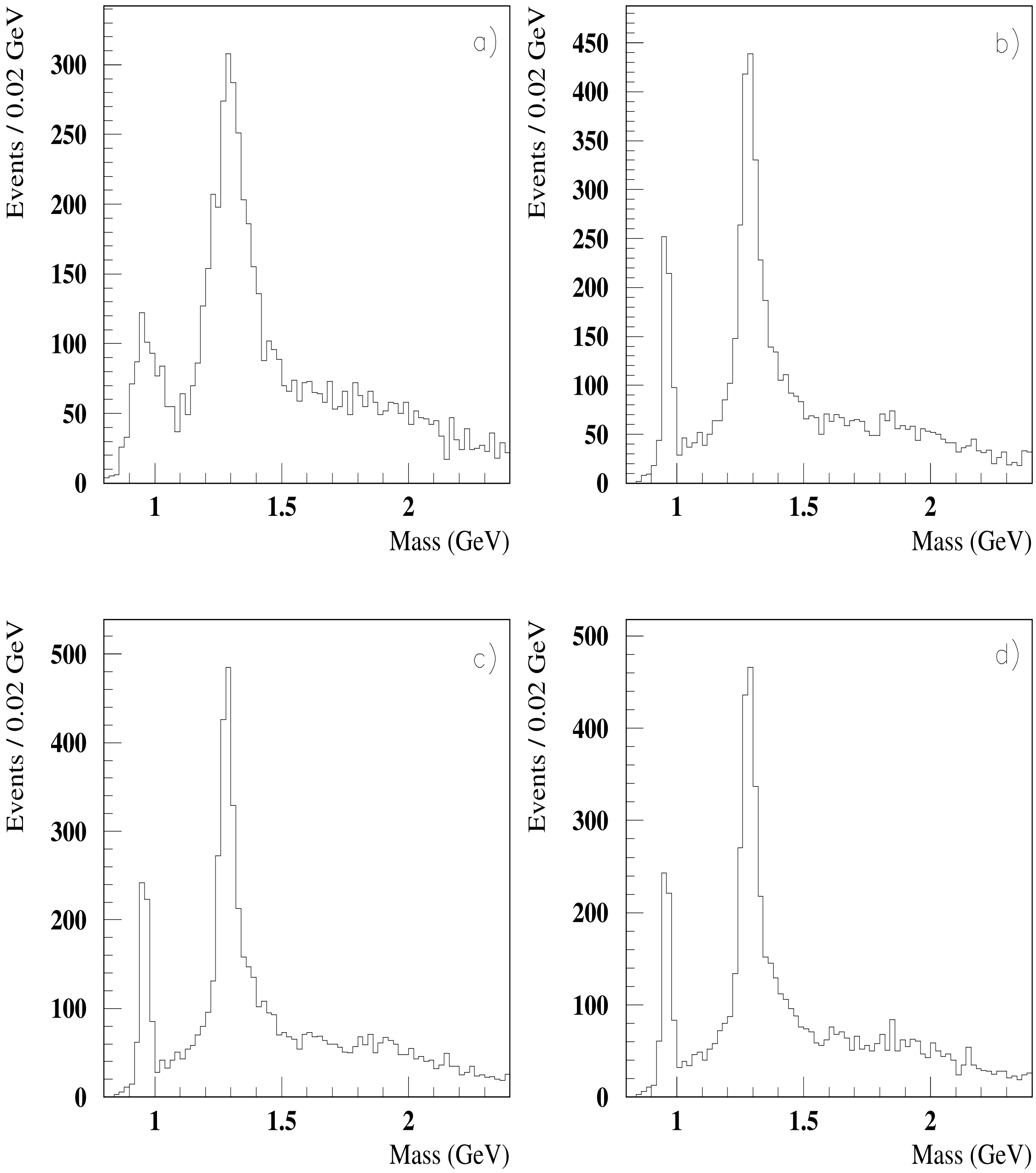

Figure 6.2: $\eta\pi\pi$ mass spectrum using various methods for recalculating the γ energy and momentum, as described in the text.

where E and P_L are the energy and longitudinal momentum of the particle in the centre of mass system. There is an enhancement in the π^+ and a smaller one in the π^- around the rapidity of the fast proton. Plotting the $p_f\pi^+$ mass shows a clear diffractive Δ^{++} signal, while the $p_f\pi^-$ spectrum shows a small enhancement at the Δ^0 mass, as shown in Fig 6.4. Both of these signals are removed by rapidity cuts of $y < 1.9$ on the π^+ and π^-, the remaining signal is shown as the cross-hatched sections of Fig 6.4. The final sample consists of 6106 events for which the $\eta\pi\pi$ effective mass distribution is shown in Fig 6.5. There are clear peaks at the $\eta'(958)$ and $f_1(1285)$ masses, but no clear evidence for structures in the E/ι region. This will be discussed further in section 6.3.

6.2.2 Selection of $\eta \rightarrow \pi^+\pi^-\pi^0$

The reaction

$$pp \rightarrow p_f(\pi^+\pi^-\eta_{\rightarrow\pi^+\pi^-\pi^0})p_s \tag{6.2}$$

has been selected from the sample of events having six outgoing tracks and two reconstructed γ's in the electromagnetic calorimeter OLGA. An energy cut of 1 GeV was imposed on the γ's, except for type 20 γ's where the cut was increased to 1.4 GeV. Showers associated with charged tracks were also removed. Momentum balanced events were then selected by imposing the following cuts on the components of missing momentum,

$$\begin{aligned} |\text{missing } p_x| &< 20.0 \text{ GeV/c} \\ |\text{missing } p_y| &< 0.20 \text{ GeV/c} \\ |\text{missing } p_z| &< 0.16 \text{ GeV/c} \end{aligned}$$

Photons of type 17, 18 and 20 were rejected if they came within 19 cm of the centre of OLGA. The $\gamma\gamma$ mass spectrum for events passing these cuts is shown in Fig 6.6. The π^0 signal was selected by requiring $0.10 < m(\gamma\gamma) < 0.17$ GeV. The γ momenta and energies were recalculated to give the π^0 mass using method three as explained above. Energy balance was obtained by calculating the function Δ, where

$$\Delta = MM^2(p_f p_s) - M^2(2\pi^+2\pi^-\pi^0)$$

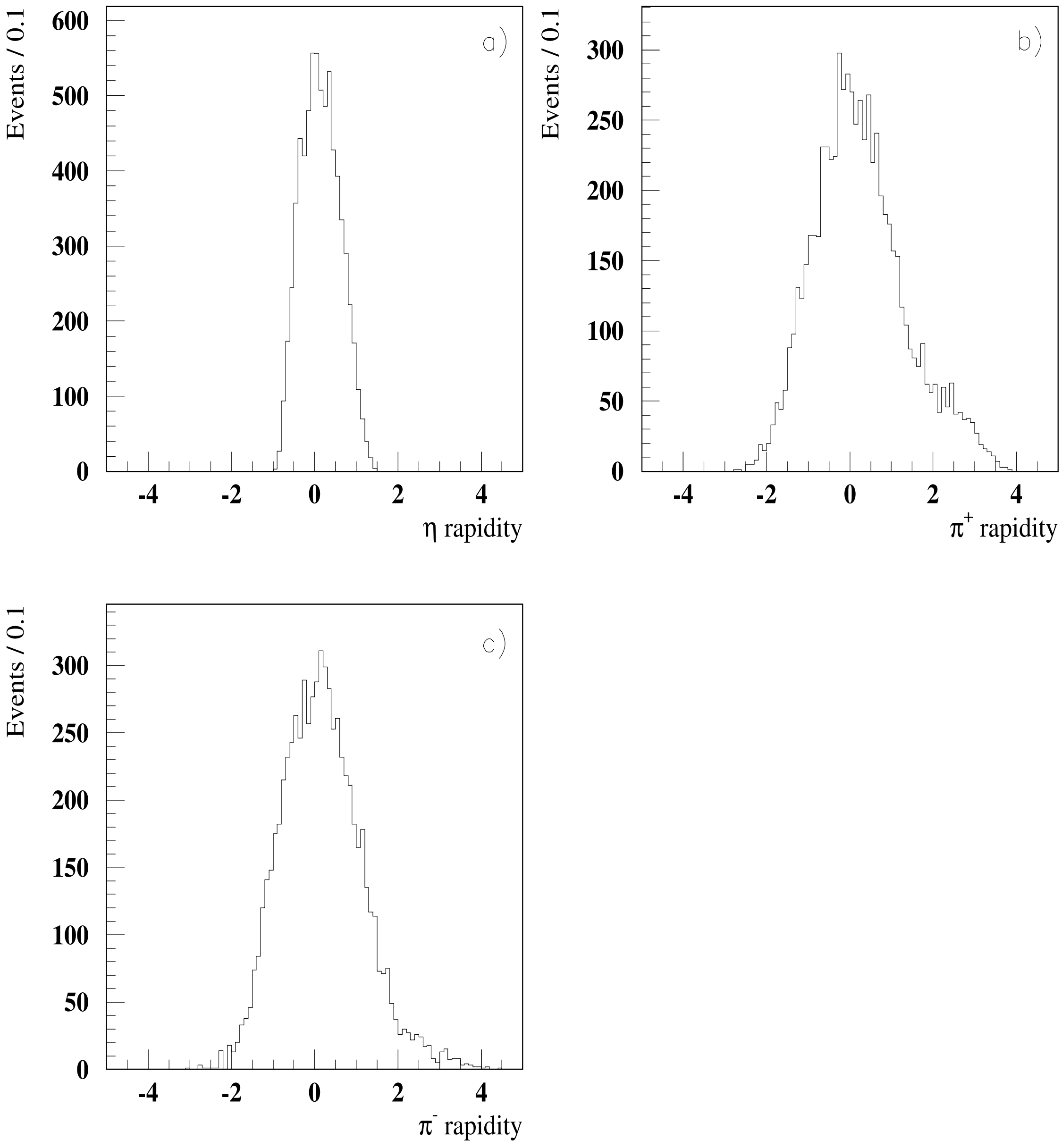

Figure 6.3: a) η b) π^+ and c) π^- rapidities.

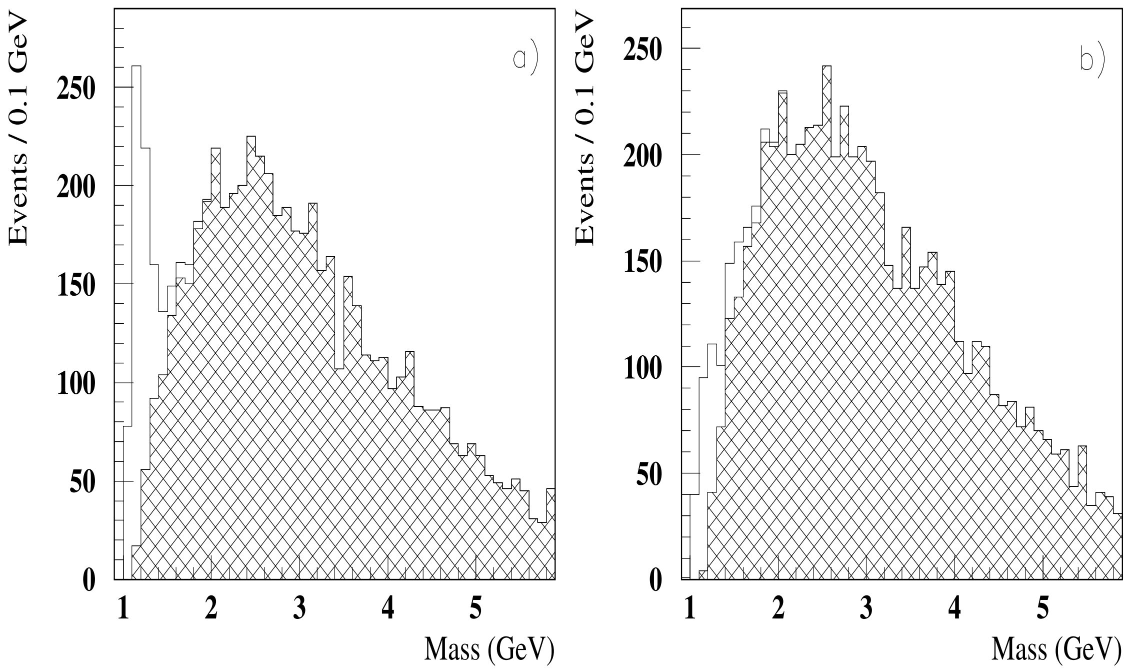

Figure 6.4: a) $p_f\pi^+$ and b) $p_f\pi^-$ mass spectra. The cross-hatched sections are for rapidity cuts of $y_\pi < 1.9$, as explained in the text.

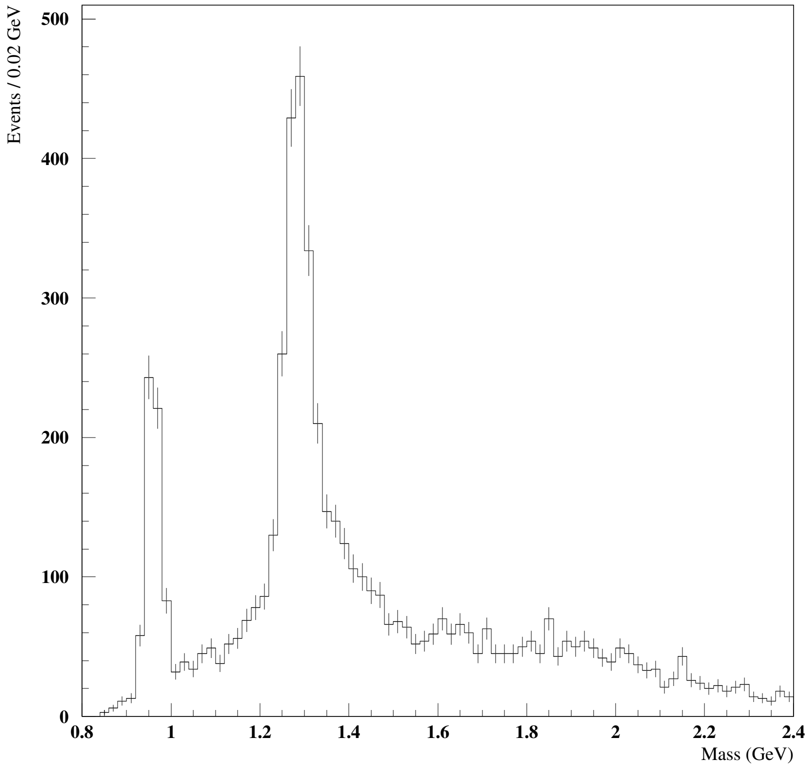

Figure 6.5: The $\eta\pi^+\pi^-$ mass spectrum for $\eta \to \gamma\gamma$.

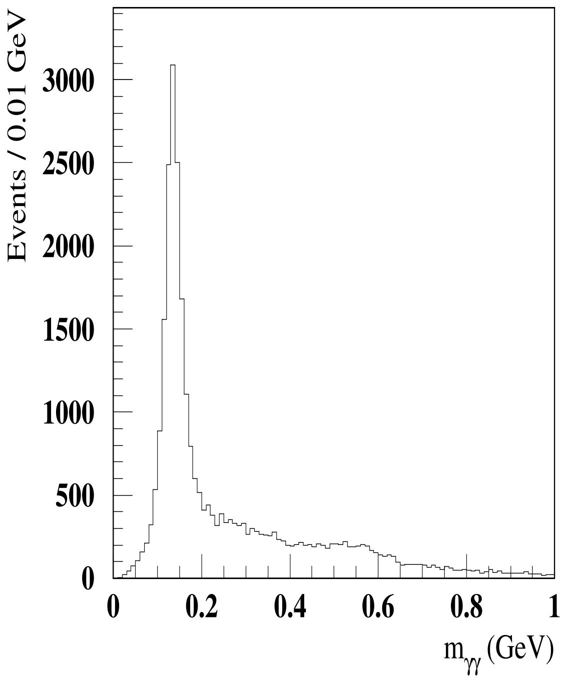

Figure 6.6: The $\gamma\gamma$ mass spectrum for the $\pi^+\pi^-\pi^+\pi^-\gamma\gamma$ system.

where MM^2 is the missing mass squared of the proton proton system, i.e. $((p_{beam} + p_{target}) - (p_f + p_s))^2$, and M^2 is the mass squared of the 5 pion system, assuming the charged tracks to be all pions. A cut of $|\Delta| < 3.0$ GeV^2 then isolates the $2\pi^+2\pi^-\pi^0$ channel. On plotting the $p_f\pi^+$ mass spectrum a clear Δ^{++} signal was seen, which was removed by requiring $m(p_f\pi^+) > 1.3$ GeV. No evidence was seen for diffractive Δ^+ or Δ^0 production.

Fig 6.7 shows the $\pi^+\pi^-\pi^0$ effective mass spectrum (4 combinations per event), where clear η and $\omega(783)$ signals can be seen, showing evidence for centrally produced $\eta\pi^+\pi^-$ and $\omega\pi^+\pi^-$ final states. Reaction 6.2 was then selected by computing the four possible $\pi^+\pi^-\pi^0$ mass combinations, keeping the nearest one to the η mass, and requiring that for this combination $0.507 < m(\pi^+\pi^-\pi^0) < 0.587$. The energy of the combination is then recalculated to give the η mass. The final sample consists of 683 events, the $\eta\pi\pi$ effective mass of which is shown in Fig 6.8. Once again there are clear $\eta'(958)$ and $f_1(1285)$ signals.

6.3 Study of the $\eta\pi^+\pi^-$ mass spectrum

The combined $\eta\pi^+\pi^-$ mass spectrum for reactions 6.1 and 6.2 is shown in Fig 6.9. The Feynman x_F distributions for the fast proton, slow proton and $\eta\pi^+\pi^-$ system are

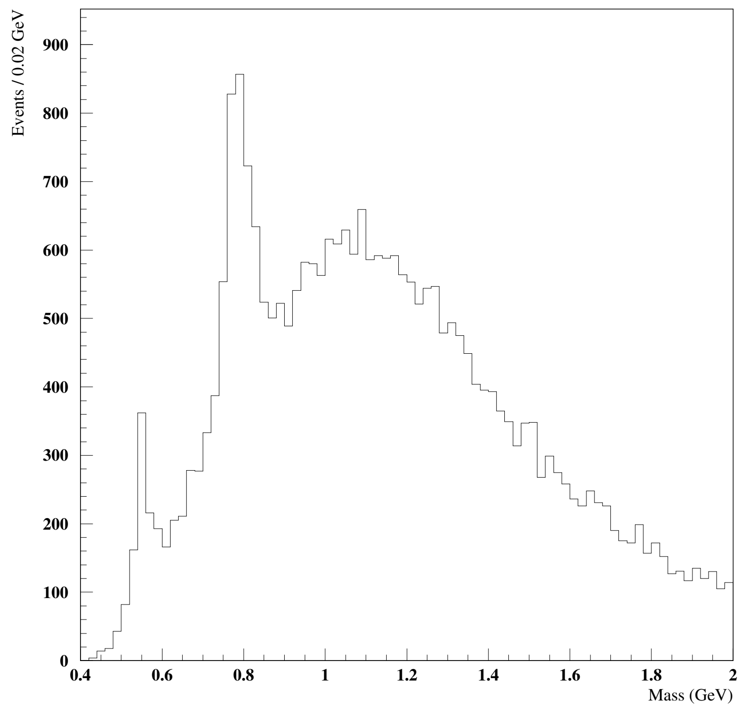

Figure 6.7: The $\pi^+\pi^-\pi^0$ mass spectrum coming from $2\pi^+2\pi^-\pi^0$.

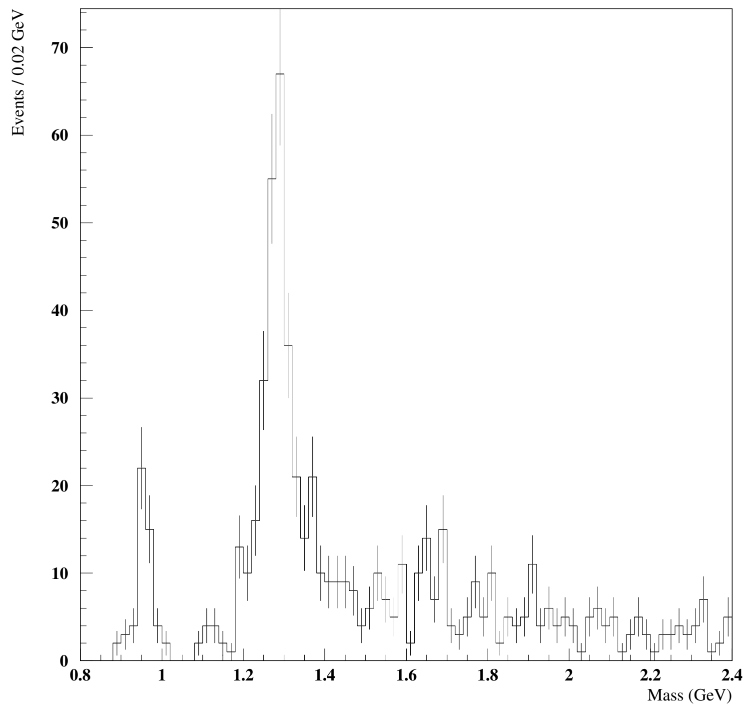

Figure 6.8: The $\eta\pi^+\pi^-$ mass spectrum, for $\eta \to \pi^+\pi^-\pi^0$.

shown in Fig 6.10, where the centrally produced system is clearly separated from the fast and slow protons. An initial fit was performed using a Gaussian to describe the

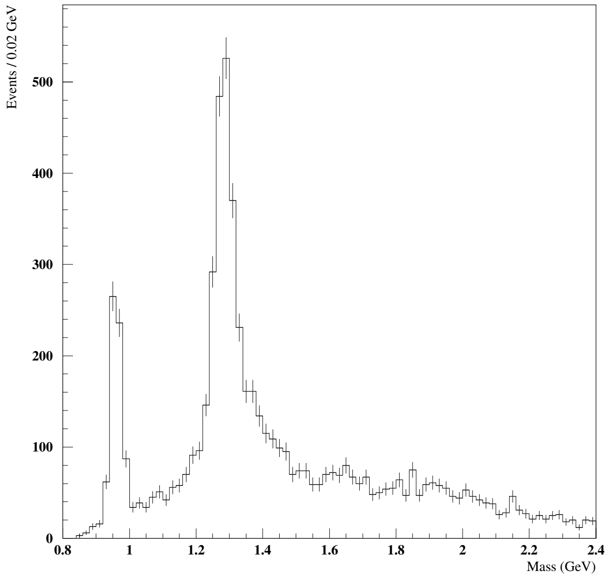

Figure 6.9: The combined $\eta\pi^+\pi^-$ mass spectrum.

$\eta'(958)$ and a Gaussian convoluted with a spin 1 relativistic Breit-Wigner (decaying to $\delta/\mathrm{a}_0(980)\pi$) for the $\mathrm{f}_1(1285)$. The Breit-Wigner width was fixed at the Particle Data Book [38] value of 24 MeV, and the Gaussian widths were allowed to vary to represent the experimental resolution. A background of the form

$$Bgnd(m) \;=\; (m - m_{th})^{\alpha} exp(-\beta m - \gamma m^2)$$

was used, where m is the $\eta\pi^+\pi^-$ mass, $\mathrm{m_{th}}$ is the $\eta\pi^+\pi^-$ threshold mass and α, β, γ are fit parameters. The results of the fit are

$$\begin{aligned} m_{\eta'(958)} &= 957 \pm 1\ MeV \\ \sigma_{\eta'(958)} &= 16 \pm 1\ MeV \\ m_{\mathrm{f}_1(1285)} &= 1285 \pm 1\ MeV \\ \sigma_{\mathrm{f}_1(1285)} &= 23 \pm 2\ MeV \end{aligned}$$

with a χ^2/NDF of 124/70, as shown in Fig 6.11a. There is an excess of events in 1400 MeV region, and the fit is poor in the higher mass region. A Breit-Wigner (called resonance Y) with free mass and width was introduced to describe the excess in the

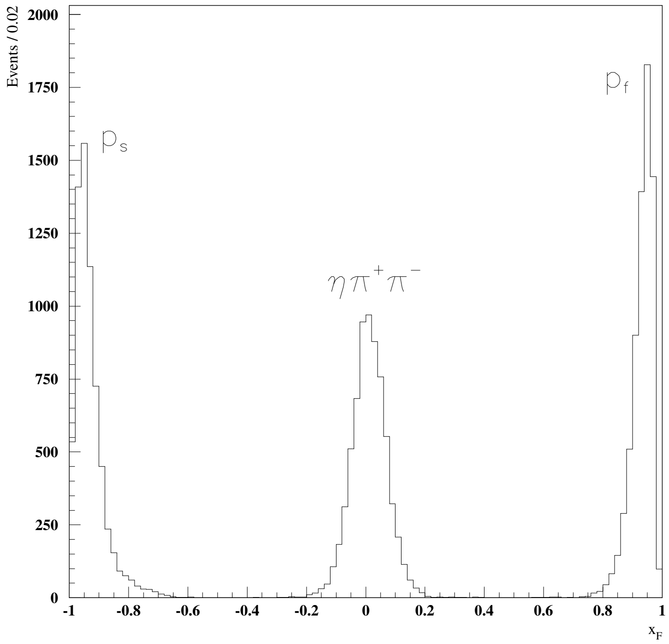

Figure 6.10: The Feynman x_F distributions for the slow proton, the $\eta\pi^+\pi^-$ system and the fast proton.

1400 MeV region, and gave

$$m_Y = 1373 \pm 14\ MeV$$
$$\Gamma_Y = 76 \pm 19\ MeV$$

with a χ^2/NDF of 83/67, as shown in Fig 6.11b. There is still an excess of events in the 1900 MeV region. A Breit-Wigner (resonance X(1900)) with free mass and width was introduced to describe this region, and gave

$$m_{\mathrm{X(1900)}} = 1960 \pm 52\ MeV$$
$$\Gamma_{\mathrm{X(1900)}} = 324 \pm 85\ MeV$$

with a χ^2/NDF of 61/64, as shown in Fig 6.12a. If the X(1900) resonance is introduced on its own the resulting fit has a χ^2/NDF of 111/67, as shown in Fig 6.12b. There is no improvement in any of the fits if a Breit-Wigner is introduced to describe the 1650 MeV region.

The X(1900)has been seen in the 4π channel in both the 300 GeV/c and 450 GeV/c data [34, 35], where it is seen to decay equally to $f_2(1270)\pi^+\pi^-$ and $a_2(1320)\pi$.

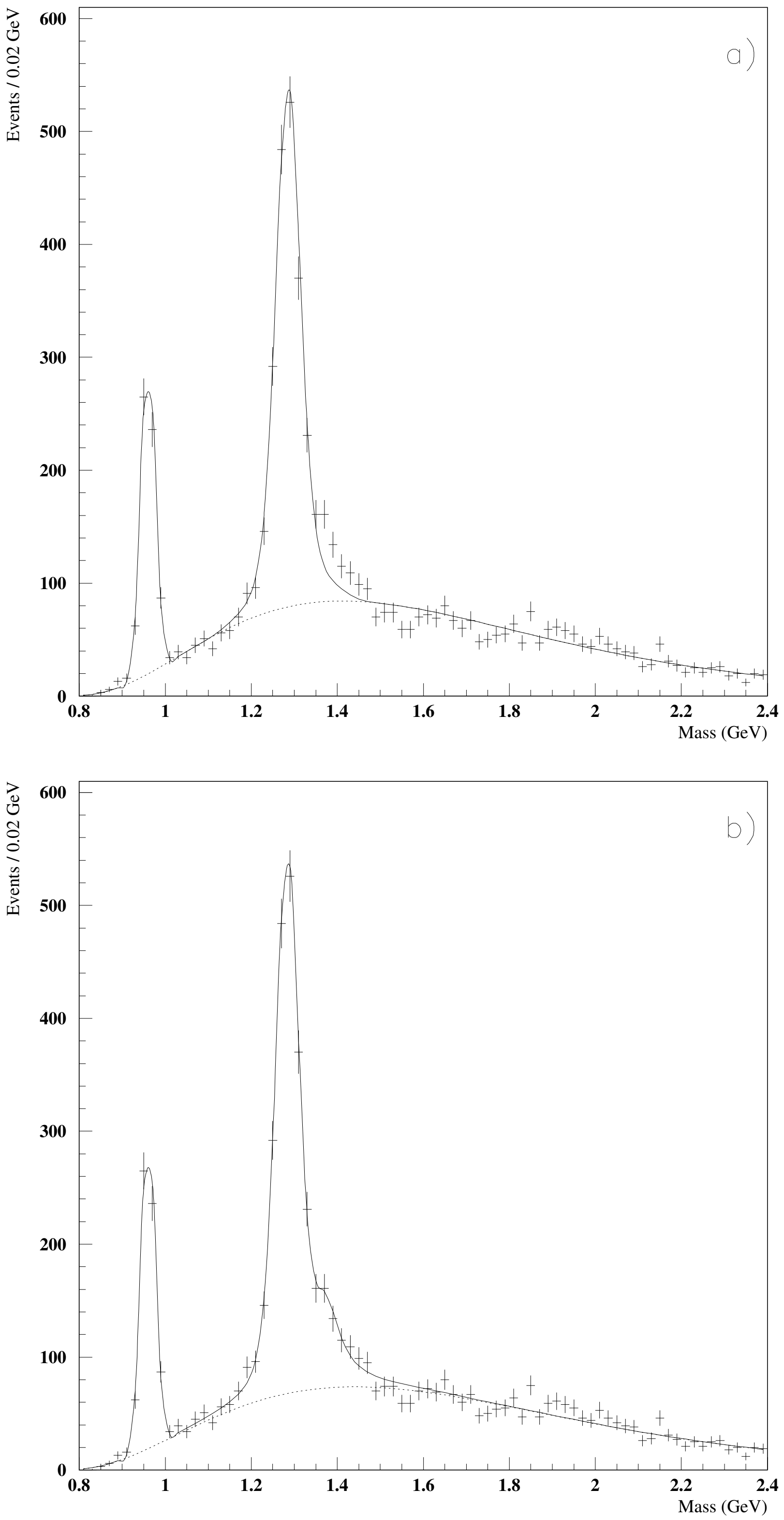

Figure 6.11: Fits to the $\eta\pi^+\pi^-$ mass spectrum, as described in the text.

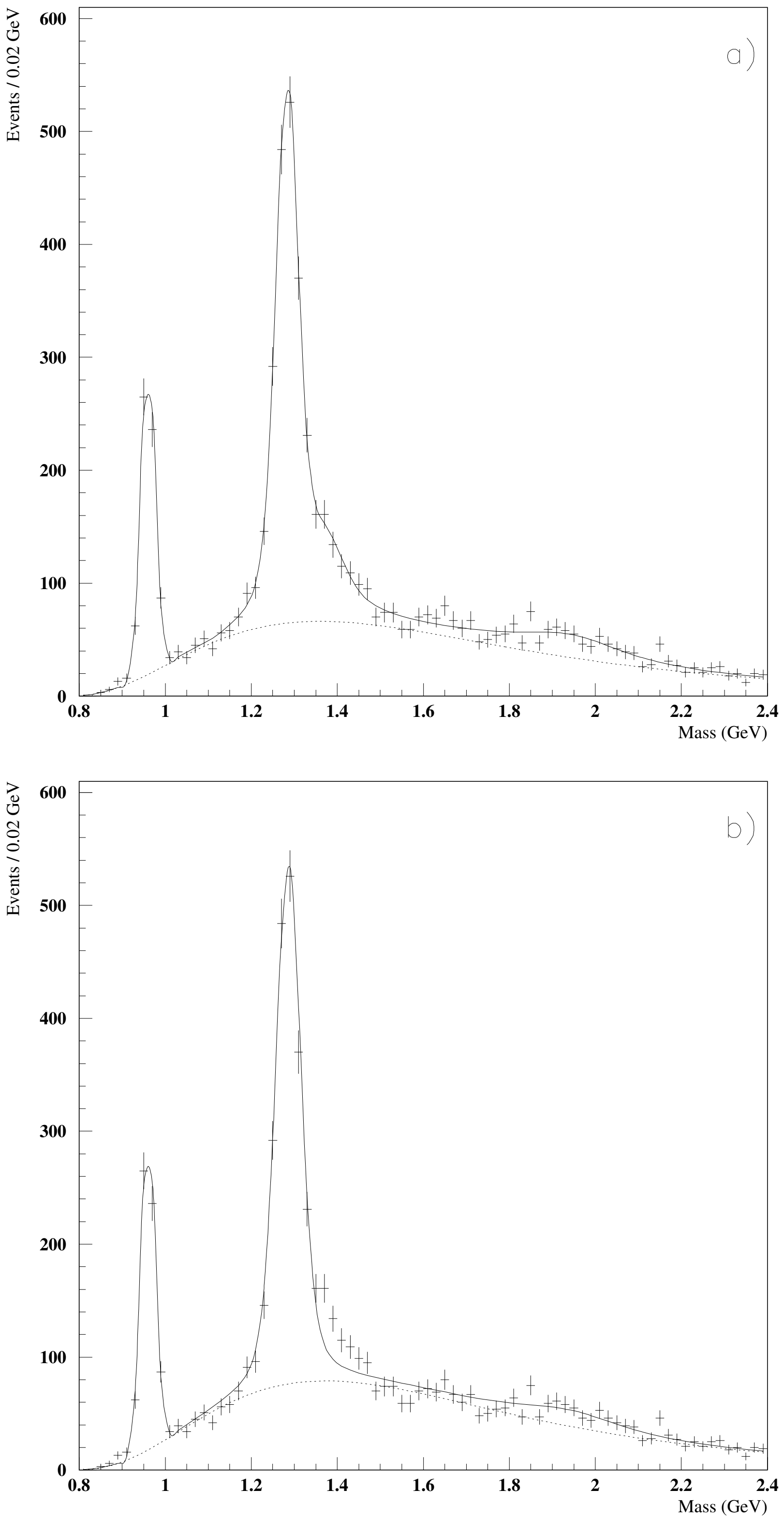

Figure 6.12: Fits to the $\eta\pi^+\pi^-$ mass spectrum, as described in the text.

This second decay mode implies that the X(1900) should also be seen in the $\eta\pi^+\pi^-$ channel. The parameters from the 450 GeV/c data are mass 1926±12 MeV, width 370±70 MeV, and $J^{PC} = 2^{++}$. In the 4π channel there was 3 times as much X(1900) produced as there was $f_1(1285)$. From the Particle Data Group the $f_1(1285)$ is 1.3 times more likely to decay to $\eta\pi^+\pi^-$ as to 4π. The X(1900) decayed 50% to $a_2(1320)\pi$, and the $a_2(1320)$ is 5 times less likely to decay to $\eta\pi$ as to $\rho\pi$. This implies that in the $\eta\pi^+\pi^-$ channel there should be 4 times less X(1900) produced as $f_1(1285)$. This is consistent with what is seen, where there are 1848±45 $f_1(1285)$ events and 334±124 X(1900) events in the $\eta\pi^+\pi^-$ mass plot.

6.4 Further study of the $\eta\pi^+\pi^-$ mass spectrum

It is necessary to try and establish whether the resonances seen in the 1380 and 1900 MeV regions are real or whether they are artificially produced by the method used to obtain and fit the mass spectrum. There are three possible ways this could happen :-

- The fitting program could be underestimating the experimental resolution, in which case the fit to the $f_1(1285)$ should be broader, perhaps eliminating the excess of events in the 1380 MeV region.
- The resonances may be due to poorly reconstructed photons, i.e. those with missing finger information and thus poorer positional resolution.
- The resonances may be due to the way the photon energy and momentum are recalculated in the kinematic fit.

6.4.1 Investigation of the experimental resolution

In order to eliminate the excess of events in the Y mass region with a broad $f_1(1285)$, the experimental resolution needs to be around 40 MeV at the $f_1(1285)$ mass (found by fixing the Gaussian width of the $f_1(1285)$ to increasing values until the excess is fitted - the χ^2/NDF at this width is 215/68). A Monte Carlo simulation of the decay

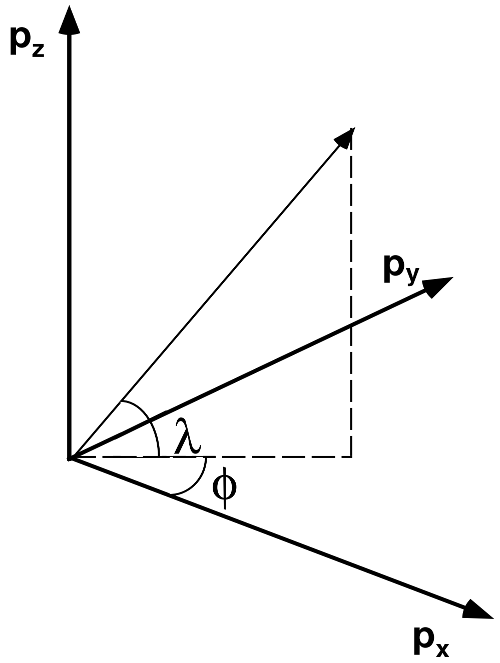

Figure 6.13: The λ and ϕ angles used in smearing the medium momentum tracks.

of a central system to $\eta\pi^+\pi^-$ was performed to estimate the expected experimental resolution. Event mixing of real $\pi^+\pi^-$ events was used to simulate the central system. For each event the effective mass of the $\pi^+\pi^-$ is calculated, and then this system is allowed to decay to $\eta\pi^+\pi^-$. The η is then allowed to decay to $\gamma\gamma$ (the resolution is estimated for $\eta \rightarrow \gamma\gamma$ only as there are ≈ 9 times more of these events than $\eta \rightarrow \pi^+\pi^-\pi^0$, and the resolution is worse for this decay). The momentum components of the fast and slow protons are then smeared according to the formula

$$\delta p = \frac{\alpha p^2}{\sqrt{2\pi}\sigma} \exp(-\frac{p^2}{2\sigma^2})$$

where σ is 2 GeV and α is 1×10^{-5} for the fast proton, and σ is 100 GeV and α is 1×10^{-3} for the slow proton. The pions are then smeared in momentum with a Gaussian with a σ of 5 GeV and α equal to 1×10^{-4}, in azimuthal angle ϕ by a Gaussian of width 6×10^{-4}, and in the angle of dip of the track λ by a Gaussian of width 9×10^{-4} (see Fig 6.13). These values have been found from a GEANT [39] simulation of the apparatus, and confirmed by a comparison of the simulated and observed widths in the $\mathrm{K\overline{K}}\pi$ channel. A decay vertex is then generated, and using this the photons and charged tracks are traced to OLGA.

The energy of each photon is then smeared by a Gaussian with a σ given by

$$\frac{\sigma(E)}{E} = 0.025 + \frac{0.16}{\sqrt{E}}$$

and the y and z coordinates are smeared by Gaussians with a σ of 0.7 cm (if the coordinate is measured by the fingers) or 4.0 cm (if the coordinate is measured by the lead glass blocks) where these values have been estimated initially from the test beam, and then set by comparing the resolution of the π^0 and η generated from the Monte Carlo with those in the real data. The photons must then pass the following cuts, which are the same as for the real events :-

1. Both photons must hit within the boundaries of OLGA ($\mid y \mid < 128$ cm, $\mid z \mid < 110$ cm).

2. Neither photon must hit at the position of the central hole (given by $-4 < y < 10$ cm, $-7.8 < z < 6.2$ cm).

3. The photons must be separated by at least 20 cm.

4. The photons must not hit within a circle of radius 16 cm from a charged track impact on OLGA.

5. The photons must pass the energy cuts and the cuts on the distance from the OLGA centre given in 6.2.1.

In the real data, after the cuts, the photons are distributed thus :-

51.2% type A (finger information in y and z)
33.9% type B (finger information in y or z)
14.9% type C (block information in y and z)

The Monte Carlo photons are generated in this proportion, and their y and z coordinates smeared accordingly. The η signal in the $\gamma\gamma$ spectrum is then selected using the same cut as for the real data, and the $\eta\pi^+\pi^-$ effective mass calculated. If the difference between the input mass and the smeared mass is plotted for each

	Real data		Monte Carlo	
	$\eta'(958)$	$f_1(1285)$	$\eta'(958)$	$f_1(1285)$
No recalculation	50 ± 3	59 ± 4	44	54
Energy recalculation	16 ± 1	30 ± 2	16	29
Kinematic fit	16 ± 1	23 ± 2	15	26

Table 6.1: Comparison of the observed and Monte Carlo resolutions for various recalculation methods (all widths in MeV).

generated event, then a Gaussian is produced whose σ represents the resolution of the $\eta\pi^+\pi^-$ channel. This has been done when the η energy/momentum have not been recalculated, when the energy only has been recalculated (method 1 of section 6.2.1) and for the full kinematic fit (method 3). The results are shown in table 6.1, and shows that the measured widths are consistent with the expected ones. Thus the 1400 MeV region cannot be explained by the resolution.

6.4.2 Investigation of photon types

There are three major classes of photon that are measured by OLGA - those with both y and z coordinates measured by the fingers (class A), those with either y or z measured by the fingers and the other coordinate measured by the blocks (class B), and those with both y and z measured by the blocks (class C). The $\eta\pi^+\pi^-$ mass spectrum can be split up according to what class the photons belong to. This is shown in Fig 6.14, where events with two class A photons, one class A and one class B photon, and those with no class A photons are plotted. Each plot has been fitted using the $\eta'(958)$, $f_1(1285)$ and X(1900) (represented as described in section 6.3). It can be seen that although there is an excess of events in the 1400 MeV region in all the plots, it is more prominent in the class A-B and no A events, while for the class A-A events, which have the most accurately reconstructed photons and would be expected to give the most reliable results, the excess is quite small. This could indicate that this 'resonance' may in fact have been artificially introduced due to poorly measured photons. The peak around 1650 MeV is also seen to be

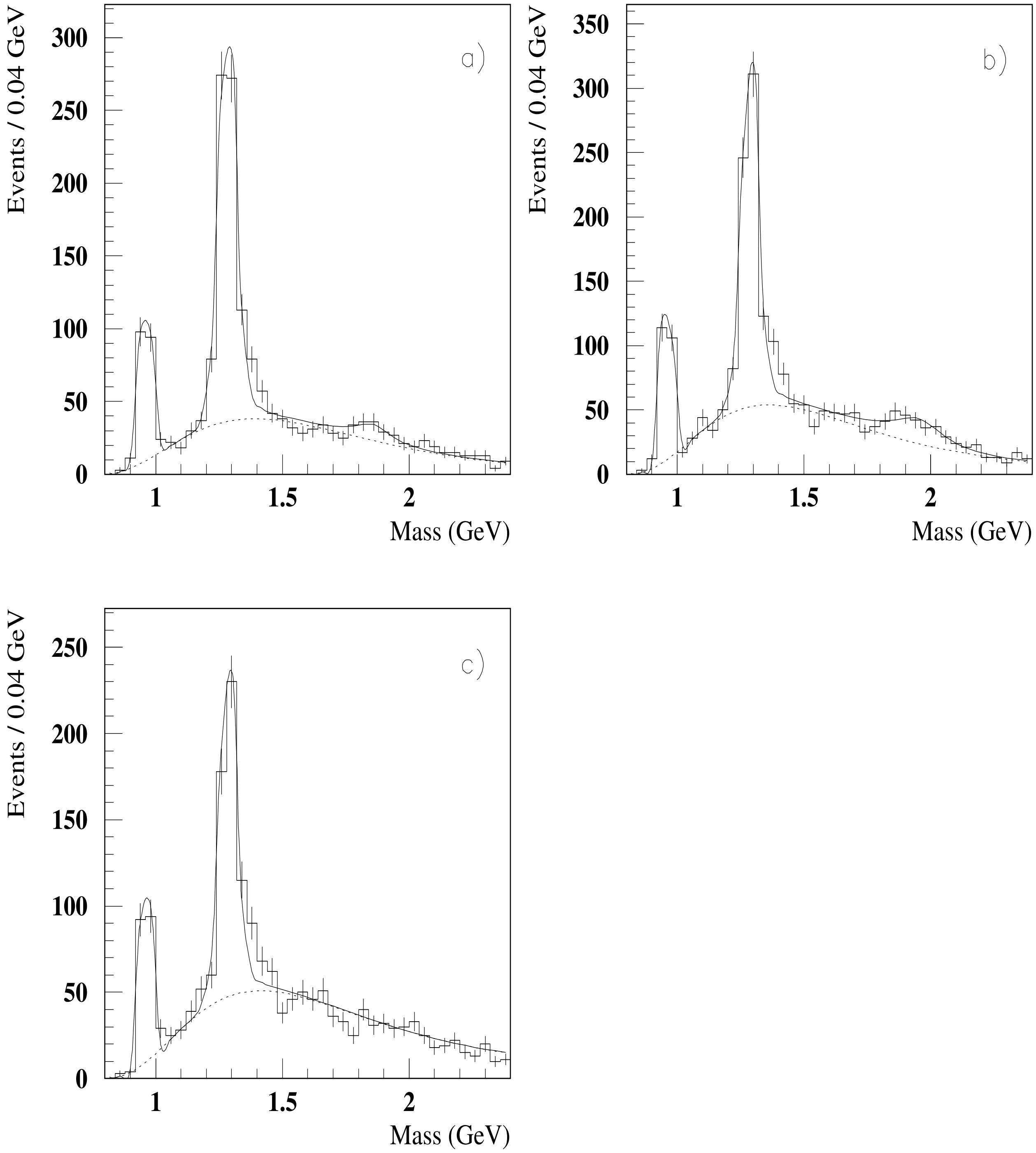

Figure 6.14: $\eta\pi^+\pi^-$ mass spectrum for events with a) A-A, b) A-B and c) no A class photons. The fits are described in the text.

predominately in the events with no class A photons. The parameters of the X(1900) found from the fit to the class A-A photons are

$$\begin{aligned} m_{\mathrm{X}(1900)} &= 1864 \ \pm \ 29 \ MeV \\ \Gamma_{\mathrm{X}(1900)} &= 165 \ \pm \ 42 \ MeV \end{aligned}$$

with a χ^2/NDF of 33.9/27. The significance of this will be taken up in the next chapter.

6.4.3 Investigation of the kinematic fit

The kinematic fitting routine takes the energy and coordinates of the photons for each event and using the energy and positional resolutions (which depend on whether the coordinates are measured by the fingers or the blocks) works out the best change in these parameters in order to give the η mass (or π^0 mass if the η decays to $\pi^+\pi^-\pi^0$). Each event has a χ^2/NDF associated with it whose value depends on how likely are the new parameters. Thus by making cuts on χ^2/NDF the best refitted events can be selected. This is shown in Fig 6.15, where the mass spectra have been plotted for events with $\chi^2 \leq 3.0$ (Fig 6.15a), $\chi^2 > 3.0$ (Fig 6.15b), $\chi^2 \leq 1.0$ (Fig 6.15c) and for $\chi^2 > 1.0$ (Fig 6.15d). For $\chi^2 \leq 3.0$ and $\chi^2 \leq 1.0$ the spectra have been fitted with an $\eta'(958)$, $f_1(1285)$ and X(1900), while for the other plots the Y resonance has also been added (all represented as described in section 6.3). As the cut on χ^2 is tightened, the need for the Y resonance is removed, whereas the X(1900) remains. Indeed all of the Y resonance appears in the high χ^2 events. The results of the fit to the low χ^2 events are summarised in Table 6.2. The parameters obtained for the $\eta'(958)$ and $f_1(1285)$ are consistent with those found in section 6.3.

It would thus seem that the structure found in the 1400 MeV region is in fact not a resonance but has been caused by attempting to force the $\gamma\gamma$ pair for events with poorly reconstructed γ parameters to have a good η mass. The X(1900) however appears just as strongly in the best $\eta\pi\pi$ events (class A-A and low χ^2 events) and would appear to be a real resonance. The parameters of the X(1900) from these

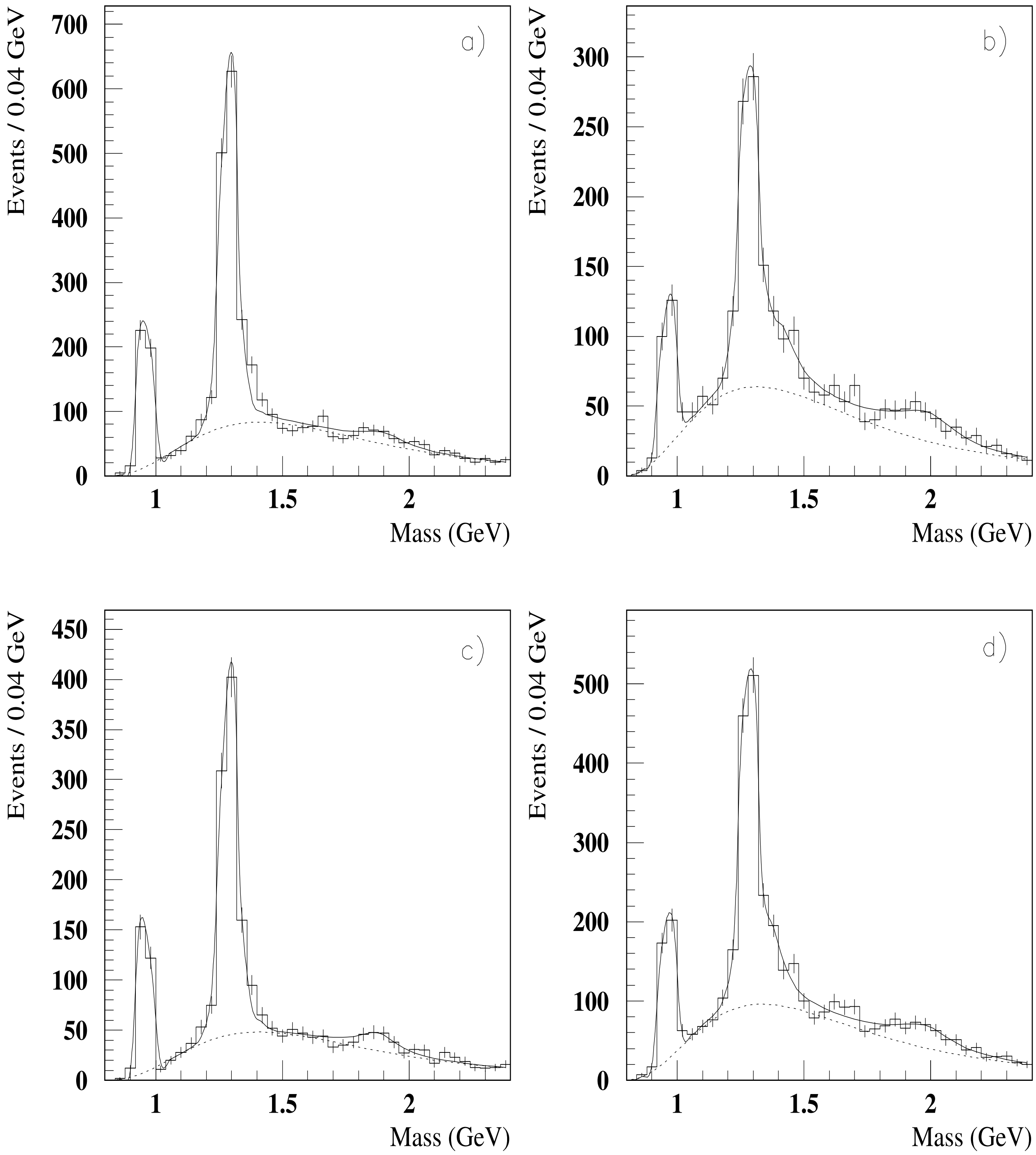

Figure 6.15: $\eta\pi^+\pi^-$ mass spectrum for events with a) $\chi^2 \leq 3.0$, b) $\chi^2 > 3.0$, c) $\chi^2 \leq 1.0$ and d) $\chi^2 > 1.0$. The fits are described in the text.

χ^2 cut	χ^2/NDF ($\eta\pi\pi$ fit)	Mass X(1900) (MeV)	Width X(1900) (MeV)
≤ 3.0	52.2/27	1902±29	201±57
≤ 1.0	32.1/27	1882±24	172±46

Table 6.2: The X(1900) and Y parameters coming from fits to the $\eta\pi^+\pi^-$ mass spectrum for various cuts on an event's χ^2.

good events are quite interesting when compared with the 4π channel. In the spin analysis of the 4π channel, although it was found that the X(1900) decayed equally to $f_2(1270)\pi\pi$ and $a_2(1320)\pi$, the event shapes peaked at different masses [35]. This implied the broad X(1900) could actually be two different resonances, a higher mass one decaying to $f_2(1270)\pi\pi$ and a lower mass one decaying to $a_2(1320)\pi$. The spin analysis gives this lower mass resonance a mass and width of around 1850 and 200 MeV respectively. This is consistent with the parameters found from the best $\eta\pi^+\pi^-$ events, although the statistics are too limited to provide conclusive evidence for the splitting of the X(1900).

6.5 Study of the 2 body mass spectra

In order to examine the decay mechanism of the $f_1(1285)$ and the X(1900), the $\eta\pi^\pm$ and $\pi^+\pi^-$ effective mass distributions were plotted, having removed the $\eta'(958)$ region ($m_{\eta\pi^+\pi^-} < 1.1$ GeV). This is shown in Fig 6.16. There is a strong $\delta/a_0(980)$ signal along with some $a_2(1320)$ in the $\eta\pi^\pm$ mass spectrum. The $\pi^+\pi^-$ mass spectrum shows no evidence for $\rho(770)$ or $f_0(1400)$ production. The $\eta\pi^\pm$ mass spectrum has been fitted using a relativistic spin 0 Breit-Wigner with free mass and width to describe the $\delta/a_0(980)$, and a relativistic spin 2 Breit-Wigner to describe the $a_2(1320)$, with width fixed to the PDG value of 110 MeV. The fit gives

$$\begin{aligned} m_{\delta/\mathrm{a}_0(980)} &= 989 \pm 2\ MeV \\ \Gamma_{\delta/\mathrm{a}_0(980)} &= 93 \pm 6\ MeV \\ m_{\mathrm{a}_2(1320)} &= 1328 \pm 15\ MeV \end{aligned}$$

which are consistent with the PDG values. The correlation between the $\eta\pi^+\pi^-$ system and the resonances observed in the $\eta\pi^\pm$ system can be seen by plotting $m(\eta\pi^\pm)$ against $m(\eta\pi^+\pi^-)$ (2 combinations per event), as shown in Fig 6.17. A clear correlation between the $\delta/a_0(980)$ and the $f_1(1285)$ can be seen, showing the $\delta/a_0(980)\pi$ decay mode of the $f_1(1285)$. The vertical band is due to the fact that when one $\eta\pi$ combination is in the $\delta/a_0(980)$ region, the other combination is below it. If the $\delta/a_0(980)$ is selected, by requiring either $\eta\pi$ combination to have $0.88 < m(\eta\pi) < 1.08$ GeV, and the $\delta/a_0(980)\pi$ effective mass plotted, then Fig 6.18 is produced, where the $f_1(1285)$ is clearly reproduced.

If the X(1900) mass region is selected ($1.76 < m(\eta\pi\pi) < 2.08\,\mathrm{GeV}$) and the $\eta\pi^\pm$ mass plotted, then a clear $a_2(1320)$ signal is seen (Fig 6.19) which is consistent with the expected $a_2(1320)\pi$ decay mode of the X(1900).

6.6 Geometrical Acceptance

The WA91 experiment has been designed using the available apparatus to maximise the recording of charged tracks and photons per event. However the experiment does not have total acceptance, and so it is necessary to study the effect that the geometrical acceptance has on the $\eta\pi\pi$ channel, and in particular whether acceptance effects are responsible for the presence of the X(1900).

The acceptance of the apparatus for the $\eta\pi\pi$ channel is studied using the method of mixing of real events. This method is used due to the lack of a well established Monte Carlo simulation of central production via Double Pomeron Exchange. Real $\pi^+\pi^-$ events are taken, and then 500000 new events generated by randomly taking a beam, target, fast and slow proton and a π^+ and π^- from different real events. The new mixed event must balance momentum within experimental limits. The 2 pions are combined to create a central X^0, and then this is allowed to decay to $\eta\pi^+\pi^-$, and the η allowed to decay to $\gamma\gamma$ or to $\pi^+\pi^-\pi^0$ with the π^0 decaying to $\gamma\gamma$, depending on for which decay mode the acceptance is being calculated. A random decay vertex position within the target is generated and the protons and

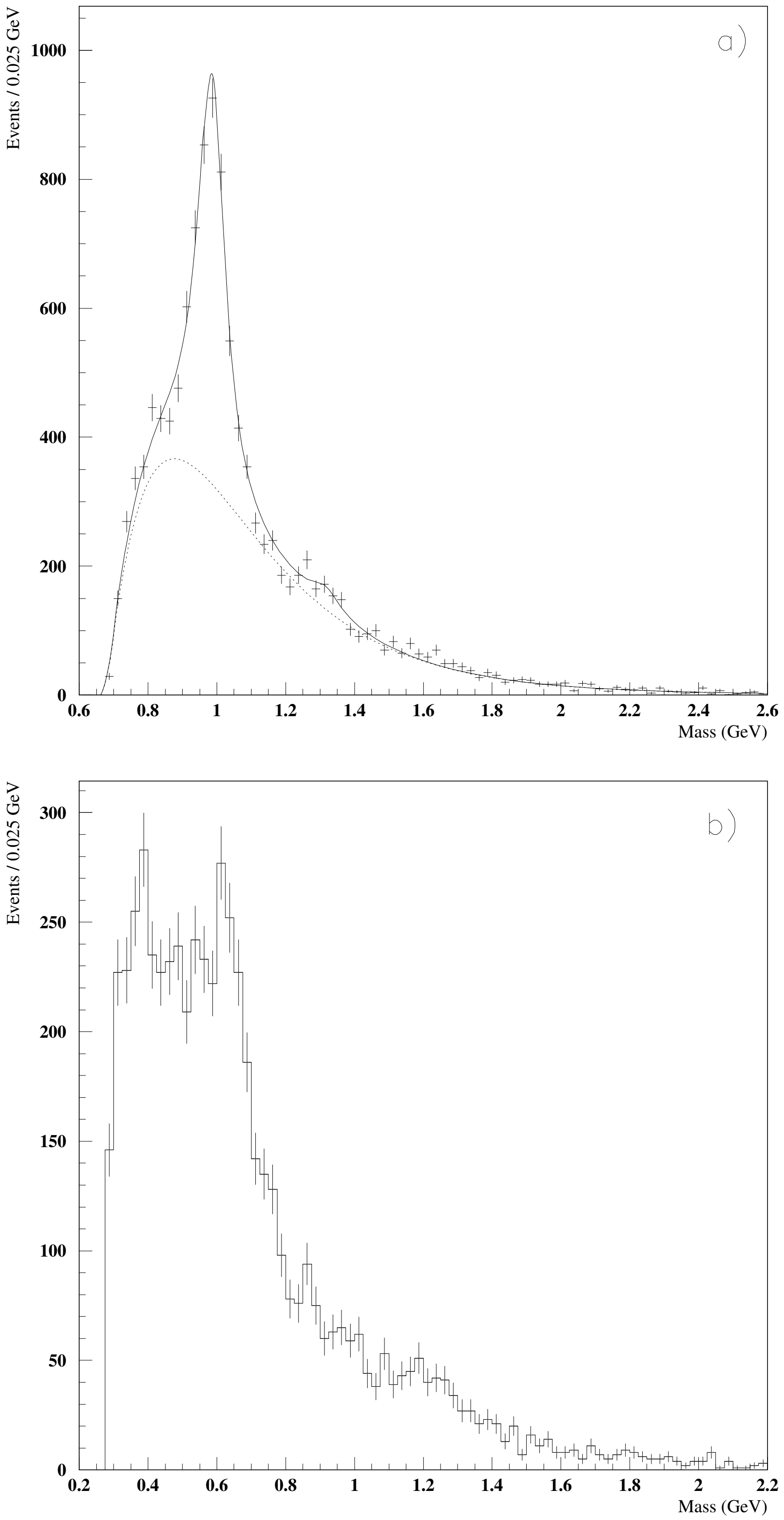

Figure 6.16: The a) $\eta\pi^{\pm}$ and b) $\pi^{+}\pi^{-}$ mass spectra from $\eta\pi^{+}\pi^{-}$. The fit is described in the text.

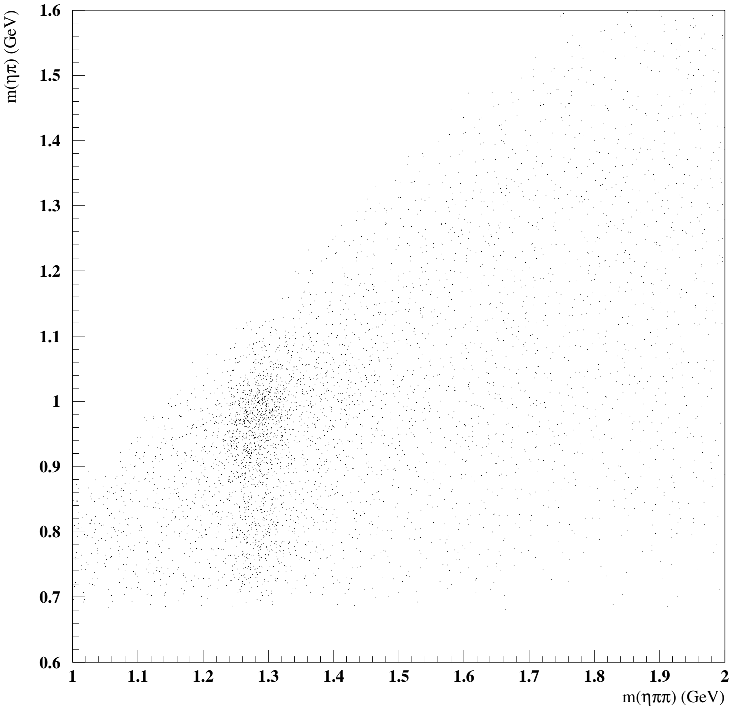

Figure 6.17: Scatter plot of m($\eta\pi^{\pm}$) vs. m($\eta\pi^{+}\pi^{-}$).

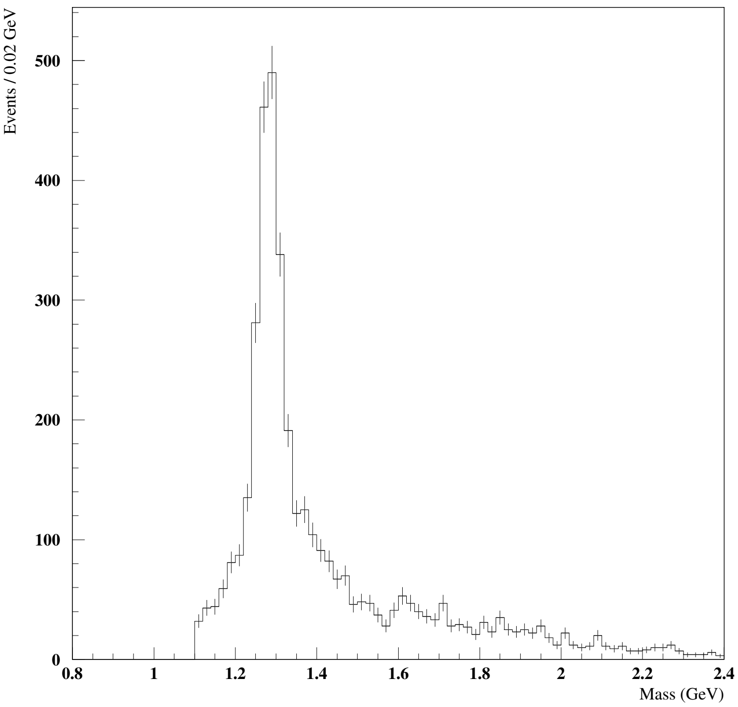

Figure 6.18: The $\delta/\mathrm{a}_0(980)\pi$ effective mass distribution.

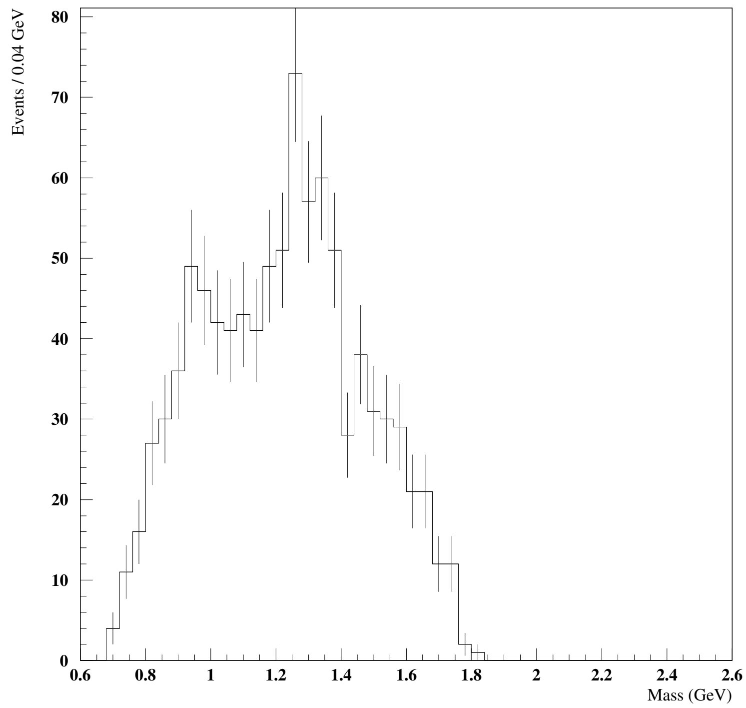

Figure 6.19: The $\eta\pi^{\pm}$ effective mass distribution for the X(1900) region.

charged tracks are traced through the apparatus to see if they would have been accepted. The decay photons are traced to OLGA and checked if they would have been accepted. The acceptance is then the number of accepted events divided by the total generated. The acceptance as a function of $\eta\pi^+\pi^-$ effective mass is shown in Fig 6.20 for the $\gamma\gamma$ and $\pi^+\pi^-\pi^0$ decay modes of the η. The acceptance varies only slightly over the mass range considered, and so no correction is needed to be applied to the $\eta\pi\pi$ mass spectrum.

6.7 Study of the t Dependence

If we assume that the observed resonances are produced by the double exchange graph as shown in Fig 6.21, the mass spectrum has been split into two samples, one with $\mathrm{t} < 0.3\,\mathrm{GeV}^2$ and the other with $\mathrm{t} > 0.3\,\mathrm{GeV}^2$, where t is the total 4-momentum transferred at the fast and slow vertices (i.e. $\mathrm{t} = \mathrm{t}_1 + \mathrm{t}_2$). This is shown in Fig 6.22. Figs 6.22a,b show $\mathrm{t} < 0.3$ and $\mathrm{t} > 0.3\,\mathrm{GeV}^2$ respectively for the complete data. Fig 6.22c shows the mass spectrum for $\mathrm{t} < 0.3\,\mathrm{GeV}^2$ and $\chi^2 \leq 1.0$. This has

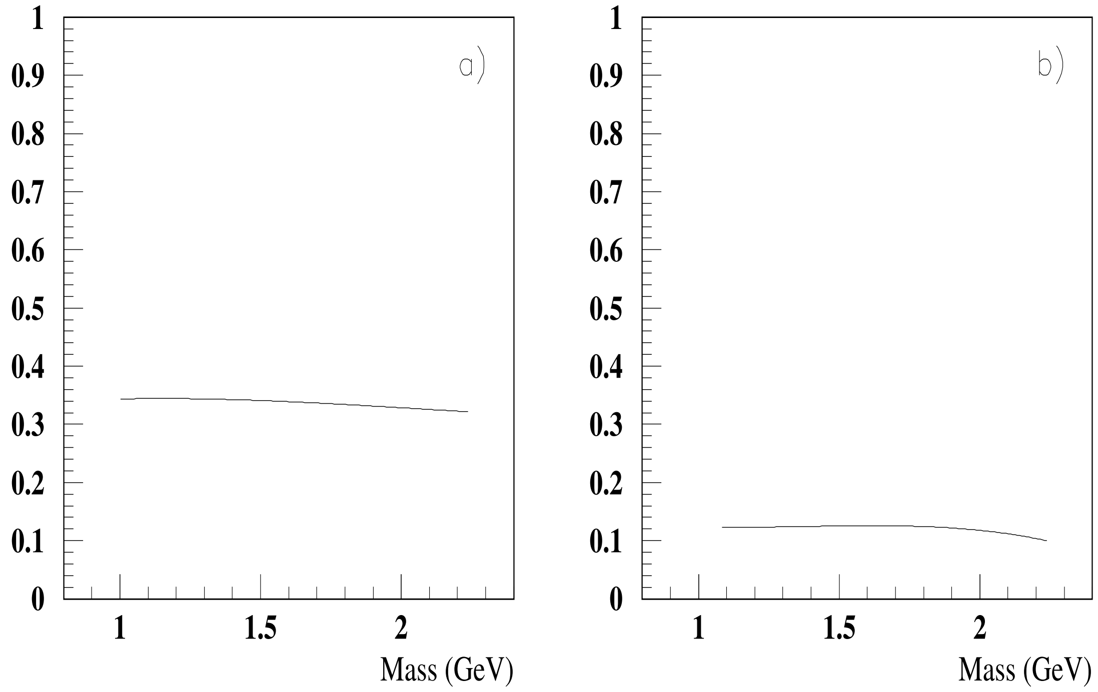

Figure 6.20: The $\eta\pi^+\pi^-$ acceptance for a) $\eta \to \gamma\gamma$ and b) $\eta \to \pi^+\pi^-\pi^0$.

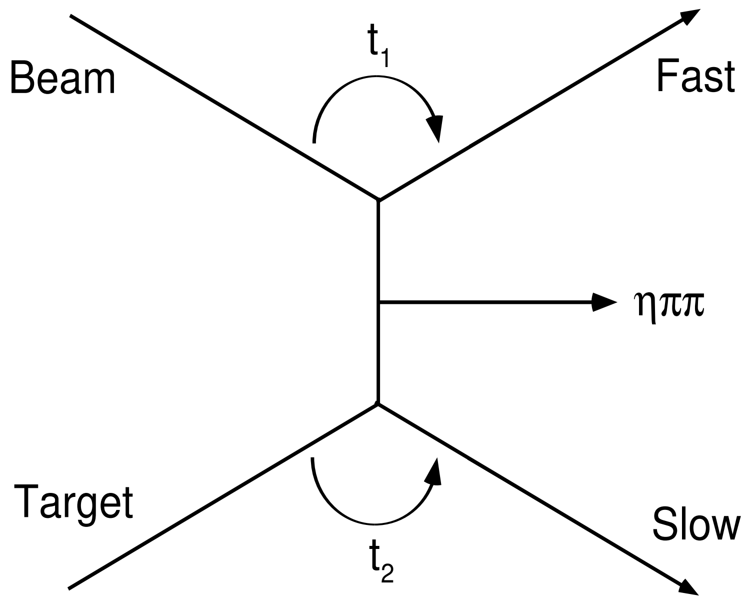

Figure 6.21: The double exchange graph for the centrally produced $\eta\pi\pi$ system.

been fitted using the $\eta'(958)$, $f_1(1285)$and the X(1900), using the parameters found from the fit to the whole data with $\chi^2 \leq 1.0$. Fig 6.22d shows the mass spectrum for t $> 0.3\,\mathrm{GeV}^2$ and $\chi^2 > 1.0$. This has been fitted using the $\eta'(958)$and $f_1(1285)$ only. These plots show that the X(1900) is predominately produced at low t, as was found for the 4π channel, and is consistent with the X(1900) being produced by a DPE mechanism. The plots also show a depletion of the $\eta'(958)$ signal in the low t region, which is consistent with what is found in the 300 GeV/c data [29].

6.8 Spin parity analysis

In order to establish the nature and decay mode of the $f_1(1285)$, and to search for other resonances, a mass dependent spin parity analysis has been performed on the $\eta\pi^+\pi^-$ system using the Zemach tensor formalism (see appendix B for an overview of this method). The intermediate states considered are $\delta/a_0(980)\pi$, $\epsilon/f_0(1400)\eta$ and $\rho(770)\eta$, using waves up to spin 2. The analysis was performed up to a $\eta\pi\pi$ mass of 1.6 GeV. The $\delta/a_0(980)$ and $\rho(770)$ are parameterised by relativistic Breit-Wigners, while the $\epsilon/f_0(1400)$ is parameterised as a $\pi\pi$ phase shift [40]. Interference is allowed between waves having the same spin and parity. The tensors used are given in Table 6.3 (see appendix B for an explanation of how these tensors are formed). The data have been fitted using the maximum likelihood method dividing the data into 40 MeV slices as a function of the $\eta\pi\pi$ effective mass. Table 6.4 shows the $\Sigma\,\ln$(likelihood) for the $f_1(1285)$ region ($1.20 < m(\eta\pi\pi) < 1.36\,\mathrm{GeV}$) for each of the waves considered. It can be seen that the dominant wave is the $J^{PC} = 1^{++}\,\delta/a_0(980)\pi$. The other waves were then added to the $1^{++}\,\delta\pi$ wave one at a time, but the logarithmic likelihood of the fit does not improve significantly over the region considered on adding any of the waves. Fig 6.23 shows the results of the fit on adding one such wave, the $J^{PC} = 0^{-+}\,\delta\pi$, to the $1^{++}\,\delta\pi$. The curve superimposed on the $1^{++}\,\delta\pi$ wave is the $f_1(1285)$ signal from the fit to the $\eta\pi^+\pi^-$ mass spectrum, and describes this wave well in size and shape. Fig 6.24 shows the same fit but to events with $\chi^2 \leq 1.0$. Again the $f_1(1285)$ signal from the mass

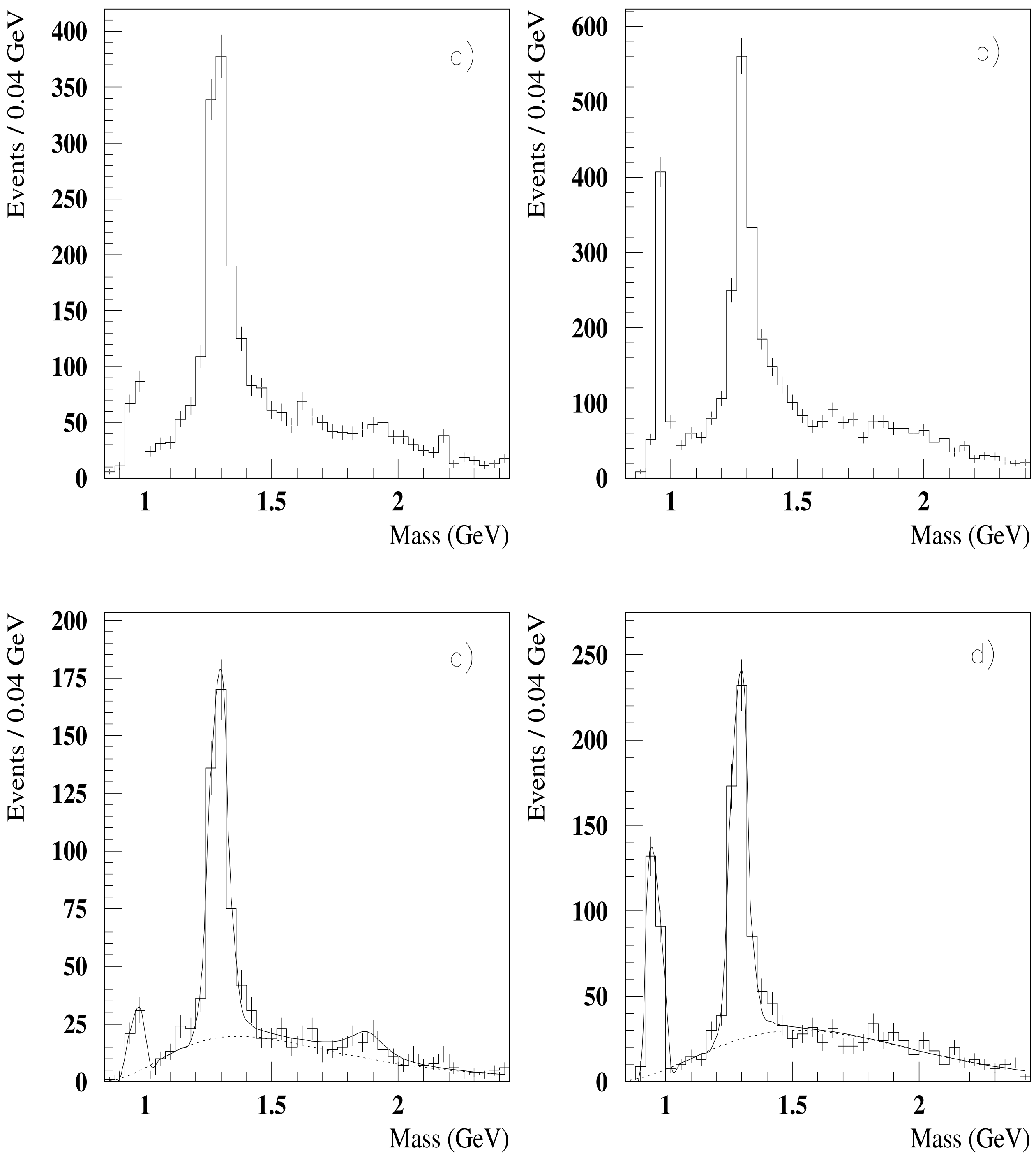

Figure 6.22: The $\eta\pi^+\pi^-$ mass spectrum for the whole data with a) t $<$ 0.3 and b) t $>$ $0.3\,\mathrm{GeV}^2$, and for events with $\chi^2 \leq 1.0$ with c) t $<$ 0.3 and d) t $>$ $0.3\,\mathrm{GeV}^2$. The fits are described in the text.

$\mathbf{J^P}$	**S**	**L**	**Decay Modes**	**Amplitudes**
0^-	0	0	$\delta\pi$	$\mathrm{BW}(\delta^+_{12}) + \mathrm{BW}(\delta^-_{13})$
1^+	0	1	$\delta\pi$	$\mathrm{BW}(\delta^+_{12})\mathbf{p_3} + \mathrm{BW}(\delta^-_{13})\mathbf{p_2}$
2^-	0	2	$\delta\pi$	$\mathrm{BW}(\delta^+_{12})[\mathbf{p_3}^\mathrm{i}\mathbf{p_3}^\mathrm{j} - \frac{1}{3} \mid \mathbf{p_3} \mid^2 \delta^\mathrm{ij}] + \mathrm{BW}(\delta^-_{13})[\mathbf{p_2}^\mathrm{i}\mathbf{p_2}^\mathrm{j} - \frac{1}{3} \mid \mathbf{p_2} \mid^2 \delta^\mathrm{ij}]$
0^-	0	0	$\eta\epsilon$	$\mathrm{BW}(\epsilon_{23})$
1^+	0	1	$\eta\epsilon$	$\mathrm{BW}(\epsilon_{23})\mathbf{p_1}$
2^-	0	2	$\eta\epsilon$	$\mathrm{BW}(\epsilon_{23})[\mathbf{p_1}^\mathrm{i}\mathbf{p_1}^\mathrm{j} - \frac{1}{3} \mid \mathbf{p_1} \mid^2 \delta^\mathrm{ij}]$
1^+	1	0	$\eta\rho$	$\mathrm{BW}(\rho^0_{23})\mathbf{t_1}$
0^-	1	1	$\eta\rho$	$\mathrm{BW}(\rho^0_{23})\mathbf{t_1}.\mathbf{p_1}$
1^-	1	1	$\eta\rho$	$\mathrm{BW}(\rho^0_{23})\mathbf{t_1} \times \mathbf{p_1}$
2^-	1	1	$\eta\rho$	$\mathrm{BW}(\rho^0_{23})[\frac{1}{2}(\mathbf{t_1}^\mathrm{i}\mathbf{p_1}^\mathrm{j} + \mathbf{p_1}^\mathrm{i}\mathbf{t_1}^\mathrm{j}) - \frac{1}{3}(\mathbf{t_1}.\mathbf{p_1})\delta^\mathrm{ij}]$
1^+	1	2	$\eta\rho$	$\mathrm{BW}(\rho^0_{23})[\mathbf{p_1}(\mathbf{t_1}.\mathbf{p_1}) - \frac{1}{3}(\mathbf{p_1}.\mathbf{p_1})\mathbf{t_1}]$
2^+	1	2	$\eta\rho$	$\mathrm{BW}(\rho^0_{23})(\frac{1}{2}[(\mathbf{t_1} \times \mathbf{p_1})^\mathrm{i}\mathbf{p_1}^\mathrm{j} + \mathbf{p_1}^\mathrm{i}(\mathbf{t_1} \times \mathbf{p_1})^\mathrm{j}] - \frac{1}{3}[(\mathbf{t_1} \times \mathbf{p_1}).\mathbf{p_1}]\delta^\mathrm{ij})$

Table 6.3: Decay amplitudes for the ${\eta_1}{\pi^+}_2{\pi^-}_3$ spin parity analysis.

Wave	Σ ln(likelihood)	% wave
$0^-\ \delta\pi$	-328.6	67.9
$1^+\ \delta\pi$	-494.9	82.7
$2^-\ \delta\pi$	-106.5	57.5
$0^-\ \eta\epsilon$	0	0
$1^+\ \eta\epsilon$	0	0
$2^-\ \eta\epsilon$	-6.5	12.7
1^+S $\eta\rho$	0	0
$0^-\ \eta\rho$	-0.6	1.3
$1^-\ \eta\rho$	0	0
$2^-\ \eta\rho$	0	0
1^+D $\eta\rho$	0	0
$2^+\ \eta\rho$	0	0

Table 6.4: The negative log likelihoods for the $\mathrm{f}_1(1285)$ region of the $\eta\pi\pi$ mass spectrum for all the considered waves.

spectrum fit describes the 1^{++} $\delta\pi$ well, and there is no evidence for any 1^{++} state at 1420 MeV, nor evidence for any pseudoscalar states being produced. Fig 6.25 shows the Dalitz plots for the $f_1(1285)$ region ($1.20 < m(\eta\pi\pi) < 1.36$ GeV) of the $\eta\pi^+\pi^-$ channel. Also shown are Monte Carlo simulations for pure $J^{PC} = 0^{-+}$ $\delta\pi$ and pure $J^{PC} = 1^{++}$ $\delta\pi$ waves, where the Zemach amplitudes have been used to represent these waves. The fit to the Dalitz plot gives the best solution as $85\pm5\%$ 1^{++} $\delta\pi$ with 15% phase space background. A Monte Carlo simulation was performed using these values and the results have been superimposed onto the Dalitz plot projections in Fig 6.26 and show good agreement, confirming that the $f_1(1285)$ is being observed. The acceptance over the Dalitz plot was evaluated and was found to be flat, and indeed fits to the acceptance corrected data do not differ significantly from those found above.

The method was repeated for the X(1900) region, including in addition to the waves mentioned previously the 2^{-+} $a_2(1320)\pi$, 1^{++} $a_2(1320)\pi$ and the 2^{++} $a_2(1320)\pi$. However due to the lack of statistics in this region no conclusions about the spin and parity of this state can be drawn.

6.9 Conclusions

The $\eta\pi^+\pi^-$ channel from the reaction $pp \rightarrow p_f(\pi^+\pi^-\eta)p_s$ at 450 GeV/c incident momentum has been studied and shows clear $\eta'(958)$ and $f_1(1285)$ signals with masses and widths

$$\begin{aligned} m_{\eta'(958)} &= 957 \pm 1\ MeV \\ \sigma_{\eta'(958)} &= 16 \pm 1\ MeV \\ m_{f_1(1285)} &= 1285 \pm 1\ MeV \end{aligned}$$

The $f_1(1285)$ is found to be a $J^{PC} = 1^{++}$ state decaying via $\delta/a_0(980)\pi$. In addition there is a structure in the 1900 MeV region with parameters

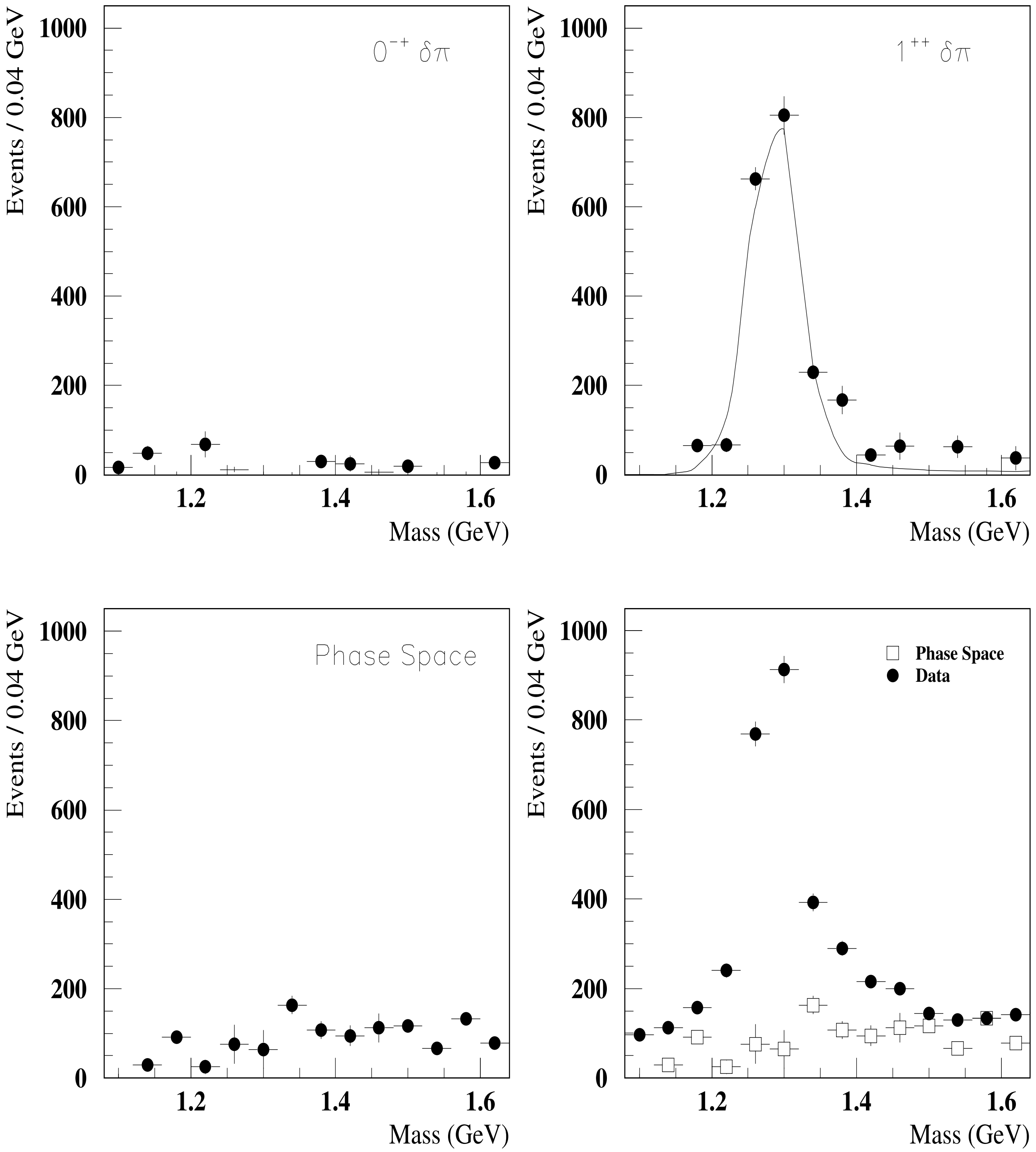

Figure 6.23: Results of the Zemach tensor spin parity analysis.

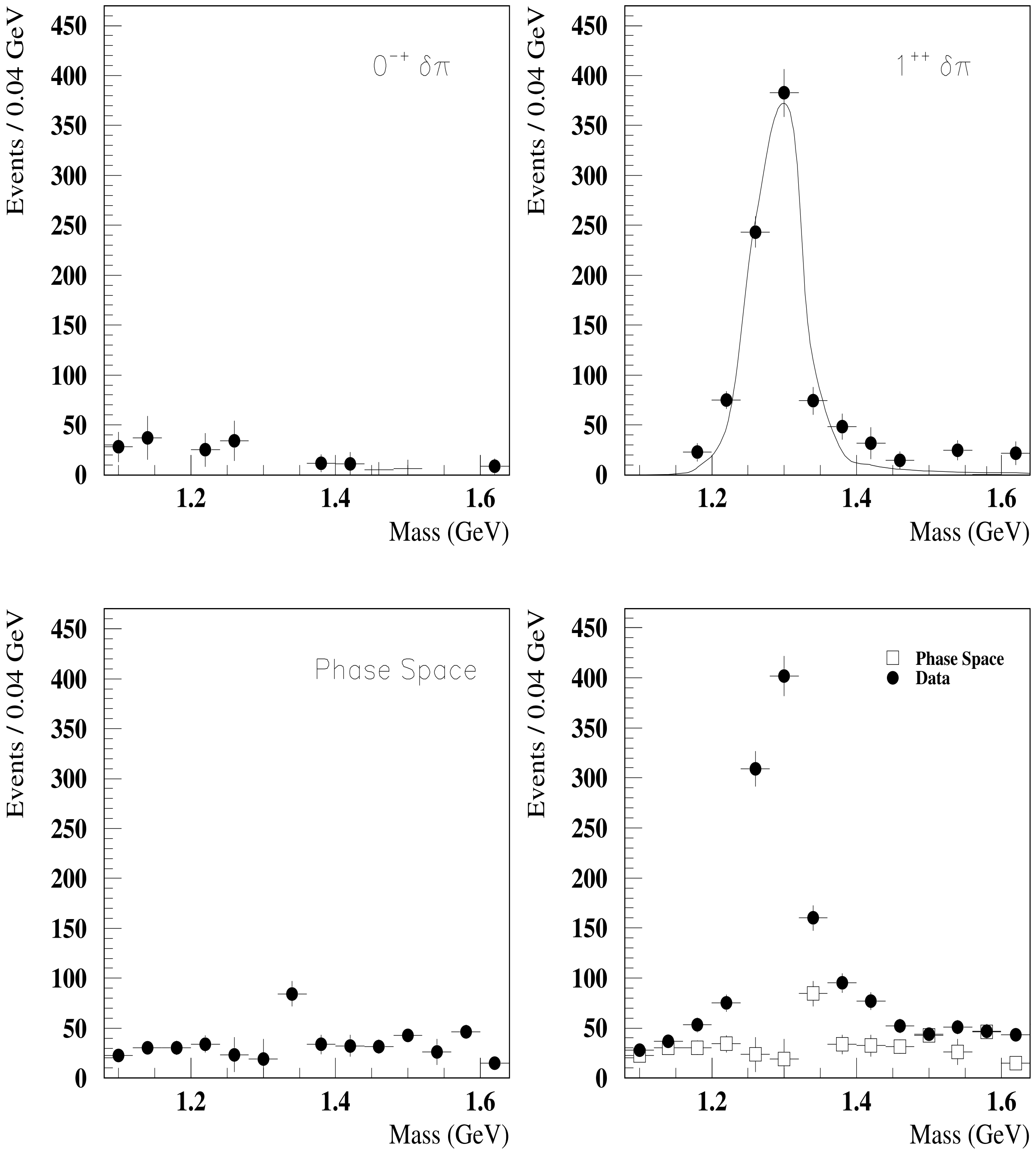

Figure 6.24: Results of the Zemach tensor spin parity analysis for events with $\chi^2 \leq 1.0$.

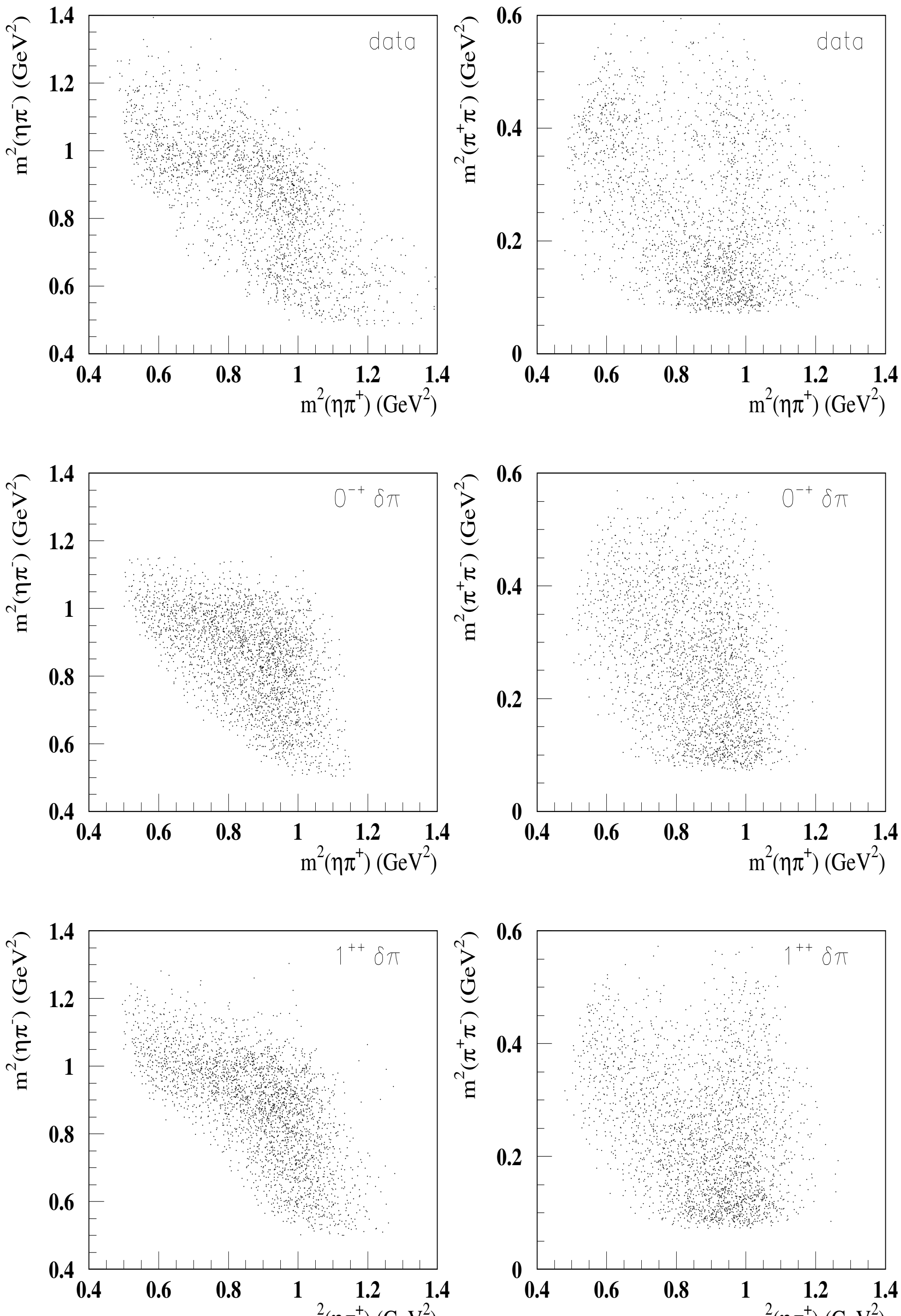

Figure 6.25: Dalitz plots for the $\eta\pi\pi$ channel, along with Monte Carlo simulations for pure 1^{++} and 0^{-+} $\delta\pi$ waves.

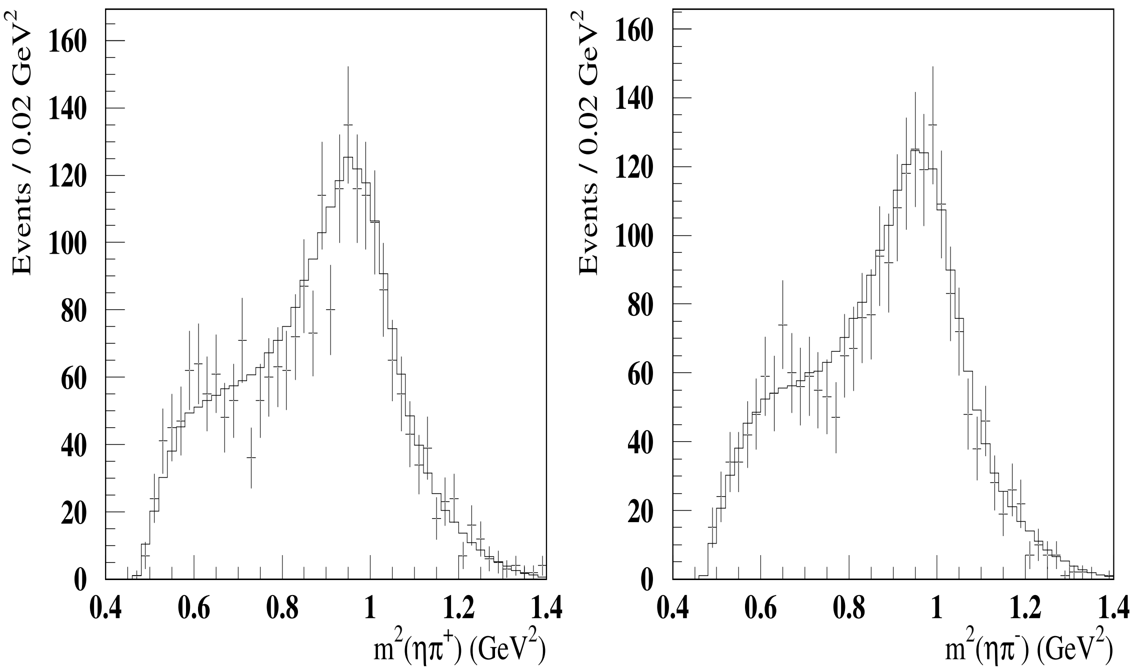

Figure 6.26: The $\eta\pi\pi$ Dalitz plot projections. The superimposed curves correspond to a Monte Carlo simulation using 85% 1^{++} $\delta\pi$ wave.

$$\begin{aligned} m_{\mathrm{X}(1900)} &= 1882 \pm 24\ MeV \\ \Gamma_{\mathrm{X}(1900)} &= 172 \pm 46\ MeV \end{aligned}$$

which appears to decay via $\mathrm{a}_2(1320)\pi$, and is probably due to the X(1900) observed in the 4π channel. There is no evidence for a $\eta\pi^+\pi^-$ decay mode of the $\mathrm{E/f_1}(1420)$, nor for the production of any pseudoscalar states, in particular the states at 1400 and 1490 MeV observed for example in radiative J/ψ decay to $\eta\pi^+\pi^-$ [25, 26] and $\mathrm{K^0_S K^\pm}\pi^\mp$ [26], and in π^-p interactions to $\eta\pi^+\pi^-$ [23] and $\mathrm{K^0_S K^0_S}\pi^0$ [22].

Chapter 7

The $\pi^+\pi^-\pi^0$ channel in WA91

7.1 Introduction

The $\pi^+\pi^-\pi^0$ channel has been studied quite extensively over the years, in an attempt to resolve the question of the existence and parameters of the $a_1(1260)$, believed to be the isovector member of the lowest lying $J^{PC} = 1^{++}$ nonet. The difficulty has been that in hadronic π^-p interactions to $\rho\pi$ the presence of a Deck background [41] makes the extraction of the $a_1(1260)$ parameters difficult, so much so that for many years it was believed to be just a threshold effect and not a resonance at all. Its existence was effectively proved by high statistics experiments on diffractive [42] and charge exchange [43] π^-p interactions producing a $\pi^+\pi^-\pi^0$ final state, where both a resonance and a Deck background were required to explain the $1^+S(\rho\pi)$ amplitude.

However the masses and widths for the $a_1(1260)$ as found by different experiments have not been in total agreement. Whereas the above experiments found an a_1 mass of 1275 $\pm$ 28 MeV and a width of 316 $\pm$ 45 MeV, experiments studying $\tau \to \rho\pi\nu$ [44, 45, 46], which is free from the Deck effect, found different parameters, with $m(a_1) \approx 1100$ MeV and $\Gamma(a_1) \approx 490$ MeV. Independent reanalysis of this data gave parameters consistent with the π^-p data [47, 48]. On the other hand, study of the backward produced 3π system in the reaction $K^-p \to \Sigma^-\pi^+\pi^-\pi^+$ [49], which is also free of the Deck effect, found a 1^{++} state with m = 1041 $\pm$ 13 MeV and Γ = 230 $\pm$ 50 MeV. In the centrally produced $\pi^+\pi^-\pi^0$ system from hadronic interactions, an analysis of the $1^{++}S$ $\rho\pi$ wave found $m(a_1) = 1208 \pm 15$ MeV and $\Gamma(a_1) = 430 \pm 50$ MeV [50].

This chapter describes an analysis of the $\pi^+\pi^-\pi^0$ channel formed in the experiment WA91 at 450 GeV.

7.2 Selection of the reaction $pp \to p_f(\pi^+\pi^-\pi^0)p_s$

The reaction

$$pp \to p_f(\pi^+\pi^-\pi^0)p_s \tag{7.1}$$

has been selected from the sample of events having four outgoing tracks and two reconstructed γ's in OLGA, each with energy greater than 0.5 GeV. Showers associated with charged tracks were removed, and events with out of time γ's rejected, as explained in chapter 5. The maximum number of blocks allowed to be in a photon shower was four. Momentum balanced events were then selected by imposing the following cuts on the components of missing momentum,

$$\begin{aligned} |\text{missing } p_x| &< 20.0 \text{ GeV/c} \\ |\text{missing } p_y| &< 0.20 \text{ GeV/c} \\ |\text{missing } p_z| &< 0.16 \text{ GeV/c} \end{aligned}$$

The $\gamma\gamma$ mass spectrum following these cuts is shown in Fig 7.1a. To enhance the π^0 signal over the background the following extra cuts were made on the photon energies depending on ORC type (see appendix C) :-

Itype	Energy cut (GeV)
14 - 16	0.7
17	0.7
18	1.0
20	1.4
40	2.0

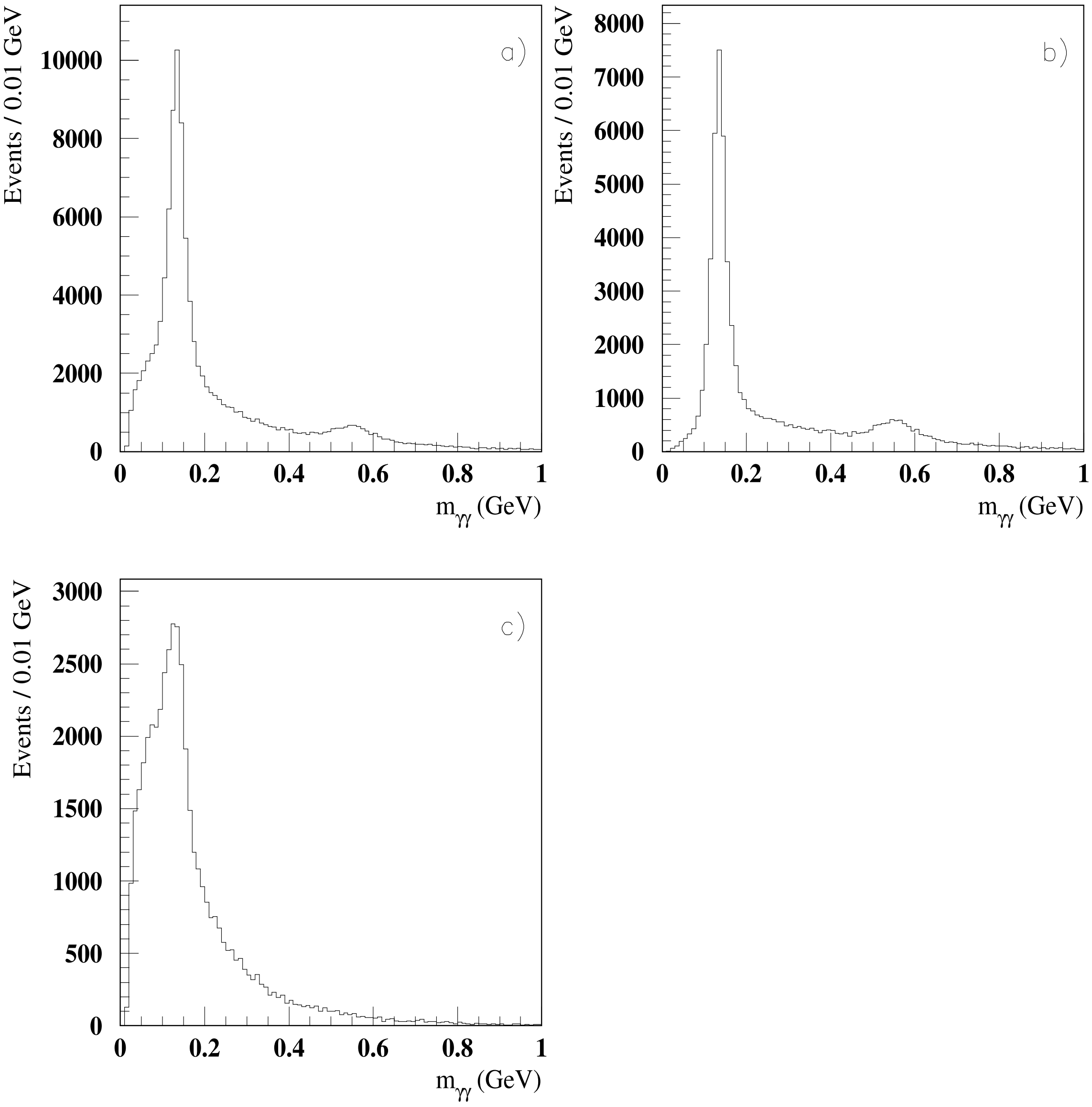

Figure 7.1: $\gamma\gamma$ spectrum after the a) initial cuts and b) secondary cuts. c) The $\gamma\gamma$ signal rejected by the secondary cuts.

and the following cuts on the minimum photon distance from the centre of OLGA :-

Itype	Minimum distance from OLGA centre (cm)
17	19.0
18	20.0
20	19.0

as explained in section 5.4. The $\gamma\gamma$ mass spectrum after these cuts is shown in Fig 7.1b, while the rejected signal is shown in Fig 7.1c, showing that that background is reduced but that only a little π^0 signal is thrown away.

Reaction 7.1 was then selected by requiring $0.10 < m(\gamma\gamma) < 0.17$ GeV. The γ momenta and energies were then recalculated to give the π^0 mass, using method three as explained in section 6.2.1. Energy balance was ensured by calculating the function Δ for each event, where

$$\Delta = \mathrm{MM}^2(\mathrm{p_f p_s}) - \mathrm{M}^2(\pi^+\pi^-\pi^0)$$

where MM^2 is the missing mass squared of the proton proton system, and M^2 is the mass squared of the 3 pion system, assuming the charged tracks to be all pions. Events with $|\Delta| < 3.0$ GeV^2 were then accepted to obtain the $\pi^+\pi^-\pi^0$ channel.

The centre of mass rapidities of the π^0, $\pi^+$and π^- are shown in Fig 7.2, where an accumulation of events near the fast proton rapidity can be seen for the π^+ and π^-. Fig 7.3 shows the $\mathrm{p_f}\pi^+$ and $\mathrm{p_f}\pi^-$ effective mass distributions, where a clear Δ^{++} signal, and a threshold enhancement at the Δ^0 mass can be seen for the π^+ and π^- respectively. A rapidity cut of $\mathrm{y} < 2.0$ on the π^+ and π^- removes these diffractive signals, as shown by the cross hatched sections of Fig 7.3. The absence of any Δ^+ signal is due to the fact that at least one of the photons from the decay of the fast π^0 passes through the central hole of OLGA, making the π^0 impossible to reconstruct.

Fig 7.4 shows the $\pi^-\pi^0$ effective mass spectrum for those events with $\mathrm{y}_{\pi^+} > 2.0$,

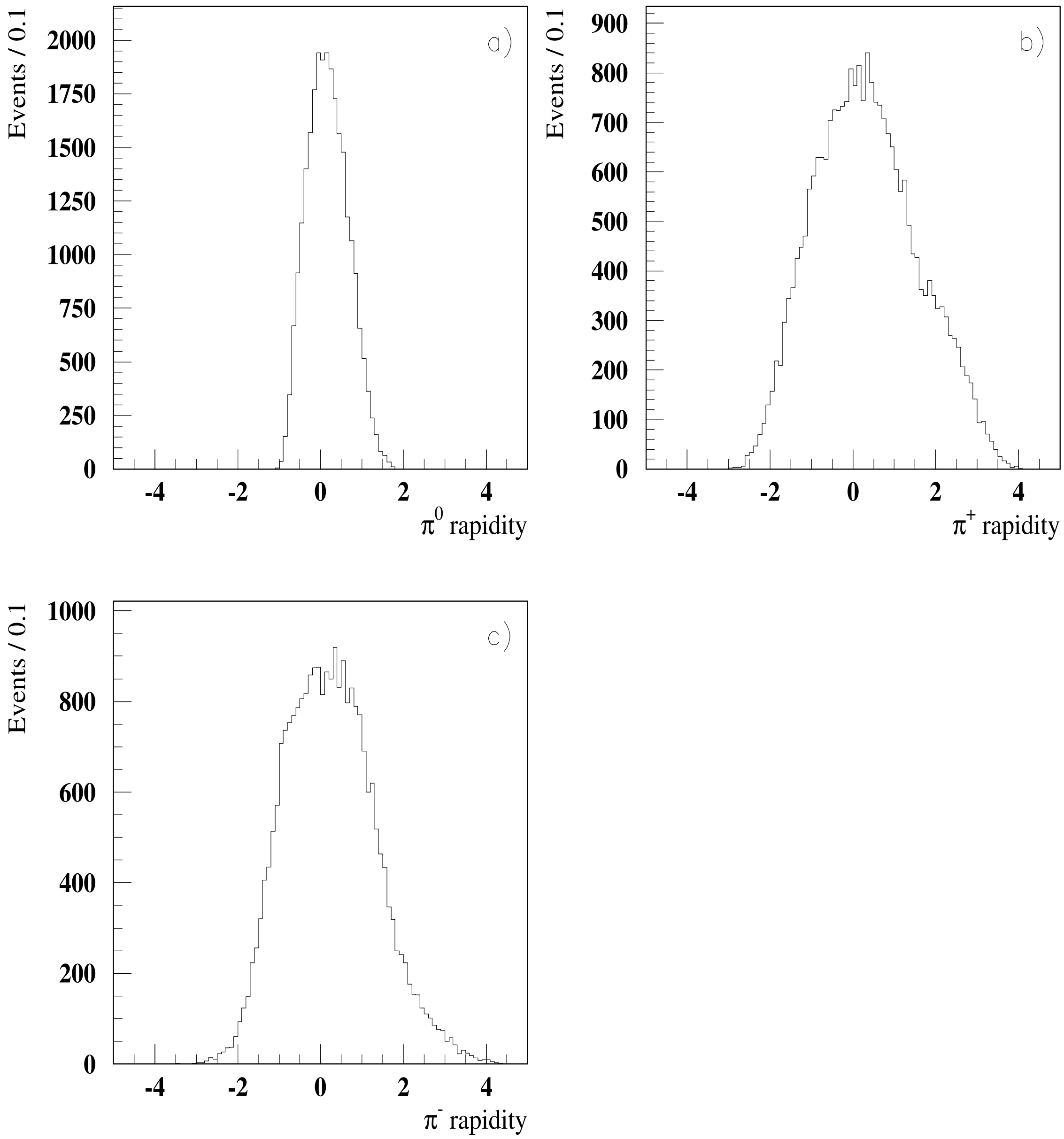

Figure 7.2: a) π^0 b) π^+ and c) π^- rapidities.

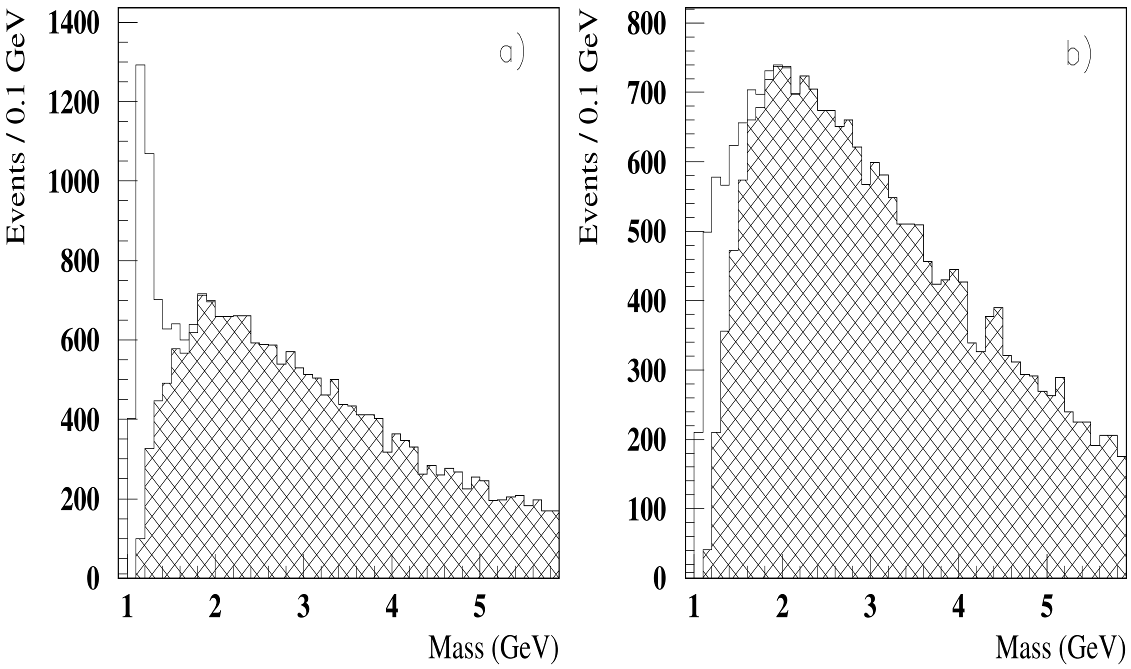

Figure 7.3: a) $p_f\pi^+$ and b) $p_f\pi^-$ mass spectra. The cross-hatched sections are for rapidity cuts explained in the text.

i.e. corresponding to the events with a diffractive Δ^{++}. A clear $\rho(770)$ signal can be seen, indicating the presence of a $\Delta^{++}\rho^-$ channel.

Fig 7.5 shows the Feynman x_F distributions for the fast proton, slow proton and for the $\pi^+\pi^-\pi^0$ system. The central system is clearly separated from the fast and slow protons. The mass spectrum for $\pi^+\pi^-\pi^0$ events passing all these cuts is shown in Fig 7.6 (21299 events). There are clear peaks at the $\eta(548)$ and the $\omega(783)$ masses, and some evidence for the $a_2(1320)$. This will be discussed in more detail in the following sections.

7.3 The $\pi^+\pi^-\pi^0$ mass spectrum

The $\pi^+\pi^-\pi^0$ mass spectrum has been fitted using a Gaussian to describe the η and a Breit-Wigner convoluted with a Gaussian to describe the ω with the Breit-Wigner width fixed to the Particle Data Book [38] value of 8.5 MeV and the Gaussian width free to represent the experimental resolution. A relativistic spin 2 Breit-Wigner was used to describe the $a_2(1320)$, with a free mass but a width fixed to the Particle Data Book value of 110 MeV. The $a_1(1260)$ is described using a Breit-Wigner of the

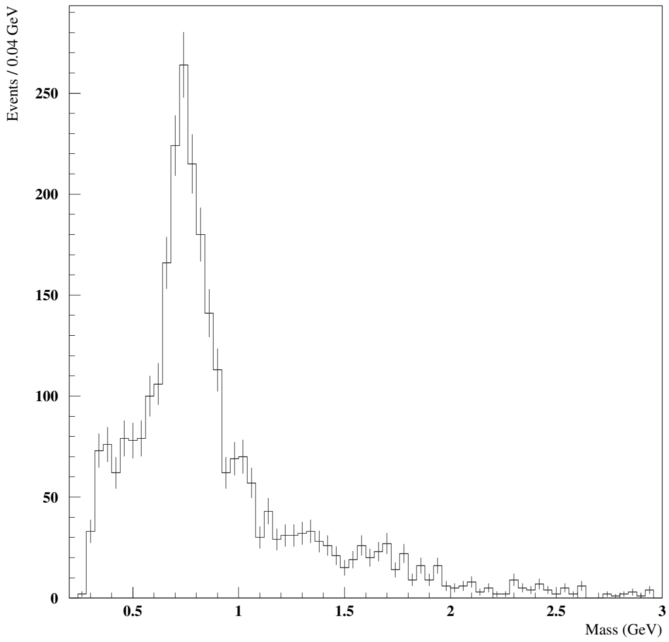

Figure 7.4: The $\pi^-\pi^0$ effective mass distribution for $y_{\pi^+} > 2.0$.

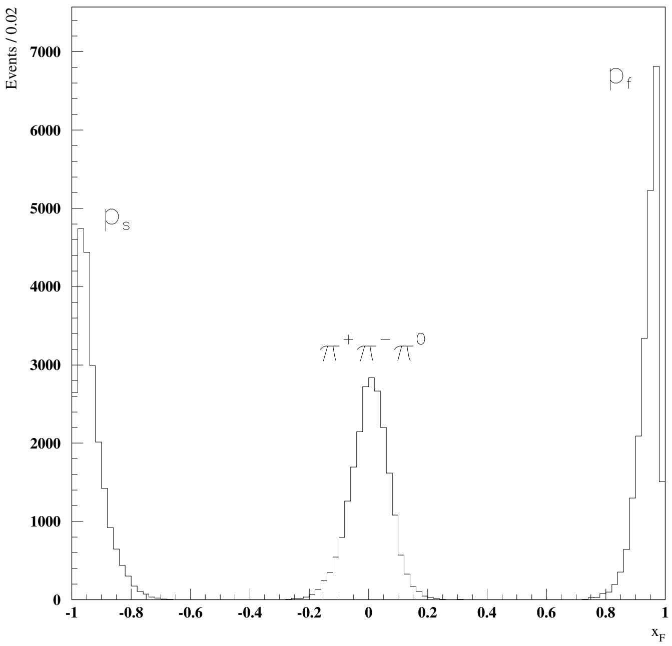

Figure 7.5: The Feynman x_F distributions for the slow proton, the $\pi^+\pi^-\pi^0$ system and the fast proton.

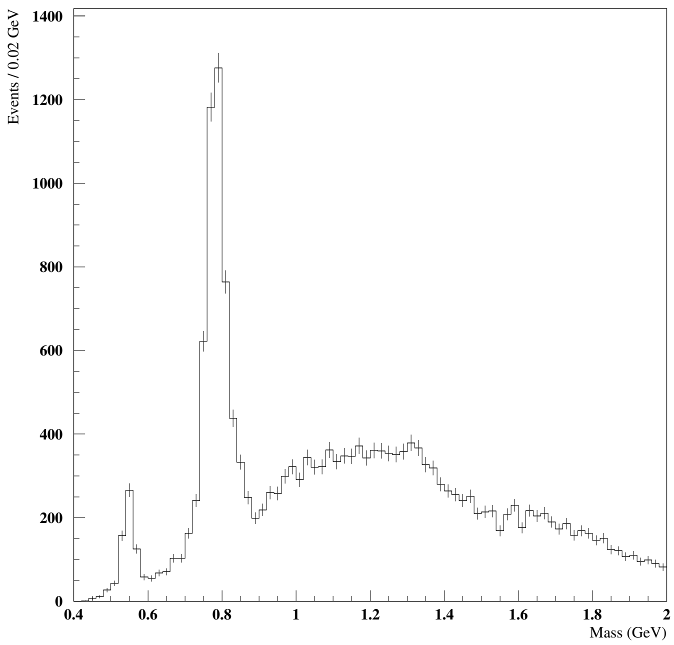

Figure 7.6: The $\pi^+\pi^-\pi^0$ mass spectrum.

form

$$\frac{dN}{dm} = \frac{m_{a_1}\Gamma_{a_1}(m)}{(m^2 - m_{a_1}^2)^2 + \Gamma_{a_1}^2(m)\, m_{a_1}^2}$$

where $\Gamma_{\mathrm{a_1}}(\mathrm{m})$ is a mass dependent width of the form

$$\Gamma_{a_1}(m) = \Gamma_{a_1}(m_{a_1})\, \frac{\rho^{1^+S}(m)}{\rho^{1^+S}(m_{a_1})}$$

where $\rho^{1^+\mathrm{S}}(\mathrm{m})$ is the phase space for S-wave $\rho^{\pm}(770)\pi^{\mp}$ which includes the effects of the mass dependent $\rho^{\pm}(770)$ width and of interference between the two $\rho^{\pm}(770)$ bands in the Dalitz plot [47]. A background has been used of the form

$$Bgnd(m) \;=\; (m - m_{th})^{\alpha} exp(-\beta m - \gamma m^2)$$

where m is the $\pi^+\pi^-\pi^0$ mass, $\mathrm{m_{th}}$ is the $\pi^+\pi^-\pi^0$ threshold mass and α, β, γ are fit parameters. The results of the fit are

$$\begin{aligned}
m\eta &= 543 \;\pm\; 1\; MeV \\
\sigma\eta &= 16 \;\pm\; 1\; MeV \\
m_{\omega(783)} &= 781 \;\pm\; 1\; MeV \\
\sigma_{\omega(783)} &= 23 \;\pm\; 1\; MeV \\
m_{\mathrm{a_1}(1260)} &= 1162 \;\pm\; 11\; MeV
\end{aligned}$$

$$\Gamma_{a_1(1260)} = 380 \pm 35 \; MeV$$
$$m_{a_2(1320)} = 1321 \pm 7 \; MeV$$

with a χ^2/NDF of 92/65, as shown in Fig 7.7a. If the $a_1(1260)$ is removed from the fit then Fig 7.7b is produced, with a χ^2/NDF of 142/69. The mass spectrum has also been fitted for events with two class A photons (χ^2/NDF = 94/65), and for events with $\chi^2 \leq 1.0$ for the kinematically fitted π^0 (χ^2/NDF = 99/65), as shown in Fig 7.8, and gives parameters consistent within errors to those quoted above. The mass found for the $a_1(1260)$ is a little lower than the PDG average for this state [38], but due to the complicated nature of this channel the parameters are best determined from a fit to the 1^+S wave, to be described in section 7.6.

The geometrical acceptance has been calculated as explained in the previous chapter, and is shown in Fig 7.9 as a function of the $\pi^+\pi^-\pi^0$ mass. This has been used to correct the $\pi^+\pi^-\pi^0$ mass spectrum and this has also been fitted as described above, but no significant changes to the fit parameters are found.

7.4 Study of the 2 body mass spectra

In order to study the decay mechanisms of the $a_1(1260)$ and $a_2(1320)$ the $\pi^\pm\pi^0$ (2 combinations per event) and $\pi^+\pi^-$ mass spectra were plotted, having removed the η and $\omega(783)$ region ($m_{\pi^+\pi^-\pi^0} < 0.9$ GeV). This is shown in Figs 7.10 a) and b) respectively. There is a clear $\rho^\pm$ signal in the $\pi^\pm\pi^0$ mass spectrum. This has been fitted with a relativistic spin 1 Breit-Wigner (decaying to $\pi^\pm\pi^0$) together with a background of the same form as used in section 7.3. The fit gives the following parameters for the $\rho(770)$

$$m_{\rho(770)} = 766 \pm 3 \; MeV$$
$$\Gamma_{\rho(770)} = 189 \pm 9 \; MeV$$

with a χ^2/NDF of 61/43. The $\pi^+\pi^-$ mass spectrum shows evidence for ρ^0 and $f_2(1270)$ production and has been fitted with a relativistic Breit-Wigner (decaying to $\pi^+\pi^-$) to describe the ρ^0 (with mass and width fixed to those found from the

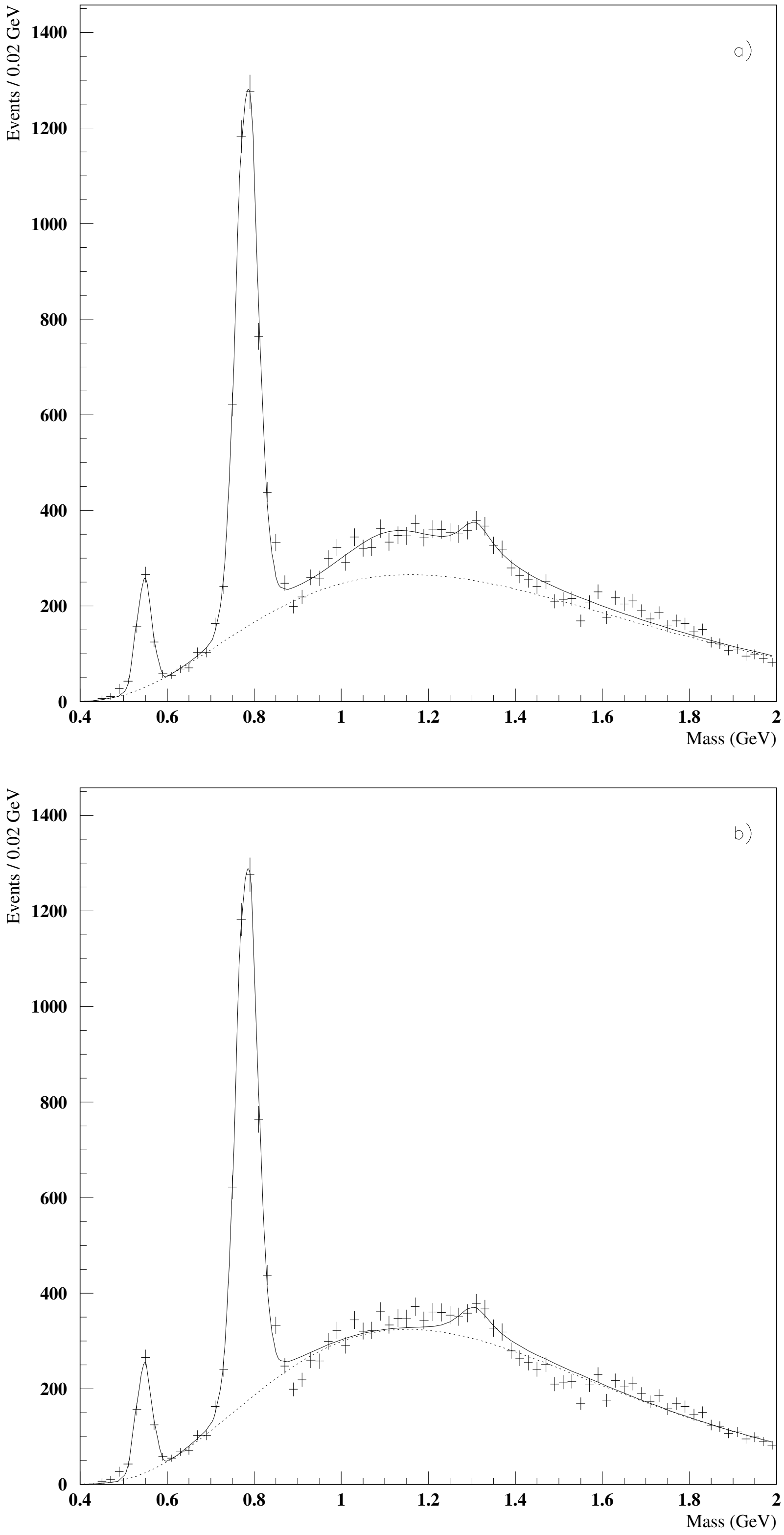

Figure 7.7: Fits to the $\pi^+\pi^-\pi^0$ mass spectrum, as described in the text.

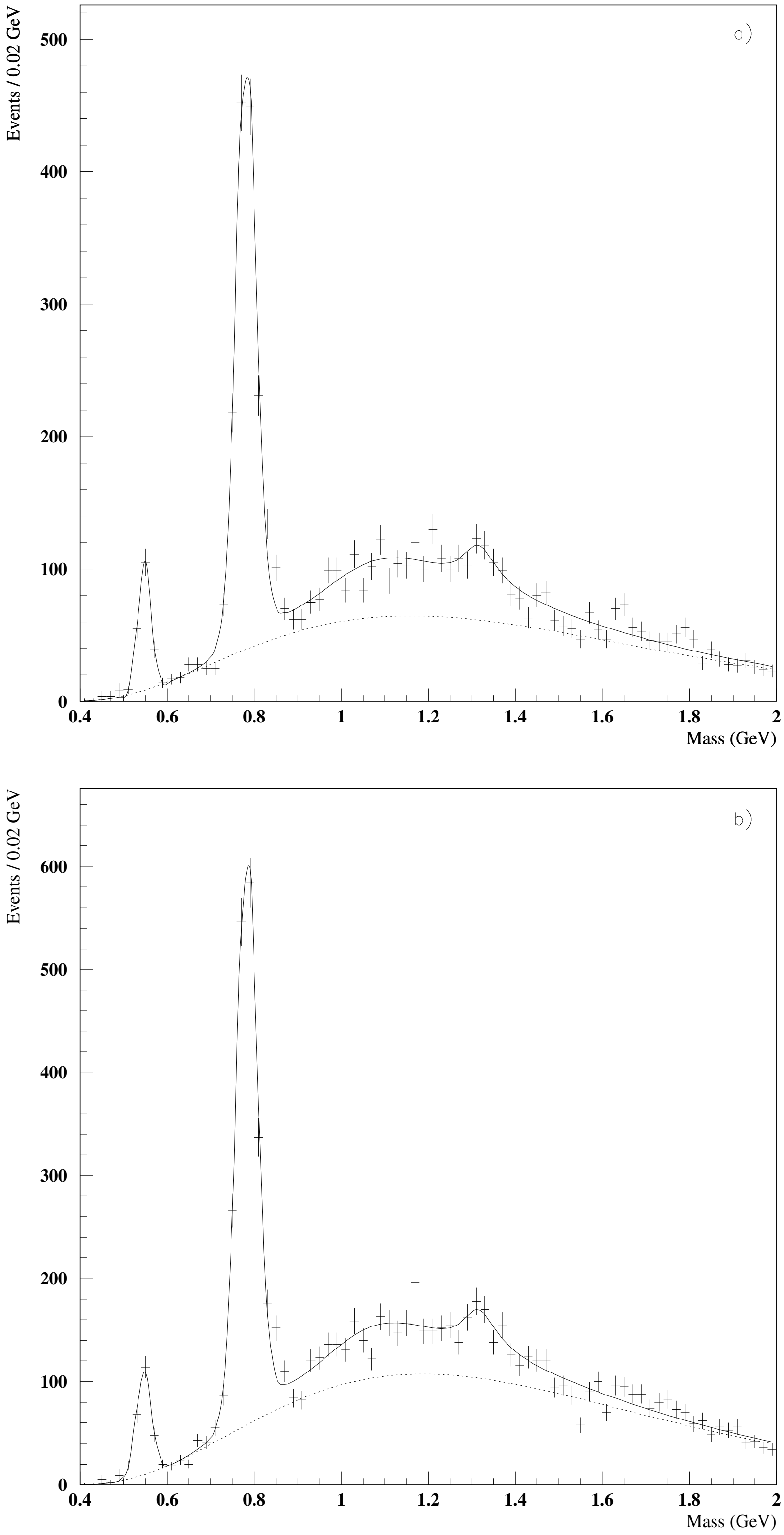

Figure 7.8: Fits to the $\pi^+\pi^-\pi^0$ mass spectrum, for events with a) class A-A photons and b) $\chi^2 \leq 1.0$.

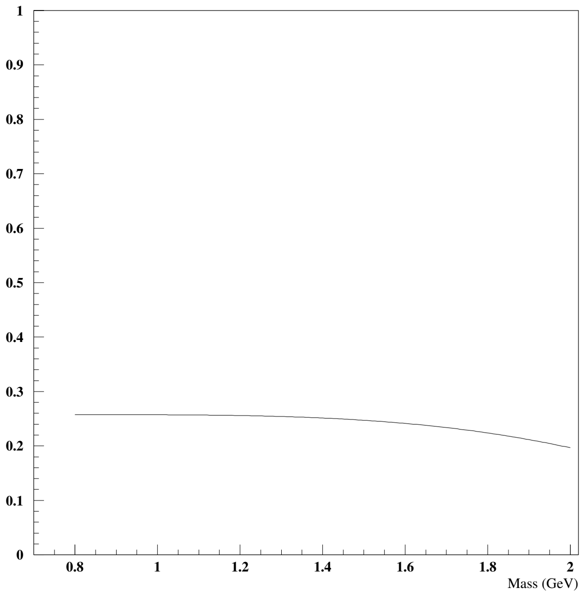

Figure 7.9: The $\pi^+\pi^-\pi^0$ acceptance.

fit to the $\pi^\pm\pi^0$ mass spectrum) and a Breit-Wigner to describe the $f_2(1270)$ (with mass and width fixed to the PDG [38] values), together with the background used in section 7.3, and gave a χ^2/NDF of 58/44. There is ~8 times more $\rho^\pm$ produced than ρ^0. This excess can be explained if we are predominately producing an isospin 1 system, as isovector states cannot decay to $\rho^0\pi^0$, as can be seen by checking the Clebsch-Gordon coefficients for combining two I=1 particles to produce an I=1, I_3=0 system.

If a cut is made on the $\rho^\pm$ ($0.68 < m_{\pi^\pm\pi^0} < 0.86$) and the subsequent $\rho^\pm\pi^\mp$mass spectrum plotted then Fig 7.11 is produced, where to enhance the signals this has been plotted for events with $\chi^2 \leq 1.0$ for the kinematically fitted photons. This mass spectrum has been fitted using the $a_1(1260)$ and $a_2(1320)$ using the parameterisations and parameters found in section 7.3, and gave a χ^2/NDF of 54/44. No evidence was seen for resonances in the $\rho^0\pi^0$ or the $f_2(1270)\pi^0$ mass spectra.

7.5 Study of the t Dependence

The $\pi^+\pi^-\pi^0$ mass spectrum has been studied as a function of the total 4-momentum t transferred at the fast and slow vertices, assuming the double exchange graph shown in Fig 6.21. The $\pi^+\pi^-\pi^0$ mass spectrum for events with $t < 0.3\,\mathrm{GeV}^2$ and

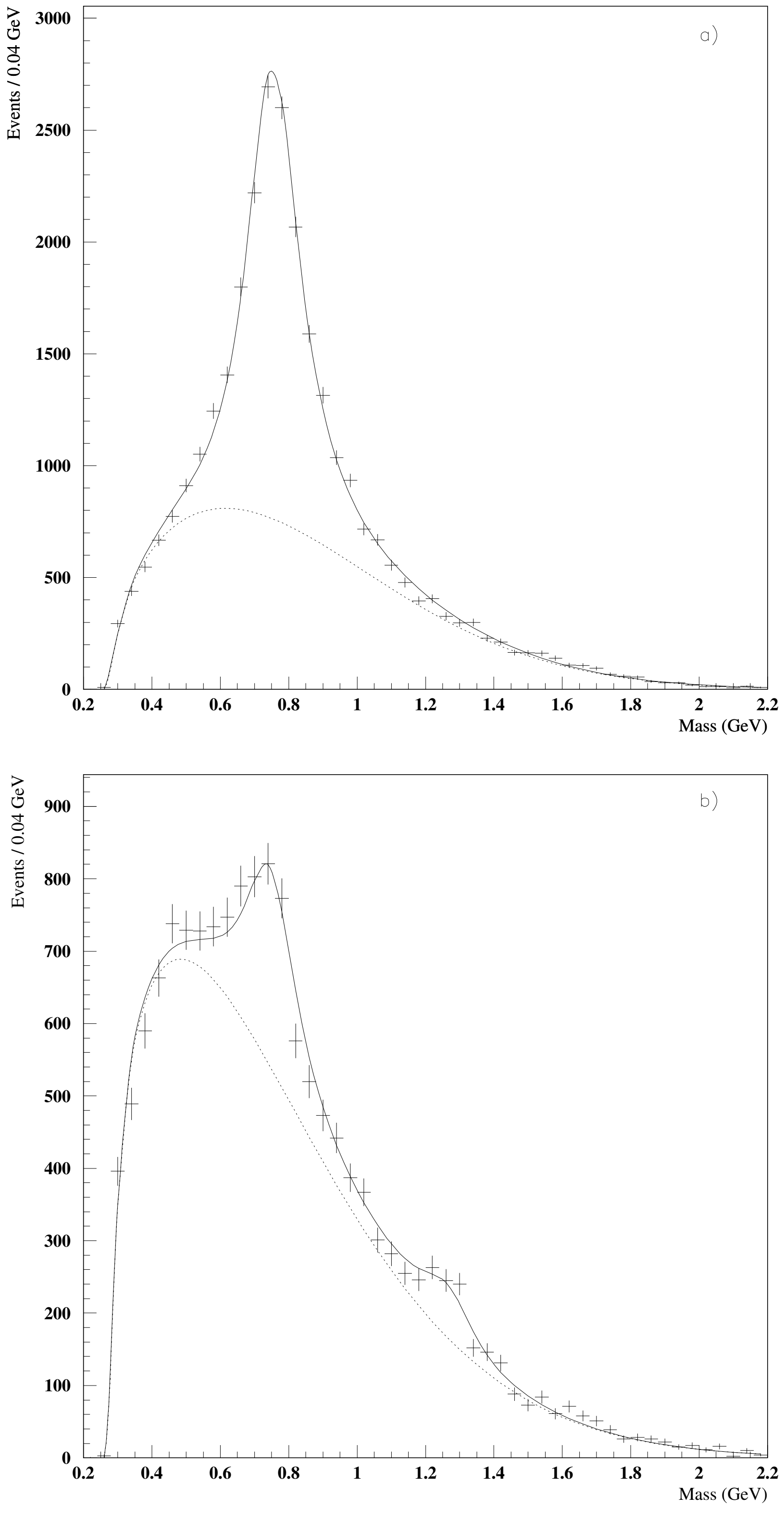

Figure 7.10: The a) $\pi^{\pm}\pi^{0}$ and b) $\pi^{+}\pi^{-}$ mass spectra from $\pi^{+}\pi^{-}\pi^{0}$. The fits are described in the text.

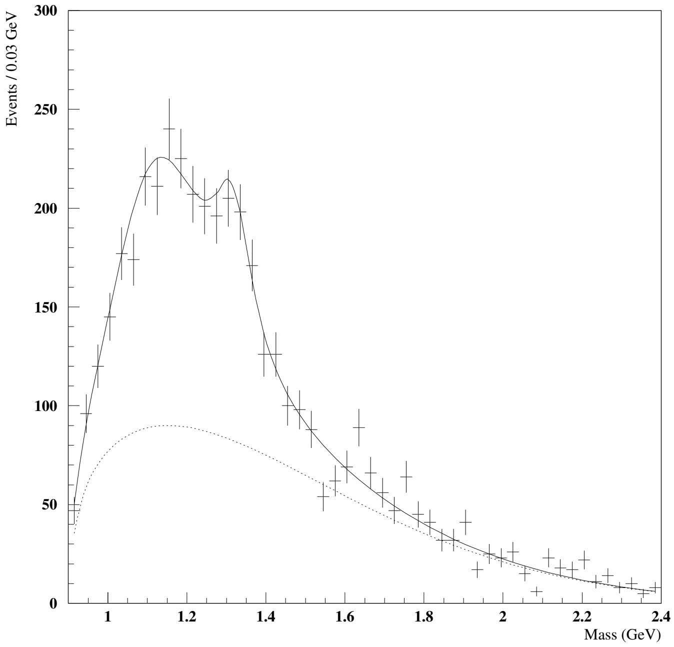

Figure 7.11: The $\rho^{\pm}\pi^{\mp}$mass spectrum, for events with $\chi^2 \leq 1.0$, with fit described in the text.

	t $<$ 0.3 GeV^2	t $>$ 0.3 GeV^2
$\eta/\omega(783)$	0.04 ± 0.01	0.18 ± 0.01
$a_1(1260)/\omega(783)$	0.75 ± 0.09	0.25 ± 0.07
$a_2(1320)/\omega(783)$	0.16 ± 0.02	0.12 ± 0.02

Table 7.1: The amount of each resonance normalised to the amount of $\omega(783)$ at low t and high t.

t $>$ 0.3 GeV^2 is shown in Fig 7.12 a) and b) respectively. The spectra have been fitted using the η, the $\omega(783)$, the $a_1(1260)$ and the $a_2(1320)$, using the parameters found from the fit to the whole spectrum as given in section 7.3. The fraction of each resonance, as compared to the amount of $\omega(783)$, and corrected for geometrical acceptance, has been calculated for each t region. This is shown in Table 7.1. It is interesting to note the reversed behaviour of the spin 0 η as compared to the spin 1 $a_1(1260)$.

7.6 Spin parity analysis

A spin parity analysis has been performed on the $\pi^+\pi^-\pi^0$ system using the Zemach tensor formalism, as explained in appendix B. The intermediate states considered

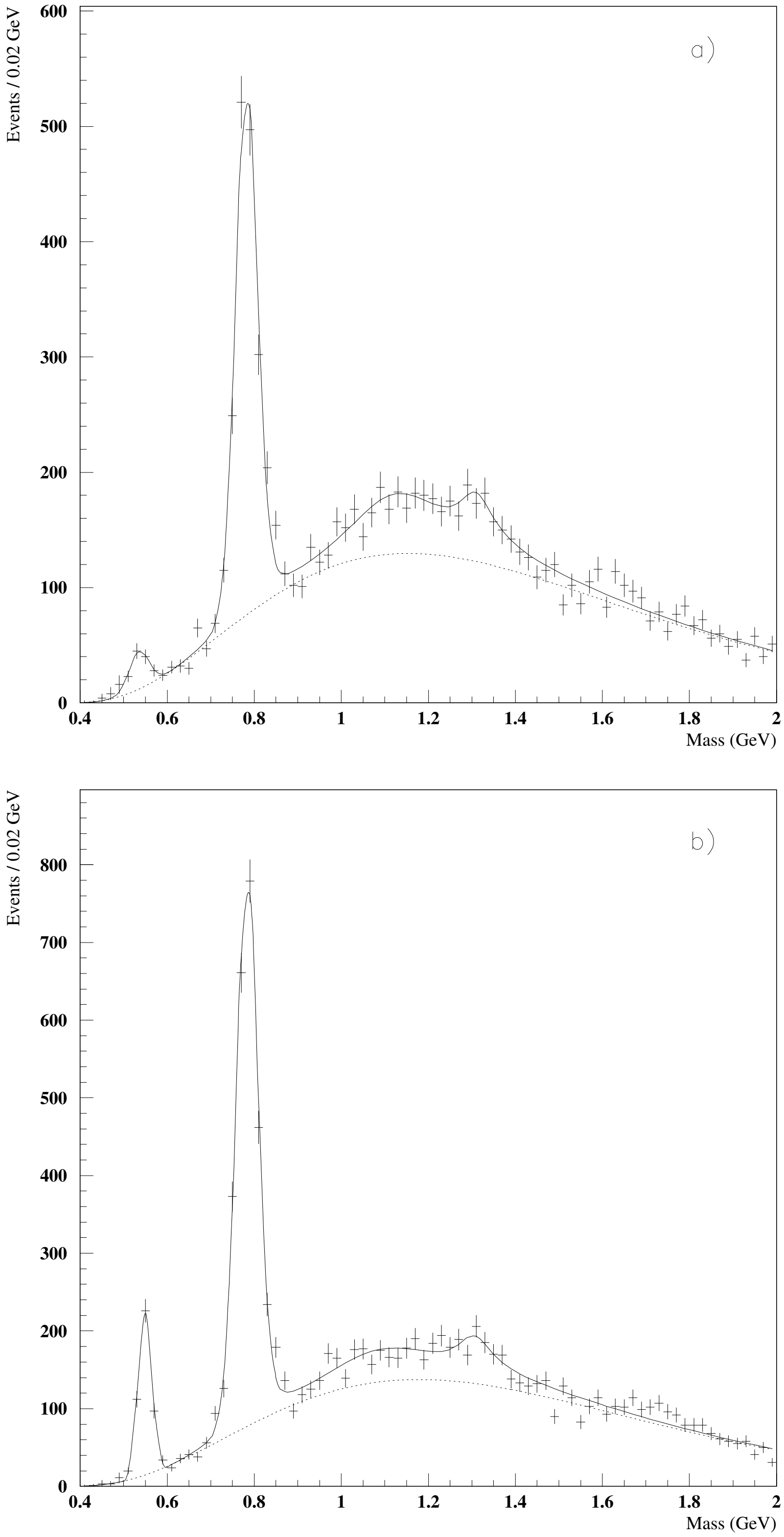

Figure 7.12: The $\pi^+\pi^-\pi^0$ mass spectrum for events with a) $t < 0.3$ and $t > 0.3\,\mathrm{GeV}^2$. The fits are described in the text.

are $\rho(770)\pi$, $f_2(1270)\pi$ and $\epsilon/f_0(1400)\pi$. For the $\rho(770)\pi$ decays both I=0 and I=1 have been considered. [1] Waves up to spin 2 have been considered in this fit. The $\rho(770)$ and $f_2(1270)$ have been parameterised by relativistic Breit-Wigners, whilst the $\epsilon/f_0(1400)\pi$ has been parameterised by a $\pi\pi$ phase shift [40]. The data have been corrected for geometrical acceptance over the Dalitz plot. The $\pi^+\pi^-\pi^0$ mass spectrum has been fitted in 40 MeV bins from 0.88 to 1.92 GeV using the maximum likelihood method. The data were found to be well described using the 1^{++}S $\rho\pi$ (I=1) and 2^{++}D $\rho\pi$ (I=1) waves and phase space only. This is shown in Fig 7.13. In particular no 1^{+-} (I=0) wave is required in the fit, i.e. there is no evidence for the $h_1(1170)$ as observed in π^-p interactions to $\pi^+\pi^-\pi^0$ [51].

The 1^{++}S wave has been fitted using the Breit-Wigner described in section 7.3 and gives the following parameters for the $a_1(1260)$:-

$$\begin{aligned} m_{a_1(1260)} &= 1239 \pm 27\ MeV \\ \Gamma_{a_1(1260)} &= 456 \pm 62\ MeV \end{aligned}$$

which are consistent with the PDG values [38].

The curve superimposed on the 2^{++}D wave is the $a_2(1320)$ wave from the fit to the $\pi^+\pi^-\pi^0$ mass spectrum, and describes the wave well in size and shape.

[1] This means that for I=0 we represent the decay by $\frac{1}{\sqrt{3}} \mid \rho^+\pi^- > -\frac{1}{\sqrt{3}} \mid \rho^0\pi^0 > +\frac{1}{\sqrt{3}} \mid \rho^-\pi^+ >$ and for I=1 we represent the decay by $\frac{1}{\sqrt{2}} \mid \rho^+\pi^- > -\frac{1}{\sqrt{2}} \mid \rho^-\pi^+ >$, where for example $\mid \rho^+\pi^- >$ represents the Zemach tensor formulation for a $\pi^+\pi^-\pi^0$ decay via $\rho^+\pi^-$, as described in appendix B, and the constant factors are the Clebsch-Gordon coefficients.

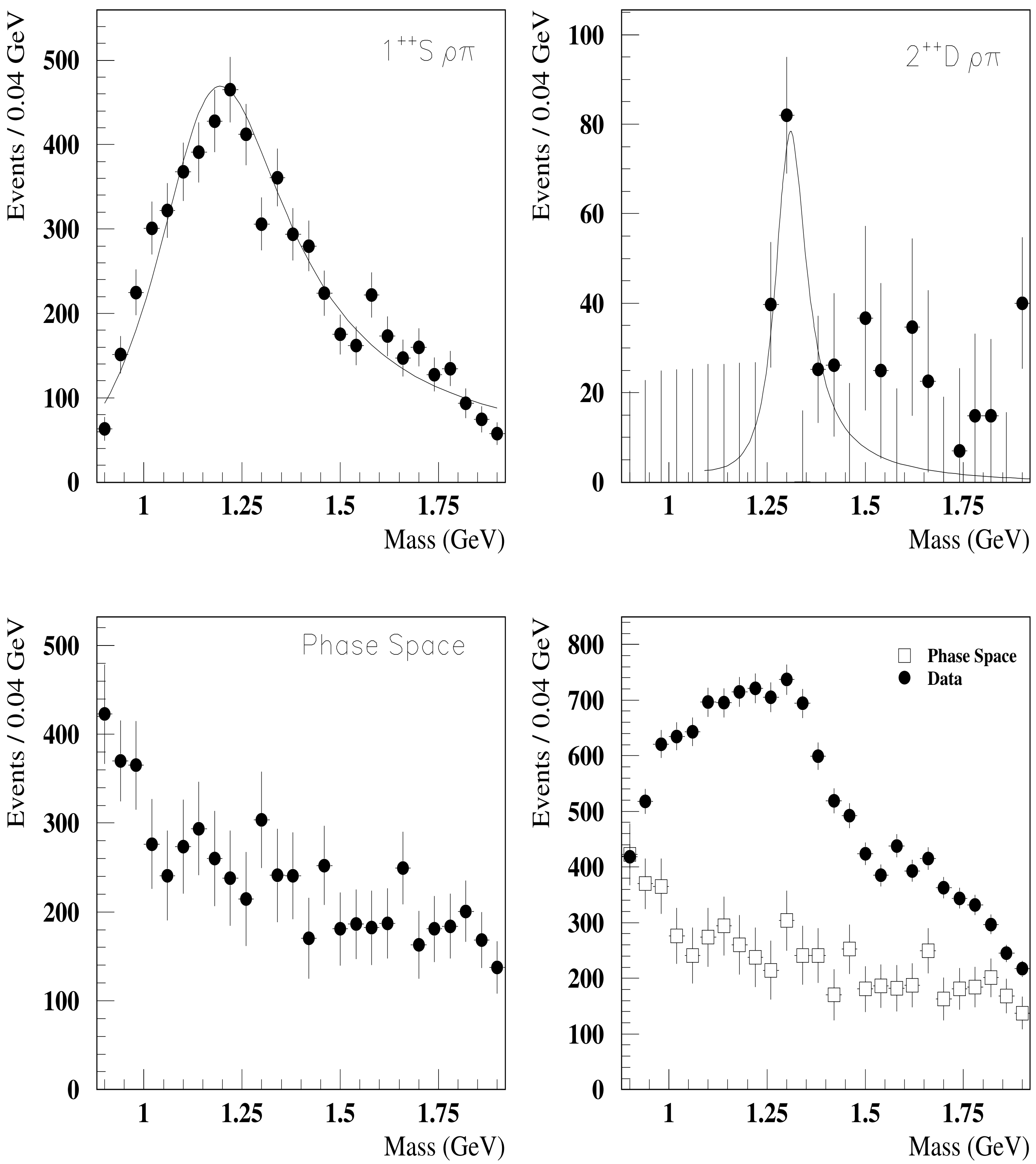

Figure 7.13: Results of the Zemach tensor spin parity analysis.

7.7 Conclusions

The $\pi^+\pi^-\pi^0$ channel from the reaction pp $\rightarrow$ $p_f(\pi^+\pi^-\pi^0)p_s$ at 450 GeV/c incident momentum has been studied and shows clear η and $\omega(783)$ signals with masses and widths

$$\begin{aligned} m\eta &= 543 \pm 1\ MeV \\ \sigma\eta &= 16 \pm 1\ MeV \\ m_{\omega(783)} &= 781 \pm 1\ MeV \end{aligned}$$

There is evidence also for the production of the I=1 $a_1(1260)$ resonance with parameters as found from a fit to the 1^{++}S wave of

$$\begin{aligned} m_{a_1(1260)} &= 1239 \pm 27\ MeV \\ \Gamma_{a_1(1260)} &= 456 \pm 62\ MeV \end{aligned}$$

and also for production of the I=1 $a_2(1320)$.

Appendix A

The WA91 Trigger

Appendix B

The Zemach Tensor Formalism

B.1 Introduction

In order to study the decay of a resonance it is necessary to construct decay matrix elements for each spin, parity, and isospin assignment under consideration. The completely general way of doing this is to perform a Partial Wave Analysis of the system, where we sum over all possible spin states of the initial and final particles to obtain an expression representing the angular distribution of the decay particles. This can prove difficult in the WA91 experiment where there is a mixture of single and double exchange mechanisms. The usual method employed in such cases is to perform a Dalitz plot analysis using the Zemach Tensor Formalism [52]. This method only considers the decay vertex and so the complexities of the production mechanism can be ignored. However the method suffers from the drawback that information about the interference between certain waves is lost, as will be explained below. However in the case of the $\eta\pi^+\pi^-$ and $\pi^+\pi^-\pi^0$ channels, where the resonances are clear and interference between waves is very unlikely, the Dalitz plot analysis is a valid and well established procedure. An outline of the method is given below.

B.2 The Dalitz plot

Consider the 3 body decay of a resonance X $\rightarrow 1 + 2 + 3$, where 1, 2 and 3 are three pseudoscalar particles. Each of the 3 decay particles has 4 degrees of freedom $(\mathrm{E}, \mathrm{p_x}, \mathrm{p_y}, \mathrm{p_z})$. As each particle must satisfy $\mathrm{E}^2 - \mathrm{p}^2 = \mathrm{m}^2$ then 3 degrees of freedom are eliminated. Also as the decay takes place in the centre of mass of X then application of overall energy and momentum conservation removes another 4 degrees of freedom. Of the 5 degrees left, 3 can be chosen to be the Euler angles $(\theta, \phi, \phi_\mathrm{z})$ defining the decay plane of X, and the other 2 as variables related to the orientation and magnitude of three-momenta within the decay plane. These are chosen to be the effective masses squared of pairs of decay particles, the reason for which will be explained later. If we now integrate over the orientation of the decay plane (meaning we consider all events no matter what the decay plane orientation is) and plot the remaining 2 degrees of freedom against each other a Dalitz plot is produced. The Dalitz plot contains all the information about the decay it is now possible to know. The advantages are we do not have to consider how the resonance was produced and we have simplified what needs to be measured to effective masses. The disadvantages are that information about interference between states of different spin, and between states with different parity, is lost. This is because states with different spin are orthogonal to each other, and thus integration over the orientation of the decay plane makes these interference terms disappear. Also the parity operation reverses the sign between the matrix elements of different parity, but since the overall decay rate is invariant the interference terms must be zero. However interference between decay modes having the same $\mathrm{J^{PC}}$ is represented in the Dalitz plot.

Now the Dalitz plot population ρ in the interval $\mathrm{dE_1dE_2}$ is related to the matrix element for the decay by the expression [2]

$$\rho = \mid \mathcal{M}(E_1, E_2) \mid^2 dE_1 dE_2 \tag{B.1}$$

where $\mathrm{E_1}$ and $\mathrm{E_2}$ are the energies of any 2 of the decay particles. It can also be shown that the energy of any one of the decay particles is proportional to the effective mass squared of the other 2 decay products. Thus the density of points on the Dalitz plot is proportional to the decay matrix element squared. In the simplest case of a 3 body phase space decay, $\mathcal{M}$ is constant and the density of points in the Dalitz plot is uniform. Any deviation from a uniform distribution indicates a structure to $\mathcal{M}$ due to dynamical effects, i.e. due to the formation of intermediate resonances (causing the Dalitz plot to exhibit bands at the mass squared of these resonances) and due to spin-parity effects.

B.3 The Zemach method

It is now necessary to construct a model to represent the decay matrix element $\mathcal{M}$ for different decay modes and different spin-parities in order to find the best combinations to fit the Dalitz plot. The formalism used was derived by Charles Zemach [52] and is based on the Standard Isobar Model [53]. This assumes that the 3 body decay of the meson resonance X proceeds through an intermediate 2 body state

$$\begin{array}{ccccc} \mathrm{X} & \rightarrow & \mathrm{Y} & + & 1 \\ \mathrm{Y} & \rightarrow & 2 & + & 3 \end{array}$$

Now the spin state of X is traditionally represented by a wave function $\psi^{\mathrm{J}}_{\mathrm{M}}$ where the magnetic quantum number M can take all integral values between -J and +J. The spin state can also be represented by a traceless symmetrical tensor of order J in 3 dimensions, with identical transformation properties under rotations as an object of spin J. This tensor is built up from the momentum vectors available in the decay process. This is the basis of the Zemach method.

Let the spin of the intermediate state Y be S, and the relative orbital angular momentum between Y and particle 1 be L. Then the spin J of resonance X is given by J = L + S, where the usual rules of angular momentum addition apply. Now both L and S are to be represented by tensors of order L and S respectively, built up from the momentum vectors of the decay particles 1, 2 and 3. In the case of the

S	Tensor	L	Tensor
0	1	0	1
1	$\mathbf{t}$	1	$\mathbf{p_1}$
2	$\frac{1}{2}(\mathbf{t}^{\mathrm{i}}\mathbf{t}^{\mathrm{j}} + \mathbf{t}^{\mathrm{j}}\mathbf{t}^{\mathrm{i}}) - \frac{1}{3}(\mathbf{t}.\mathbf{t})\delta^{\mathrm{ij}}$	2	$\frac{1}{2}(\mathbf{p_1}^{\mathrm{i}}\mathbf{p_1}^{\mathrm{j}} + \mathbf{p_1}^{\mathrm{j}}\mathbf{p_1}^{\mathrm{i}}) - \frac{1}{3}(\mathbf{p_1}.\mathbf{p_1})\delta^{\mathrm{ij}}$

Table B.1: The tensors used to represent values values of L and S in the Zemach method.

spin S of Y, the momentum vector used is

$$\mathbf{t} = \mathbf{p_2^*} - \mathbf{p_3^*}$$

where $\mathbf{p_2^*}$ and $\mathbf{p_3^*}$ are the momentum vectors of particles 2 and 3 respectively in the centre of mass frame of Y, i.e. $\mathbf{t}$ is the relative momentum of particle 2 and 3 associated with Y in the rest frame of Y. The Zemach method requires all momentum vectors to be translated into the overall centre of mass frame (i.e. of X). In terms of the momentum vectors $\mathbf{p_2}$ and $\mathbf{p_3}$ of particles 2 and 3 in the rest frame of X, $\mathbf{t}$ is given by

$$\mathbf{t} = \mathbf{p_2} - \mathbf{p_3} - (\frac{m_2^2 - m_3^2}{m_{23}^2})(\mathbf{p_2} + \mathbf{p_3}).$$

In the case of the angular momentum L between Y and particle 1, the momentum vector used is simply $\mathbf{p_1}$, the momentum of particle 1 in the rest frame of X.

Now that we have the required momentum vectors, we can construct the tensors to represent L and S. Consider the spin S. The tensors to represent it must be built from the momentum vector $\mathbf{t}$. If S=0 then a zero order tensor is required to represent it, i.e. a scalar, which is chosen to be 1. If S=1 then a first order tensor is required to represent it, i.e. a vector, which is simply $\mathbf{t}$ itself. If S=2 then a second order tensor is needed to represent it, built from $\mathbf{t}$, and it turns out to be $\frac{1}{2}(\mathbf{t}^{\mathrm{i}}\mathbf{t}^{\mathrm{j}} + \mathbf{t}^{\mathrm{j}}\mathbf{t}^{\mathrm{i}}) - \frac{1}{3}(\mathbf{t}.\mathbf{t})\delta^{\mathrm{ij}}$, which is traceless and symmetrical as required, and where $\mathbf{t}^i$ and $\mathbf{t}^j$ refer to the i th and j th components of the Cartesian vector $\mathbf{t}$.

If we now consider L, then we represent L=0, 1 and 2 in exactly the same way except that because we are now using $\mathbf{p_1}$ to build up the tensors we must replace $\mathbf{t}$ by $\mathbf{p_1}$ in the above formulae. The situation is summarised in Table B.1

The next step in the Zemach method is to combine the spin S with the orbital angular momentum L to obtain the spin J of the initial resonance X. The parity P of the state is given by

$$P = (-1)^3(-1)^L(-1)^S = (-1)^{L+S+1}$$

where the first term comes from the fact we are dealing with decays into 3 pseudoscalars which have negative intrinsic parity, the second from the orbital angular momentum S between particles 2 and 3 (i.e. the spin of Y), and the final term from the orbital angular momentum L between Y and particle 1. We can now combine to get specific values of J^P.

- S=0,L=0 :- The final state must be 0^-, i.e. scalar, and comes from combining 2 scalar quantities. This is just standard arithmetic multiplication and thus this state is represented by the scalar quantity 1.
- S=0,L=1 :- The final state must be 1^+, i.e. vector, and comes from combining a scalar quantity (1, representing S=0) with a vector quantity ($\mathbf{p_1}$, representing L=1). This is just standard multiplication again and thus this state is represented by the vector quantity $\mathbf{p_1}$.
- S=0,L=2 :- The final state must be 2^-, i.e. second order tensor, and comes from multiplying a scalar (1, representing S=0) with a second order tensor ($\frac{1}{2}(\mathbf{p_1}^{\mathrm{i}}\mathbf{p_1}^{\mathrm{j}} + \mathbf{p_1}^{\mathrm{j}}\mathbf{p_1}^{\mathrm{i}}) - \frac{1}{3}(\mathbf{p_1}.\mathbf{p_1})\delta^{\mathrm{ij}}$, representing L=2), thus this state is represented by $\frac{1}{2}(\mathbf{p_1}^{\mathrm{i}}\mathbf{p_1}^{\mathrm{j}} + \mathbf{p_1}^{\mathrm{j}}\mathbf{p_1}^{\mathrm{i}}) - \frac{1}{3}(\mathbf{p_1}.\mathbf{p_1})\delta^{\mathrm{ij}}$.
- S=1,L=0 :- The final state must be 1^+, and is similar to the S=0,L=1 case above except now the vector quantity is $\mathbf{t}$ (representing S=1) and so this state is represented by $\mathbf{t}$.
- S=1,L=1 :- there are 3 possible values of J that can be formed (0, 1 and 2). These states are to be constructed by combining the vector $\mathbf{t}$ (representing S=1) with the vector $\mathbf{p_1}$ (representing L=1). The type of combination depends on whether the final state is scalar, vector or tensor.
  - 0^- :- this is a scalar final state and so is represented by the scalar product $\mathbf{t}.\mathbf{p_1}$.

- 1^- :- This is a vector final state and so is represented by the vector product $\mathbf{t} \times \mathbf{p_1}$.
- 2^- :- This is a tensor final state, and so we need to combine the vectors $\mathbf{t}$ and $\mathbf{p_1}$ to give a tensor of the same form as the tensor in Table B.1, i.e. we represent it by $\frac{1}{2}(\mathbf{t}^{\mathrm{i}}\mathbf{p_1}^{\mathrm{j}} + \mathbf{t}^{\mathrm{j}}\mathbf{p_1}^{\mathrm{i}}) - \frac{1}{3}(\mathbf{t}.\mathbf{p_1})\delta^{\mathrm{ij}}$

- S=1,L=2 :- if we consider states up to spin 2 only, there are 2 states that are possible, and have to be constructed by combining the vector $\mathbf{t}$ with the tensor $\frac{1}{2}(\mathbf{p_1}^{\mathrm{i}}\mathbf{p_1}^{\mathrm{j}} + \mathbf{p_1}^{\mathrm{j}}\mathbf{p_1}^{\mathrm{i}}) - \frac{1}{3}(\mathbf{p_1}.\mathbf{p_1})\delta^{\mathrm{ij}}$.
  - 1^+ :- To obtain a vector from a 1×3 vector and a 3×3 tensor we simply multiply the two together to give

$$\sum_i \mathbf{t}^{\mathbf{i}}[\frac{1}{2}(\mathbf{p_1}^{\mathrm{i}}\mathbf{p_1}^{\mathrm{j}} + \mathbf{p_1}^{\mathrm{j}}\mathbf{p_1}^{\mathrm{i}}) - \frac{1}{3}(\mathbf{p_1}.\mathbf{p_1})\delta^{\mathrm{ij}}]$$
$$= \mathbf{p_1}(\mathbf{t}.\mathbf{p_1}) - \frac{1}{3}(\mathbf{p_1}.\mathbf{p_1})\mathbf{t}$$

  - 2^+ :- To obtain a tensor result we must perform a vector product of $\mathbf{t}$ within each term of the tensor representing L to obtain

$$\frac{1}{2}[(\mathbf{t} \times \mathbf{p_1})^{\mathrm{i}}\mathbf{p_1}^{\mathrm{j}} + (\mathbf{t} \times \mathbf{p_1})^{\mathrm{j}}\mathbf{p_1}^{\mathrm{i}}] - \frac{1}{3}[(\mathbf{t} \times \mathbf{p_1}).\mathbf{p_1}]\delta^{\mathrm{ij}}$$

- S=2,L=0 :- As we are combining a scalar (representing L) with a tensor (representing S) the final 2^- result is simply the tensor representing S, i.e. $\frac{1}{2}(\mathbf{t}^{\mathrm{i}}\mathbf{t}^{\mathrm{j}} + \mathbf{t}^{\mathrm{j}}\mathbf{t}^{\mathrm{i}}) - \frac{1}{3}(\mathbf{t}.\mathbf{t})\delta^{\mathrm{ij}}$

- S=2,L=1 :- Again considering spins up to 2 only, the possible states available by combining the vector $\mathbf{p_1}$ representing L with the tensor $\frac{1}{2}(\mathbf{t}^{\mathrm{i}}\mathbf{t}^{\mathrm{j}} + \mathbf{t}^{\mathrm{j}}\mathbf{t}^{\mathrm{i}}) - \frac{1}{3}(\mathbf{t}.\mathbf{t})\delta^{\mathrm{ij}}$ representing S are
  - 1^+ :- This is similar to the S=1,L=2 case except now the vector is $\mathbf{p_1}$ and the tensor involves $\mathbf{t}$ so the result is the same with the $\mathbf{p_1}$ replaced by $\mathbf{t}$ and vice versa, i.e.

$$\mathbf{t}(\mathbf{p_1}.\mathbf{t}) - \frac{1}{3}(\mathbf{t}.\mathbf{t})\mathbf{p_1}$$

– 2^+ :- Again similar to S=1,L=2 but with $\mathbf{p_1}$ replaced by $\mathbf{t}$ and vice versa, i.e.

$$\frac{1}{2}[(\mathbf{p_1} \times \mathbf{t})^{\mathrm{i}}\mathbf{t}^{\mathrm{j}} + (\mathbf{p_1} \times \mathbf{t})^{\mathrm{j}}\mathbf{t}^{\mathrm{i}}] - \frac{1}{3}[(\mathbf{p_1} \times \mathbf{t}).\mathbf{t}]\delta^{\mathrm{ij}}$$

This covers the combinations used in this thesis.

The final element needed to represent the decay matrix element is to multiply the relevant Zemach tensor by a Breit-Wigner (or other parameterisation) to describe the intermediate resonance Y. If the intermediate resonance can exist in more than one charge state then the total amplitude is the sum of the individual amplitudes multiplied by the appropriate Clebsch-Gordon coefficient of isospin. Thus the final matrix element is given by

$$\mathcal{M} = \sum_{\mathrm{i}} \mathrm{CG}^{\mathrm{i}}\, \mathrm{BW}^{\mathrm{i}}\, \mathrm{T}_1^{\mathrm{i}}(\mathrm{S}) * \mathrm{T}_2^{\mathrm{i}}(\mathrm{L})$$

where CG is the isospin Clebsch-Gordon coefficient, BW is the Breit-Wigner representing the intermediate resonance, $\mathrm{T_1(S)}$ is the tensor representing the spin S of the intermediate resonance, $\mathrm{T_2(L)}$ is the tensor representing the angular momentum L between the intermediate resonance and the remaining particle, $\mathrm{T_1(S)} * \mathrm{T_2(L)}$ represents the coupling between the tensors to obtain the spin-parity of the final state (as explained above) and the sum is over all the available charge states of the intermediate resonance.

B.4 Normalisation of the Waves

We now have a way of representing waves of various spin-parity and decaying through various intermediate 2-body states. However these waves are not normalised relative to each other, which is a problem if we want to use more than 1 wave to try and describe the data. To normalise the waves the integrals of each wave are calculated in the total Lorentz invariant phase space. As the integrals are mass dependent they are calculated throughout the mass range to be considered in 0.01 GeV steps. This is done using FOWL [54] which is a program using the Monte Carlo method to generate phase space distributions due to particle interactions. It does this by taking as input the centre-of-mass energy of the decay, the number of decay particles and their masses, and then using these to calculate the four-momentum of each particle and a weight WT related to the phase space distributions. These four-momenta are then used to calculate each possible Zemach amplitude $\mathcal{M}(\text{wave})$. The normalisation integral for each wave is then given by

$$\text{Norm Int(wave)} = \frac{\sum \text{WT} \mid \mathcal{M}(\text{wave}) \mid^2}{\sum \text{WT}}$$

where the sum is over all the FOWL generated events. Figs B.1 and B.2 show the normalisation integrals for a selection of waves for the $\eta\pi^+\pi^-$ and $\pi^+\pi^-\pi^0$ channels.

B.5 The Maximum Likelihood Fit

This method assumes that the observation of a set of quantities x_i is related to a set of parameters α_i by a probability distribution $P(\alpha_i, x_i)$. The maximum likelihood method consists of finding the set of values α_i which maximises the joint probability density for all the observations, given by

$$\mathcal{L}(\alpha) = \prod_n P(\alpha_i, x_i)$$

where $\mathcal{L}(\alpha)$ is known as the likelihood [55], and the product is over all the events observed in the experiment. It is easier to deal with the logarithmic likelihood

$$\ln(\mathcal{L}(\alpha)) = \sum_n \ln(P(\alpha_i, x_i))$$

seeing as both $\mathcal{L}(\alpha)$ and $\ln(\mathcal{L}(\alpha))$ are both maximised for the same set of α, and as then we are dealing with a sum rather than a large product. In the case of fitting the Dalitz plot each x_i is a Zemach amplitude for the event, and α_i is the amount of that amplitude. The overall probability for each event is given by

$$P(\alpha_i, x_i) = \sum_i \alpha_i \mid \mathcal{M}_i^{JP} \mid^2 + (1 - \sum_i \alpha_i)$$

where $\mathcal{M}_i^{JP}$ is the Zemach amplitude for a specific wave with spin J and parity P, α_i is the amount of that amplitude, and $(1 - \sum \alpha_i)$ represents the background.

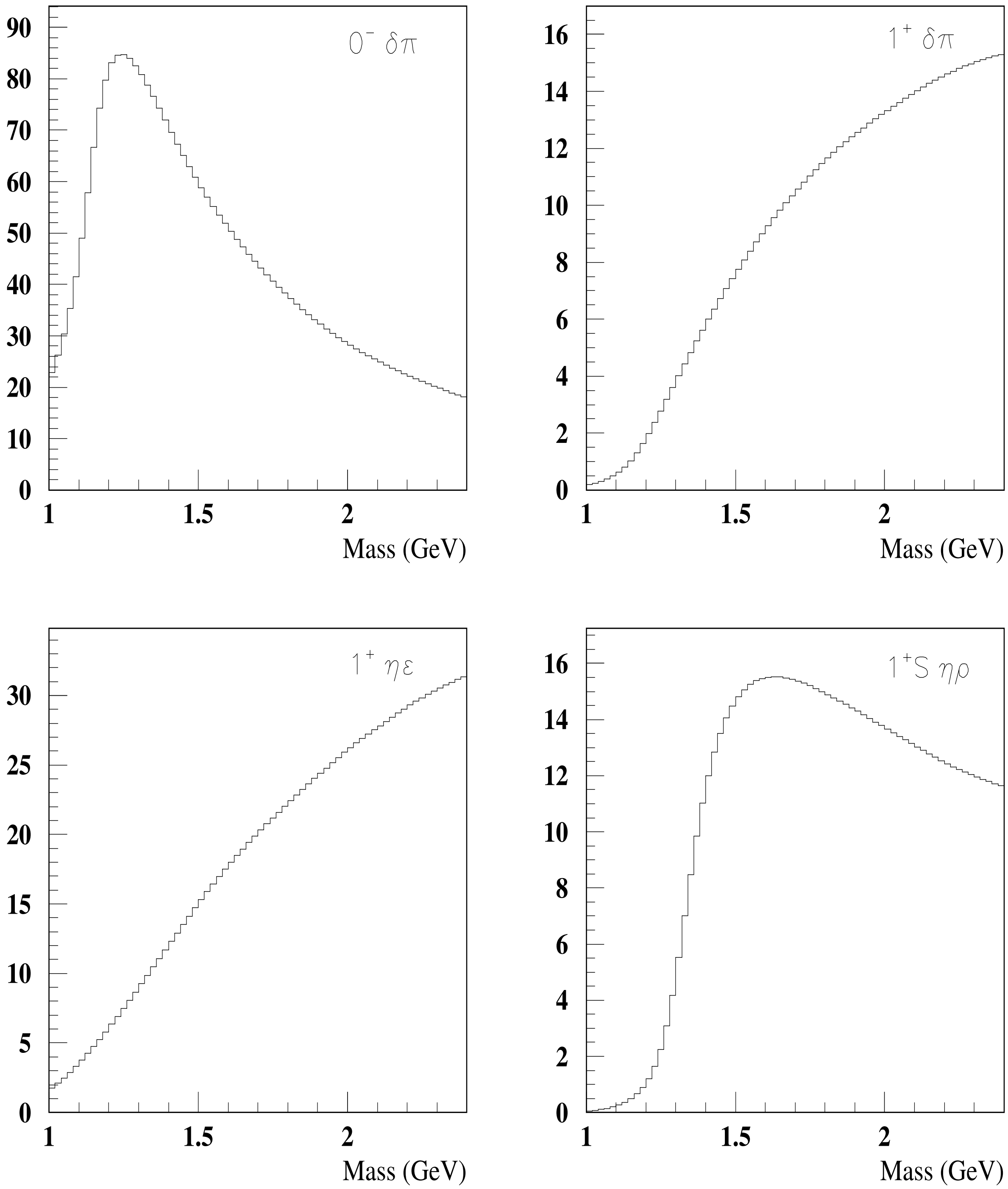

Figure B.1: Normalisation integrals for a selection of waves for the $\eta\pi^+\pi^-$ channel.

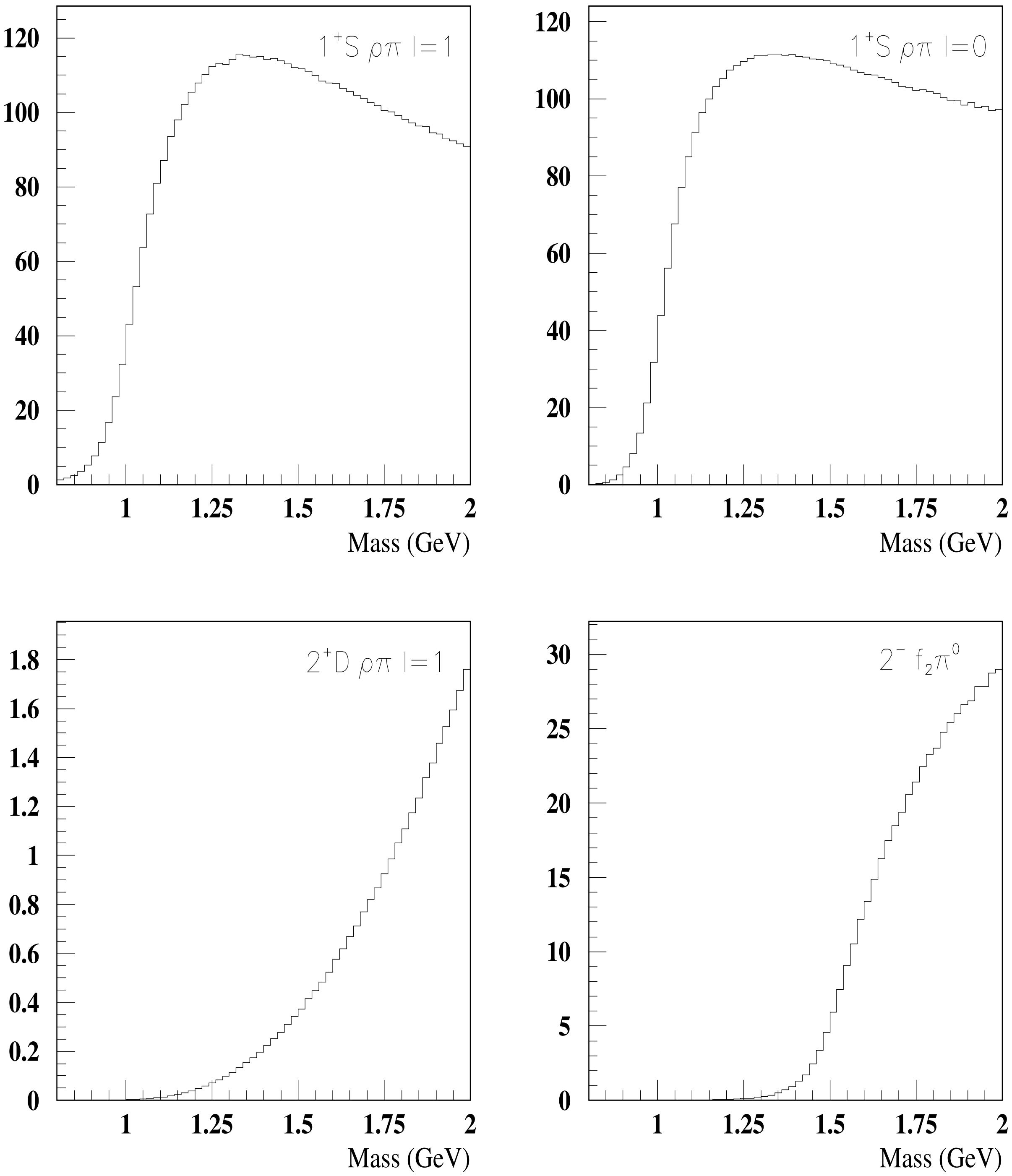

Figure B.2: Normalisation integrals for a selection of waves for the $\pi^+\pi^-\pi^0$ channel.

Thus each event is read in, the Zemach amplitudes for each wave calculated and normalised using the normalisation integrals, and the logarithmic likelihood calculated for the waves being considered. This is repeated for each event, and the sum over all the events of the log likelihoods computed. The negative of this is minimised using MINUIT [36] to give the fraction of each wave needed to fit the data. By comparing the log likelihoods for different combinations of waves the best fit can be obtained, since a difference in log likelihoods between two combinations of waves of $\Delta\mathcal{L}$ corresponds to $\sqrt{2\Delta\mathcal{L}}$ standard deviations between the two hypotheses.

Appendix C

The ORC Reconstruction Code

C.1 Introduction

Experimental detectors record the passage of a particle as a set of voltage signals which are converted to a digital signal read out onto tape. Before physics analysis can begin it is therefore necessary to convert these signals into the momentum and energy of the particle giving rise to them, in effect reconstructing the particle trajectory. In WA91 two reconstruction programs were needed, one for recreating the fast and slow protons and other charged tracks, using information from the MWPC's, drift chambers and microstrips, and one for recreating the photons either produced directly or coming from neutral particle decays, using the electromagnetic calorimeter OLGA. The charged particle reconstruction code was called TRIDENT, and the neutral particle reconstruction code was called ORC (OLGA Reconstruction Code). Most of the algorithms used were based on those used in SNARK [10], a reconstruction program developed by NA14 for OLGA. The following appendix describes how ORC reconstructs the photon impacts from the signals in OLGA.

C.2 The Reconstruction method

Since a photon undergoing an electromagnetic shower can deposit its energy in several samplers/fingers/blocks of OLGA, then in order to reconstruct them the individual blocks, samplers and fingers that have fired must be clustered together into single photon impacts and these clusters must then be correlated. The method employed to do this can be summarised as follows :-

1. Convert the ADC signals above threshold in the blocks and samplers to energy using the measured calibration constants, and normalise the finger signals using the normalisation constants.

2. Cluster the block energies together to give the impact energies in the blocks.

3. Cluster the finger signals together to give the impact positions.

4. Associate the finger impacts with the block impacts, removing as many ambiguous associations as possible.

5. Associate the finger/block clusters with the sampler impacts.

6. Write out the energy/position information for each cluster onto tape.

C.2.1 Block clustering

The columns of lead glass blocks are searched until the first one with energy in it is found. The surrounding blocks (excluding diagonally adjacent) are searched and added to the cluster if they have energy in them. Each of these new blocks is searched for neighbours in the same way, and the procedure repeated until no new neighbouring blocks are found. The cluster is then closed, each block in it is marked as being part of a cluster, and the columns are searched again for any unmarked blocks with energy in them, where the clustering will begin again. Thus after searching through all the OLGA blocks, they will have been clustered into potential single photon impacts.

The next stage is to examine each block cluster to see if it is of the correct topology for a single photon impact, for example it is unlikely that a single photon shower spreading into 3 blocks would do so in a straight line of blocks (an L shape would be more likely). Such clusters are split up into smaller subclusters according to the pattern of energy deposition in the individual blocks if this is possible.

Thus at the end of this clustering routine a set of primary and subclusters are formed, with block cluster energy E_{blk} equal to the sum of the block energies in the cluster. An initial impact position (y_{blk}, z_{blk}) for the cluster is obtained using the Russe method, which assumes the lateral energy deposition of an electromagnetic shower falls exponentially (the shower barycentre method assumes a linear fall which is less accurate). The Russe method can only be used if there are $\geq$ 2 blocks in the cluster in the projection (y or z) being considered. If there is only 1 block in this projection the block centre coordinate has to be used.

C.2.2 Finger clustering

As stated in chapter 2, the fingers are split into 4 half planes of 180 fingers each, 2 half planes for measuring the y impact coordinate and 2 for measuring the z impact coordinate. Each half plane is clustered by searching each finger in turn until the first one with a signal (above threshold) is found. Each adjacent finger is added to the cluster if there is a signal in it. One missing finger is allowed before the cluster is closed (see Fig 4.16c). The impact coordinate for the cluster is then defined as the barycentre of the cluster, i.e.

$$y_{impact} = \frac{\sum y_n S_n}{\sum S_n}$$

where y_n is the y (or z) coordinate and S_n the ADC signal of the n'th finger in the cluster, and the sum is over all the fingers in the cluster. This clustering is repeated when the next finger with a signal in it is found.

The clusters are then checked to see if they have the correct profile, by checking the variance of the signal distribution in the cluster. If this is greater than 2 then it is seen whether the cluster can be split into 2 smaller clusters. This is done by checking if the profile of the cluster is of the normal type (see Fig 4.16a). If it is not the cluster is split up.

Thus at the end of this clustering routine a set of y and z finger clusters are produced, with the impact coordinate given by the cluster barycentre y_{fing} (or z_{fing}).

C.2.3 Associating the block and finger clusters

Each block cluster is taken in turn, and a search window defined around it from the top-left corner of the top-left block in the cluster, to the bottom-right corner of the bottom-right block in the cluster. The finger clusters are then searched and any whose y or z barycentres fall within this window are associated with the block cluster. If any of these associated finger clusters have $\mid y_{\rm fing} - y_{\rm blk} \mid > 8$ cm (and similarly for z) they are rejected. Once this has been done for all the block clusters, a check is made for ambiguous associations (i.e. when a finger cluster is associated with 2 or more block clusters) and their possible solution. The ambiguities are solved if possible by methods such as checking how close the ambiguous cluster is to each block cluster, whether there is sampler information, checking how the energy in the fingers compares with the blocks and checking how many finger clusters are associated with the other block clusters in each projection. The ultimate aim is to have each finger cluster (y and z) associated with only one block cluster.

C.2.4 Association of sampler impacts

The final task is to associate the sampler impacts with the block/finger cluster. This is done by checking the sampler at the impact position of the block/finger cluster for energy. Any sampler hits not associated with a block cluster in this way are checked if they are above or below an already associated sampler, in which case their energy is added to the associated sampler as long as the impact position for the block/finger cluster is less than 5 cm away from the border between the 2 samplers (otherwise it is unlikely that the shower would have spread between the 2 samplers). For samplers that have been associated with more than 1 block cluster the sampler energy is shared amongst the block clusters in proportion to the energy deposited in the block clusters. Finally the sampler energy $E_{\rm samp}$ is corrected for attenuation according to the impact position. The cluster energy is then given by $E_{\rm clus} = E_{\rm blk} + E_{\rm samp}$.

C.2.5 Reassociation

The finger/block association routines so far described have been designed to be very strict. To ensure that potential finger information is not lost a final routine called REPEN was used as a backup to associate finger and blocks. REPEN takes a block cluster and again searches for y and z finger clusters in the same way as described in section C.2.3. Then to eliminate ambiguous associations each of these associated finger clusters is taken in turn and tested to see if it can be associated with any of the other block clusters in that event. This is done by taking one of the other block clusters, and seeing if the finger cluster coordinate falls within the boundaries of any of the blocks in this block cluster. If it does, and this block contains the largest amount of energy for that block cluster, the finger cluster is rejected as ambiguous. If this cannot be done for any of the other block clusters the finger cluster is kept. If more than one finger cluster in either projection is kept for a particular block cluster the nearest one to the block cluster impact position (y_{blk}, z_{blk}) is used. This procedure is then repeated for all the block clusters in the event.

C.2.6 ORC codes

For each event ORC outputs the energy and (y,z) coordinate of each cluster found, along with a code Itype which depends on how the position coordinates were determined (i.e. whether by the fingers or the blocks, and whether the finger coordinates came from the main ORC routines or from REPEN). The explanation of each Itype code is given in Table C.1 Thus clusters with Itype between 10 and 13 have the y and z coordinate of the cluster determined by finger information, clusters with Itype between 14 and 17 have either the y or z coordinate determined by finger information, and type 18 have the y and z coordinate determined by block information alone. A type 20 photon is one where no finger information is available, but the Russe method can only be used in either y or z (or neither). To indicate a subcluster 30 is added to the Itype code, e.g. Itype of 40 means a subcluster with the y and z coordinates determined by the fingers. The effect that the fingers have can be seen

Itype	y coordinate	z coordinate
10	finger (main)	finger (main)
11	finger (main)	finger (REPEN)
12	finger (REPEN)	finger (main)
13	finger (REPEN)	finger (REPEN)
14	finger (main)	block (Russe)
15	block (Russe)	finger (main)
16	finger (REPEN)	block (Russe)
17	block (Russe)	finger (REPEN)
18	block (Russe)	block (Russe)

Table C.1: Table to show how the Itype ORC codes relate to the way the y and z cluster coordinates are determined.

by plotting the $\gamma\gamma$ mass spectrum for the momentum balanced $\pi^+\pi^-\gamma\gamma$ system, as shown in Fig C.1. Fig C.1a shows the $\gamma\gamma$ mass spectrum when both photons have their y and z coordinates measured by the fingers (i.e. Itype between 10 and 13), Fig C.1b for when both photons have either their y or z coordinates measured by the fingers (i.e. Itype between 14 and 17), and Fig C.1c for when both photons have their y and z coordinates measured by the blocks (i.e. Itype of 18 or 20). As the amount of finger information decreases the amount of background increases and the resolution becomes poorer.

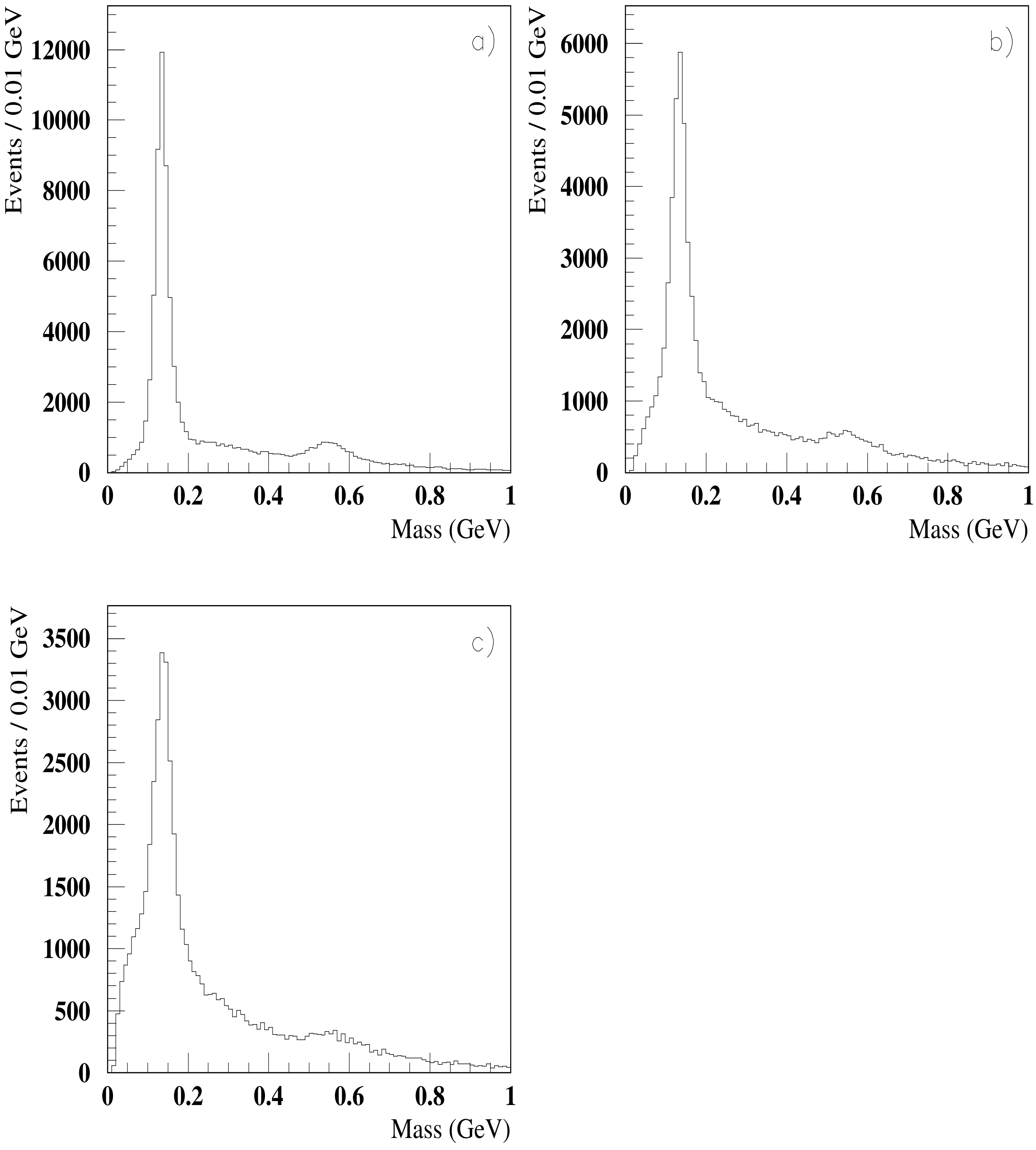

Figure C.1: The $\gamma\gamma$ mass spectrum from $\pi^+\pi^-\gamma\gamma$ for various types of events.

Bibliography

[1] S.L. Glashow, Nucl. Phys. **22** (1961) 579,
S. Weinberg, Phys. Rev. Lett. **19** (1967) 1264,
A. Salam, *Elementary Particle Theory*, (Ed.) N. Svartholm, Almqvist and Wikell, Stockholm, 1968.

[2] D.H. Perkins, *Introduction to High Energy Physics*, Addison-Wesley Publishing Company, Third Edition 1987.

[3] I.J.R. Aitchison and A.J.G. Hey, *Gauge theories in particle physics*, Adam Hilger, 1989.

[4] F. Halzen and A.D. Martin, *Quarks and Leptons: An Introductory Course in Modern Particle Physics*, John Wiley and Sons, 1984.

[5] G. 't Hooft,
Nucl. Phys. **B33** (1971) 173, Nucl. Phys. **B35** (1971) 167.

[6] T. Kinoshita and J. Sapirstein, *Atomic Physics Nine*, (Eds.) R.S. Van Dyck Jr. and E.N. Fortson, Singapore: World Scientific, 1984.

[7] F.E. Close, *Gluonic Hadrons*, RAL-87-072 (1987).

[8] D. Robson, Nucl. Phys. **B130** (1984) 328.

[9] CERN Proposal SPSC/90-2/P249 (1990).

[10] E. Augé, *Thése de 3e Cycle*, Orsay (1983).

[11] U. Fano, Ann. Rev. Nucl. Sci. **13** (1963) 1.

[12] R. Fernow, *Introduction to experimental particle physics*, Cambridge University Press,1990.

[13] R. Wigmans, *Advances in Hadron Calorimetry* ,CERN-PPE/91-39.

[14] C. Fabjan and T. Ludlam, *Calorimetry in high energy physics*, Ann. Rev. Nucl. Part. Sci., **32** 335-89, 1982.

[15] W. Heitler, *The Quantum Theory of Radiation*, Oxford: Clarendon Press, Third Edition 1953.

[16] Nelson,W.R.,Hirayama,H. and Rogers,D.W.O, *SLAC Report 165*, Stanford:SLAC (1985).

[17] J. Jelley, *Cerenkov Radiation and its Applications*, Pergamon, 1958.

[18] S. Katsanevas, *Thése de 3e Cycle*, Orsay (1979).

[19] P.Baillon et al., Nuovo Cimento, **50a** (1967) 393.

[20] D.L. Scharre et al., Phys. Lett. **97B** (1980) 329.

[21] C. Edwards et al., Phys. Rev. Lett. **49** (1982) 259.

[22] M.G. Rath et al., Phys. Rev. **D40** (1989) 693.

[23] S. Fukui et al., Phys. Lett. **267B** (1991) 293.

[24] T. Armstrong et al., Phys. Lett. **221B** (1989) 216.

[25] M. Burchell et al., Nucl. Phys. **B21** (1991) 132 (suppl).

[26] Z. Bai et al., Phys. Rev. Lett. **65** (1990) 2507.

[27] G. Gidal et al., Phys. Rev. Lett. **59** (1987) 2016.

[28] A. Ando et al., Phys. Rev. Lett. **57** (1986) 1296.

[29] T. Armstrong et al., Zeit. Phys. **C52** (1991) 389.

[30] D. Aston et al., Phys. Lett. **201B** (1988) 573.

[31] S. Ishida et al., Progress of Theoretical Phys. **82** (1989) 119.

[32] D.O. Caldwell, Mod. Phys. Lett. **A2** (1987) 771.

[33] J. Weinstein, Proceedings of the Workshop on Glueballs, Hybrids and Exotics, BNL, August 1988.

[34] T. Armstrong et al., Phys. Lett. **B228** (1989) 536.

[35] S. Abatzis et al., Phys. Lett. **B324** (1994) 509.

[36] F. James and M. Roos, MINUIT Computer Physics Communications **10** (1975) 343.

[37] R. le Marachel, private communication.

[38] Review of Particle Properties, Phys. Lett. **B239** (1990).

[39] W. Beusch, Omega Prime, **CERN/SPSC/77-70** (1977).

[40] B. Hyams et al., Nucl. Phys. **B64** (1973) 134,
S. Protopopescu et al., Phys. Rev. **D7** (1973) 1280.

[41] R. T. Deck, Phys. Rev. Lett. **13** (1964) 169.

[42] C. Daum et al., Phys. Lett. **89B** (1980) 281.

[43] J. Dankowych et al., Phys. Rev. Lett. **46** (1981) 580.

[44] H. Albrecht et al., Zeit. Phys. **C33** (1986) 7.

[45] W. B. Ruckstuhl et al., Phys. Rev. Lett. **56** (1986) 2132.

[46] W. B. Schmidke et al., Phys. Rev. Lett. **57** (1986) 527.

[47] M. G. Bowler, Phys. Lett. **182B** (1986) 400.

[48] N. A. Tornqvist, Zeit. Phys. **C36** (1987) 695.

[49] Ph. Gavillet et al., Phys. Lett. **69B** (1977) 119.

[50] T. Armstrong et al., Zeit. Phys. **C48** (1990) 213.

[51] A. Ando et al., Phys. Lett. **291B** (1992) 496.

[52] C. Zemach, Phys. Rev. **B140** (1965) 97.

[53] C. Zemach, Phys.Rev. **B133** (1964) 1201.

[54] F. James, FOWL, CERN Computer Centre W505 (1977).

[55] W. T. Eadie et al., *Statistical methods in experimental physics*, North-Holland, 1971.